



Argonne National Laboratory

REACTOR DEVELOPMENT PROGRAM PROGRESS REPORT

July 1970

The facilities of Argonne National Laboratory are owned by the United States Government. Under the terms of a contract (W-31-109-Eng-38) between the U. S. Atomic Energy Commission, Argonne Universities Association and The University of Chicago, the University employs the staff and operates the Laboratory in accordance with policies and programs formulated, approved and reviewed by the Association.

MEMBERS OF ARGONNE UNIVERSITIES ASSOCIATION

The University of Arizona	Kansas State University	The Ohio State University
Carnegie-Mellon University	The University of Kansas	Ohio University
Case Western Reserve University	Loyola University	The Pennsylvania State University
The University of Chicago	Marquette University	Purdue University
University of Cincinnati	Michigan State University	Saint Louis University
Illinois Institute of Technology	The University of Michigan	Southern Illinois University
University of Illinois	University of Minnesota	University of Texas
Indiana University	University of Missouri	Washington University
Iowa State University	Northwestern University	Wayne State University
The University of Iowa	University of Notre Dame	The University of Wisconsin

LEGAL NOTICE

This report was prepared as an account of Government sponsored work. Neither the United States, nor the Commission, nor any person acting on behalf of the Commission:

A. Makes any warranty or representation, expressed or implied, with respect to the accuracy, completeness, or usefulness of the information contained in this report, or that the use of any information, apparatus, method, or process disclosed in this report may not infringe privately owned rights; or

B. Assumes any liabilities with respect to the use of, or for damages resulting from the use of any information, apparatus, method, or process disclosed in this report.

As used in the above, "person acting on behalf of the Commission" includes any employee or contractor of the Commission, or employee of such contractor, to the extent that such employee or contractor of the Commission, or employee of such contractor prepares, disseminates, or provides access to, any information pursuant to his employment or contract with the Commission, or his employment with such contractor.

Printed in the United States of America

Available from

Clearinghouse for Federal Scientific and Technical Information

National Bureau of Standards, U. S. Department of Commerce

Springfield, Virginia 22151

Price: Printed Copy \$3.00; Microfiche \$0.65

ARGONNE NATIONAL LABORATORY
9700 South Cass Avenue
Argonne, Illinois 60439

REACTOR DEVELOPMENT PROGRAM
PROGRESS REPORT

July 1970

Robert B. Duffield, Laboratory Director
Robert V. Laney, Associate Laboratory Director

Division

Applied Physics
Center for Environmental Studies
Chemical Engineering
EBR-II Project
Engineering and Technology
Materials Science
Reactor Analysis and Safety

Director

R. Avery
L. E. Link
R. C. Vogel
M. Levenson
S. A. Davis
P. G. Shewmon
W. R. Simmons

Report coordinated by
M. Weber and V. G. Trice, Jr.

Issued August 27, 1970

FOREWORD

The Reactor Development Program Progress Report, issued monthly, is intended to be a means of reporting those items of significant technical progress which have occurred in both the specific reactor projects and the general engineering research and development programs. The report is organized in accordance with budget activities in a way which, it is hoped, gives the clearest, most logical overall view of progress. Since the intent is to report only items of significant progress, not all activities are reported each month. In order to issue this report as soon as possible after the end of the month editorial work must necessarily be limited. Also, since this is an informal progress report, the results and data presented should be understood to be preliminary and subject to change unless otherwise stated.

The issuance of these reports is not intended to constitute publication in any sense of the word. Final results either will be submitted for publication in regular professional journals or will be published in the form of ANL topical reports.

The last six reports issued
in this series are:

December 1969	ANL-7655
January 1970	ANL-7661
February 1970	ANL-7669
March 1970	ANL-7679
April-May 1970	ANL-7688
June 1970	ANL-7705

REACTOR DEVELOPMENT PROGRAM

Highlights of Project Activities for July 1970

EBR-II

The reactor was operated for 1277 MWd from June 16 through July 15, bringing its cumulative operational total to 37,490 MWd.

Reclamation of centrifugally bonded vendor fuel elements by a two-step heat treatment is proving successful. Of the 473 elements put through reclamation to date, 458 are acceptable. The 15 reject elements may be acceptable under a recently approved revision of the product specification for EBR-II fuel elements.

A prototype of a device for measuring bow and length of irradiated experimental capsules and elements is operating in the FCF air cell. It can measure length to ± 0.001 in., bow to ± 0.020 in., and bow location to $\pm 1/32$ in.

ZPR-3

The third critical assembly in support of the EBR-II program, Assembly 62, has been made critical with a two-drawer-thick stainless steel-rich radial reflector. Core composition and axial-reflector geometry have not been changed from that of Assembly 61, but the nickel-rich reflector of that assembly has been replaced by a stainless steel reflector, which will be enlarged to four-drawer thickness in two steps.

ZPR-6

As the loading of the 3500-liter, mixed-oxide Assembly 7 proceeds, predicted values for each parameter to be measured as part of the experimental program are being calculated.

The construction of the Variable Temperature Rodded Zone to be used with this facility is now 15% complete.

ZPR-9

Measurements on Assembly 26, the FTR-3 critical assembly, have been extended to include the central fission rate ratios of ^{238}U , ^{239}Pu , and ^{240}Pu to ^{235}U . The assembly was subsequently returned to its reference configuration to determine the reactivity worths of a number of control-rod arrangements.

ZPPR

In anticipation of future zone loadings of pin-type fuel, the core composition of the demonstration benchmark assembly, ZPPR-Assembly 2, has been modified to better approximate these loadings. The modification resulted in a slight increase in reactivity, but selected perturbation measurements in the new core agreed within experimental error with identical measurements made in the unmodified core. Perturbation-sample worths made with the autorod have been shown to be completely free of interaction effects between autorod and sample.

TABLE OF CONTENTS

	<u>Page</u>
I. LIQUID METAL FAST BREEDER REACTORS--CIVILIAN	1
A. Physics Development	1
1. Theoretical Reactor Physics	1
2. Experimental Reactor Physics	3
3. ZPR and ZPPR Operations and Analysis	7
4. ZPR Materials	18
B. Component Development	28
1. Instrumentation and Control	28
2. Fuel Handling, Vessels, and Internals	36
C. EBR-II--Research and Development	39
1. New Subassemblies and Experimental Support	39
2. Instrumented Subassemblies	41
3. Coolant Chemistry	43
4. Experimental Irradiation and Testing	46
5. Materials-Coolant Compatibility	54
6. Reactor Analysis, Testing, and Methods Development	56
7. Metal Driver Fuel Development and Application	64
8. Hot Fuel Examination Facilities	72
9. Characterization of Irradiation Environment	73
D. EBR-II--Fuel and Hardware Procurement	76
1. Reclamation of Vendor Fuel	76
E. EBR-II--Operations	76
1. Reactor	76
2. Fuel Cycle Facility	77
PUBLICATIONS	79
II. OTHER FAST REACTORS--OTHER FAST BREEDER REACTORS--FUEL DEVELOPMENT	80
A. Irradiation Effects, Mechanical Properties and Fabrication	80
1. Neutron Simulation Studies Using 4-MeV Dynamitron	80
2. Mechanical Properties of Cladding Materials	80

TABLE OF CONTENTS

	<u>Page</u>
III. GENERAL REACTOR TECHNOLOGY	85
A. Applied and Reactor Physics Development	85
1. Theoretical Reactor Physics--Research and Development	85
2. Nuclear Data--Research and Development	101
B. Reactor Fuels and Materials Development	103
1. Fuels and Claddings--Research and Development	103
2. Techniques of Fabrication and Testing--Research and Development	113
3. Engineering Properties of Reactor Materials--Research and Development	119
C. Engineering Development--Research and Development	132
1. Instrumentation and Control	132
2. Engineering Mechanics	134
D. Chemistry and Chemical Separations	136
1. Fuel Cycle Technology--Research and Development	136
2. General Chemistry and Chemical Engineering--Research and Development	142
PUBLICATIONS	144
IV. NUCLEAR SAFETY RESEARCH AND DEVELOPMENT	146
A. LMFBR Safety--Research and Development	146
1. Coolant Dynamics	146
2. Fuel Dynamics Studies in TREAT	150
3. Fuel-Coolant Interactions	159
4. Post-accident Heat Removal	162
B. Operations	168
1. TREAT Operations	168
C. Engineered Safety Features--Safety Features Technology	168
1. Reactor System and Containment Structural Dynamic Response	168
PUBLICATIONS	173
PUBLICATIONS--General	173

I. LIQUID METAL FAST BREEDER REACTORS--CIVILIAN

A. Physics Development

1. Theoretical Reactor Physics

a. General Fast Reactor Physics

(i) Reactor Dynamics (D. A. Meneley)

Last Reported: ANL-7705, pp. 1-3 (June 1970).

(a) Two-dimensional Kinetics: Point-kinetics Algorithm (E. L. Fuller)

An algorithm for efficiently integrating the point-kinetics model in KIN2D has been developed. It differs from that used in QX1* in that it is capable of accounting for phenomena due to moving precursors. Nevertheless, the structure of the kinetics model is essentially the same, and, as a result, the integration algorithms are fairly similar.

The point-kinetics model for KIN2D is

$$\dot{N} = \left(\frac{\rho - \beta}{\Lambda} + \frac{k_0 - 1}{\Lambda k_0} \right) N + \sum_{s=1}^m \lambda_s \eta_s + \sum_{s=1}^m \lambda_s \xi_s + Q' \quad (1)$$

and

$$\dot{\eta}_s = \frac{\beta'_s}{\Lambda} N - (\lambda_s + \kappa_s) \eta_s, \quad s = 1, \dots, m. \quad (2)$$

The only differences from the traditional point-kinetics model are: k_0 , a steady-state eigenvalue; κ_s , a precursor loss coefficient ($\neq 0$ only after vaporization of fuel has begun); and ξ_s , a moving-precursor contribution to the neutron density. Unlike formulations with fixed precursors,

$$\sum_{s=1}^m \beta'_s \neq \beta$$

(although equality would result if the precursors were fixed).

The first step toward obtaining a solution is to formally integrate Eq. 2 over the time interval $t_{j-1} \leq t \leq t_j$, and substitute the result into Eq. 1. The result is

*Ott, K. O., and Meneley, D. A., Nucl. Sci. Eng. 36, 402 (1969).

$$\begin{aligned}
\dot{N} &= \left(\frac{\rho - \beta}{\Lambda} + \frac{k_0 - 1}{\Lambda k_0} \right) N + \sum_{s=1}^m \lambda_s \left(\eta_s(t_{j-1}) \exp \left\{ - \int_{t_{j-1}}^t [\lambda_s + \kappa_s(\tau)] d\tau \right\} \right. \\
&\quad \left. + \int_{t_{j-1}}^t \exp \left\{ - \int_{t'}^t [\lambda_s + \kappa_s(\tau)] d\tau \right\} \frac{\beta'_s}{\Lambda} (t') N(t') dt' + \xi_s(t) \right) + Q' \\
&= \text{RHS}[N(t)].
\end{aligned} \tag{3}$$

Next, assume the following trial solution for $N(t)$ over the same time interval:

$$\bar{N}(t) = \sum_{k=0}^2 A_k (t - t_{j-1})^k. \tag{4}$$

The parameters A_k are to be determined in order to obtain the solution over the j th time step. This is done by using the method of undetermined parameters, with subdomain weighting. Specifically, construct the residual $R_N(t)$ by substituting $\bar{N}(t)$, as given by Eq. 4, into Eq. 3, to obtain

$$R_N(t) = \frac{d\bar{N}}{dt} - \text{RHS}[\bar{N}(t)]. \tag{5}$$

Then, define the weighting functions to be the unit-step functions

$$V_r(t) = U(t) - U(t - t_r), \quad r = 1, 2, \tag{6}$$

where

$$t_r = t_{j-1} + \frac{t_j - t_{j-1}}{2^{r-1}}. \tag{7}$$

The subdomains are thus the full interval and the half-interval, respectively. The parameters A_1 and A_2 can then be determined by solving the system of algebraic equations that results when the weighted residual criterion

$$\int_{t_{j-1}}^{t_r} V_r(t) R_N(t) dt = 0, \quad r = 1, 2, \tag{8}$$

is used. (A_0 is, of course, equal to $\bar{N}(t_{j-1})$.) The parameters

$$p(t) = \frac{\rho - \beta}{\Lambda} + \frac{k_0 - 1}{\Lambda k_0},$$

β'_s/Λ , ξ_s , and Q' , are fitted to parabolas over the time interval, and κ_s is approximated by a constant over the same time interval. Finally, this algorithm is used in conjunction with a time-step selecting scheme, developed by Kaganove,* that provides a stable, accurate solution.

2. Experimental Reactor Physics

a. Fast Critical Experiments--Experimental Support--Idaho

(i) Neutron Spectroscopy (G. G. Simons)

Last Reported: ANL-7705, pp. 13-17 (June 1970).

Errors in neutron spectra measured with proportional counters resulting from using approximate gamma-ray background data were investigated during the ZPR-3 Assembly 61 spectrum measurements. This assembly offered an ideal testing medium since the gamma-ray background from the hot fuel was very high at the core center. Moreover, spectrum measurements were also made near the core edge and outside the core, where the gamma-ray background was much lower than at the core center. Thus gamma-ray background effects could be studied in a single assembly possessing different degrees of background severity.

Hydrogen- and methane-counter gamma-ray background spectra were accumulated both in the center of ZPR-3 Assembly 61, with the halves apart, several hours after shutdown and with a 30-Hz point ^{60}Co source located about 4 in. away from the side of the detectors but perpendicular to the centerline of the active volumes.

These ZPR-3 in-core and ^{60}Co source produced background-data sets were used to subtract the gamma-ray contributions from the raw data measured in ZPR-3 at Locations 1-P-16, 1-P-11 and 1-P-9. Resulting neutron spectra are shown in Fig. I.A.1.

As shown in the lowest spectra in Fig. I.A.1, the 1-P-16 central spectrum obtained using the ^{60}Co background tapes exhibits serious deviations from the ZPR-3 background subtracted spectrum below 10 keV. For the 1-P-11 interface position (center spectra in Fig. I.A.1), small deviations are evident below 10 keV. At position 1-P-9, the ^{60}Co background results appear to be slightly high below 5 keV. However, these two spectra are generally within the error limits imposed upon each spectrum.

Additional background tests will be run for the ZPR-3 Assembly 62 spectrum measurements. Following completion of these tests,

*Kaganove, J. J., Numerical Solution of the One-group Space-independent Reactor Kinetics Equations for Neutron Density Given the Excess Reactivity, ANL-6132 (Feb 1960).

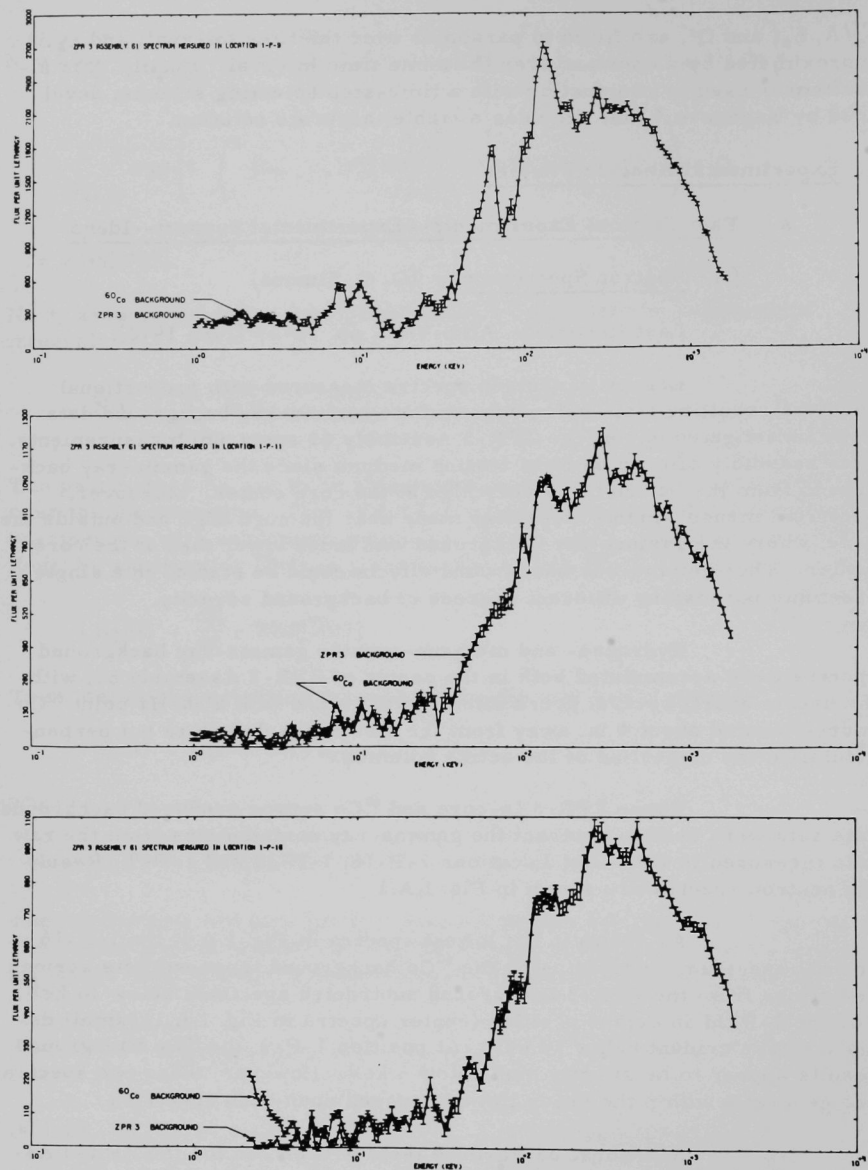


Fig. 1.A.1. Comparison of Neutron Spectra Measured with Proportional Counters When Gamma-ray Background Data Were Measured with a Point ^{60}Co Source and in the ZPR-3 Assembly 61 at Cell Locations 1-P-9, 1-P-11, and 1-P-16

specific details of gamma-ray background-induced errors relative to the in-core gamma-to-neutron fields will be reported for hydrogen- and methane-filled proportional counters.

(ii) Maintenance of Support Techniques and Facilities
(D. W. Maddison)

(a) Measurement of Manganese and Sodium Activation in ZPPR/FTR-2 Shield Configuration*

Last Reported: ANL-7661, pp. 4-8 (Jan 1970).

The counting efficiency for ^{24}Na in $2 \times 2 \times 1/4$ -in. sodium plates has been carefully evaluated experimentally. To properly relate the absolute manganese reaction rates to the sodium reaction rates previously reported, all the sodium reaction rates should be divided by 1.985 ($\pm 2.2\%$). This correction, however, should not be applied to the sodium reaction rates reported in conjunction with the plutonium fission rates (Table I.A.5 of ANL-7661).

This factor (1.985) includes all corrections for gamma attenuation and sample configuration, which were not included in the value reported earlier.

b. Fast Critical Experiments--Experimental Support--Illinois

(i) Computer Applications (C. E. Cohn)

Not previously reported.

Small computers are coming into use for data acquisition and control in nuclear power plants and laboratories. It helps in planning such applications to know the time required for certain elementary operations on various computers, which indicates how much real-time computational load may be carried by a given machine.

Such information has been obtained from speed tests on a limited but representative selection of small computers. The selection included the computers used in the Applied Physics Division for on-line data handling, as well as some others that were available for tests. The tests were done to assist in computer selection for the Division or to assist in evaluating past selections. A special program was written in FORTRAN, a popular process-control language, to test the speed of various single-precision floating-point operations and functions. Each operation was tested in a DO loop which repeated it many times (500 to 200,000 depending on the particular operation) with different operands. The loop was preceded and followed by PAUSE.

*Previously reported as part of Selected Differential and Integral Data.

On PDP-9, CDC-1700, and IBM-1130, loops were timed by a stopwatch. On all others except SEL-840MP, a 3-in./sec recorder was connected to the halt light. On the SEL-840MP, timing was done with an interfaced binary scaler and a clock generator.

For each loop, gross time per operation was total time over number of cycles. To obtain net time shown, the DO cycle time was subtracted. Sine, square-root, and natural-logarithm operations required subtraction of the time for an add operation used in forming the argument.

Table I.A.1 shows parameters of the computers tested; Table I.A.2 shows measured operation times. All machines have hard-wired fixed-point multiplication and division, and all but the SEL-840MP with EAU use subroutines to perform floating-point arithmetic. Also shown is the amount of memory occupied by the timing program and its binary subroutines. Practically all of the memory is occupied by instructions; only

TABLE I.A.1. Computer Parameters

Computer	DDP-224	SEL-840MP	PDP-9	DATA-620	SEL-810A	CDC-1700	IBM-1130	DDP-516
Bits per word	24	24	18	16	16	16	16	16
Memory cycle time, μ sec	5.0	1.75	1.0	1.8	1.75	1.1	3.2	0.96
Memory occupied by timing program and library subroutines		Non-EAU	With EAU					
Words:	953	1129	881	1907	1622	1845	2078	1636
Bits:	22872	29496	21144	29070	30512	29520	33248	26176

TABLE I.A.2. Operation Times, μ sec

Computer	DDP-24 ^a	SEL-840MP		PDP-9	DATA-620 ^b	SEL-810A ^c	CDC-1700	IBM-1130 ^d	DDP-516 ^e
		Non-EAU	With EAU ^f						
Add	440	308	19	500	518	553	540	850	245
Divide	413	383	37	580	790	2622	720	1130	270
Multiply	369	282	26	500	732	611	550	960	250
Sine	584	4970	365	5235	3396	9862	4540	3600	2375
Square root	377	824	267	4085	806	13459	8440	5070	535
Exponential	1188	3009	470	6385	1916	N.A.	3340	2833	2105
Log	548	5887	373	4785	4576	11262	5940	5500	2725
If	28	11	11	90	24	85	190	200	36
Fix	130	79	33	160	260	162	330	370	224
Float	105	50	8	160	356	615	760	540	312
Store subscripted variable									
1-dimension	196	77	28	240	53	192	370	640	89
2-dimension	221	88	39	300	242	213	380	750	124
DO (1 cycle)	43	18	18	15	266	18	16	52	10

^aResults also apply to DDP-124 if operation times are multiplied by 0.34 and 40 μ sec are added for ADD, DIVIDE, MULTIPLY, SINE, LOG, and EXPONENTIAL. Increase memory requirement by 20 words.

^bResults also apply to DATA-620/i.

^cResults also apply to SEL-810B if operation times are multiplied by 0.45.

^dResults also apply to IBM-1800 if operation times are multiplied by 0.625 for the 2- μ sec memory or 1.25 for the 4- μ sec memory. Re-entrant software may run slower.

^eResults also apply to DDP-116 and H-316 if times are multiplied by 1.82.

^fEAU = Extended Arithmetic Unit (hardware floating point).

about two or three dozen words are for data. The program occupies about the same number of memory bits, regardless of word length, implying that a shorter word produces no savings in memory cost for a given job.

Various factors produce the observed disparities in speed. On some machines the sine, square-root, and logarithm subroutines are themselves programmed in FORTRAN, so the approximation algorithms are executed in floating-point arithmetic. Also, the SEL-840MP carries 11 significant figures in its single-precision floating-point arithmetic, while the others carry just six or seven. Evidently, the third-generation short-word machines do not yield the computational speed that their fast memory cycles would lead one to expect.

These results might be considered representative solely of FORTRAN programs or floating-point arithmetic, and not applicable to typical control applications programmed in machine language and performing various types of data manipulation. However, that view is not wholly valid. Much of the elapsed time in these measurements, particularly in the arithmetic operations and functions, is spent executing hand-coded library subroutines, and only a small fraction is spent executing compiler-generated code. Floating-point arithmetic might be considered simply as one type of data manipulation where the bit patterns known as the "floating-point arguments" are operated upon a prescribed way to obtain another bit pattern known as the "floating-point result." The relative efficiency of this type of data manipulation can be taken as an index of the relative efficiency of other types of data manipulation. Actually, FORTRAN is the only practical way to make such comparisons on a wide range of computers with a reasonable expenditure of effort.

Maximization of speed could have a significant adverse effect on system reliability only through increase of memory or logic speeds to the threshold of the state of the art. Optimization of hardware or software architecture would not significantly affect intrinsic reliability.

These results imply that the popular 16- and 18-bit word lengths are less cost-effective than a 24-bit word length.

3. ZPR and ZPPR Operations and Analysis

- a. ZPR-6 and -9 Operations and Maintenance (R. A. Karam and G. K. Rusch)

Not previously reported.

Preparation of the ZPR-6 facility for operation with the plutonium-fueled Assembly 7 has been completed. All the plutonium fuel plates estimated to be needed for this assembly have been received,

processed, and stored in the Building 316 vault. Loading of the assembly has progressed to the first multiplication step at 408 kg fissile. Estimated critical mass for Assembly 7 is 1245 kg.

b. Fast Critical Facilities Experiments and Evaluation--Illinois

(i) Clean Critical Experiments (R. A. Lewis)

Last Reported: ANL-7705, p. 25 (June 1970).

Preanalysis of ZPR-6 Assembly 7 is nearly complete. The preanalysis will consist of a predicted value for each parameter that will be measured as part of the Assembly 7 experimental program and will include additional information, such as drawer worths at various core locations, which is operationally useful. MACH-1 one-dimensional diffusion calculations and a cross-section set generated by the MC² code from the ENDF/B tape are being used for the calculations. The cross sections have been corrected for plate heterogeneity using both equivalence theory in the resonance region and S_N flux and volume weighting.

(ii) Mockup Critical Experiments (J. W. Daughtry)

Last Reported: ANL-7705, pp. 26-28 (June 1970).

(a) Status of the FTR-3 Experiments. The status of the program of experiments designated FTR-3 being performed on ZPR-9 was last reported as of the end of May 1970. Since that time, Steps 6 and 7 of the Detailed Plans for the FTR-3 Experiments have been completed. In Step 6, the radial and axial shape of the fission rates of ²³⁹Pu and ²³⁸U and the (n, α) reaction rate of ¹⁰B were measured. The radial distribution was measured at two axial positions, and the axial distribution was measured at two radial positions.

In Step 7 of these experiments, fission-rate ratios were measured near the center of the core for ²³⁹Pu/²³⁵U, ²³⁸U/²³⁵U, and ²⁴⁰Pu/²³⁵U using fission counters. The ratio of the ²³⁸U capture rate to the ²³⁵U fission rate was measured by foil activation. In addition, a measurement was made using counters to determine the ratio of the ¹⁰B(n, α) reaction rate to the ²³⁵U fission rate.

Upon completion of Step 7 of the plans, the assembly was returned to the reference FTR-3 configuration for Step 8, which is a series of measurements of the reactivity worths of various control configurations. The reference configuration for Step 8 is essentially the same as that described in earlier progress reports* with a number of minor modifications:

* Reactor Development Program Progress Reports: December 1969, ANL-7655, pp. 10-13; January 1970, ANL-7661, pp. 15-16; February 1970, ANL-7669, pp. 27-30.

(1) New safety and control-rod configuration--One additional ^{10}B safety rod was added in the stationary half at matrix location S 16-23 to provide additional shutdown margin by rod action in this assembly. Several fuel-bearing control rods were moved to new locations so that they would not be in matrix locations that had been selected for simulated closed loops in a later step of the FTR-3 experiments. When the fuel-bearing rods are fully inserted they do not cause a significant perturbation to the core configuration. However, the core is perturbed slightly by a ^{10}B rod installation. A stainless steel sheath is inserted in the matrix tube to provide a channel in which the ^{10}B rod moves. A special narrow drawer is loaded into the matrix tube next to the ^{10}B rod sheath. The inside dimensions of the drawer are: 2 in. high by $1\frac{1}{2}$ in. wide, compared to the 2 x 2-in. dimensions of the standard drawer. Atom densities were given in the January 1970 progress report* for a matrix tube containing a ^{10}B rod channel and a narrow drawer with modified outer core composition.

(2) Additional flux-detection devices--In Step 8 of these experiments, the inverse-kinetics method is being used to determine the subcriticality of each configuration of interest. In addition, four ^{235}U fission counters and one compensated boron ion chamber have been placed at various locations within the reflector regions of the assembly. The counting rates of the fission counters and the ion chamber current will be recorded at each subcritical level in this series of experiments.

Each fission counter is approximately 10 in. long and 2 in. in diameter. The ion chamber is approximately 6 in. long and 2 in. in diameter. Table I.A.3 gives the location of these instruments in the assembly. The "distance from the interface" heading gives the distance from the interface of the reactor halves to the nearest end of each detector.

TABLE I.A.3. Locations of Fission Counters and Ion Chamber for Step 8 of the FTR-3 Experiments

Type of Detector	Matrix Location	Radius, cm	Distance from Interface, cm	Region
Fission counter	M 32-32	70.4	0	Radial reflector
Fission counter	S 13-13	78.2	0	Radial reflector
Fission counter	S 13-33	78.2	45.7	Radial reflector
Fission counter	S 27-19	31.3	62.0	Axial reflector
Ion chamber	M 23-23	0	62.0	Axial reflector

*Reactor Development Program Progress Report, ANL-7661, January 1970, p. 15.

(b) Small Sample Worth Measurements in ZPR-9 Assembly 26, FTR-3. This experiment was described in detail on pages 26-28 of the previous monthly report. This follow-up report gives details not available at that time.

(1) Sample Worths by the Period Method. The set of samples used for central worth measurements in FTR-3 contained four samples with reactivity worths too large to be measured by the oscillation-autorod method. The worths of these samples were obtained from positive period measurements by the Hurliman-Schmid method* using a DDP-24 computer on-line. The sample descriptions are given in Table I.A.4. The results of the measurements are given in Table I.A.5. These results are preliminary, since various aspects of these measurements are still under investigation. The results of these investigations will be included in future reports.

TABLE I.A.4. Perturbation Sample Descriptions

Sample Identification	Material Element or Isotope	State	Geometry	Dimensions, in.			Sample Weight, g
				OD	Thickness	Length	
B-1	¹⁰ B	Powder	Cylinder	0.401	-	2.174	4.1928
B-5	¹⁰ B	Powder	Annulus	0.400	0.040	2.173	1.8370
B-6	¹⁰ B	Powder	Annulus	0.401	0.020	2.173	0.9562
MB-22	²³⁵ U	Solid	Annulus	0.835	0.030	1.6875	30.83795

TABLE I.A.5. Sample Worth Results from Period Evaluation

Sample Identification	Capsule Worth, 1h	Standard Deviation, ^a 1h	Sample Worth, 1h	Standard Deviation, 1h	Specific Worth, 1h/kg	Standard Deviation, 1h/kg	Radius, in.	Stainless Steel, g
B-1	-15.026	0.16	-14.88	0.16	-4322	38	0.0	20.503
B-5	-7.589	0.16	-7.40	0.16	-4027	87	0.0	21.4545
B-6	-4.328	0.16	-4.13	0.16	-3550	167	0.0	28.0564
MB-22	+5.225	0.16	+5.55	0.16	+179.9	5.2	0.0	48.06814

^aExperimenters' estimated error based on autorod calibration using the same technique.

(2) Additional Sample-composition Data. Additional information has been obtained on the compositions of samples used in the FTR-3 small-sample measurements. The tantalum samples can be considered to be pure natural tantalum which is 99.988 at. % ¹⁸¹Ta. The iron, Fe₂O₃, aluminum, and Al₂O₃ samples may be treated as pure elements or compounds with naturally occurring isotopic abundances. The boron samples are 92.88 wt % ¹⁰B. The sample designated MB-22 is enriched uranium with the composition given in the June monthly progress report.

*Hurliman, T., and Schmid, P., Nucleonik 5, pp. 236-239 (1963).

(iii) Heterogeneity Measurements (R. A. Lewis)

Last Reported: ANL-7606, pp. 21-23 (Aug 1969).

(a) VTRZ Project. The Variable Temperature Rodded Zone Project has progressed to the procurement and fabrication phase. Fabrication of the VTRZ itself is approximately 15% complete. Fabrication of the associated calandria cans is complete, and the fabrication of the associated oxide fuel rods is about 50% complete.

The VTRZ Final Safety Analysis Report has been formally submitted to the AEC for review after completion of all internal ANL technical and safety reviews. The VTRZ FSAR (ANL-7638), Design Summary Report (ANL-7639), and a revised ZPR-6 and -9 Operating Limits Document (revised to include the VTRZ in ZPR-6) are now available in approval copy form.

c. Fast Critical Facilities Experiments and Evaluation--Idaho(i) Clean Critical Experiments (P. I. Amundson)

Last Reported: ANL-7705, p. 29 (June 1970).*

(a) ZPR Assembly 2 (R. E. Kaiser)

Modifications to the ZPPR Assembly 2 reference loadings, required to provide a better match between plate and future pin-zone compositions, have been completed. The modified reference core is only slightly more reactive than its predecessor, and the core outline, shown in Fig. I.A.2, remains the same. The radial blanket is now represented as a two-zone region, where the inner zone contains essentially all 1/2-in. sodium plates and the outer zone contains pairs of 1/4-in. sodium plates. The basic drawer-loading pattern is the same in both blankets, but the difference in the type of sodium plate used to make up the 1/2-in. column causes a noticeable difference in the atom densities of sodium and the components of stainless steel, as can be seen in Table I.A.6, which gives the atom densities for the modified core. Figures I.A.3 and I.A.4 show the configurations of the two halves of the "as-built" assembly, which includes two spiked control rods. The axial dimensions given include the thickness of the drawer fronts, which have been homogenized into the core compositions.

The corrected critical mass has been evaluated according to procedures described in earlier reports, and is given in Table I.A.7. The inner-core atom densities with normal control drawers

*Previously reported under ZPR-3 and ZPPR Operations and Analysis.

in place of the spiked control drawers are listed in Table I.A.6, and the configuration of the cylindrical "corrected" heterogeneous reactor, adjusted to 22°C, is presented in Figs. I.A.5 and I.A.6.

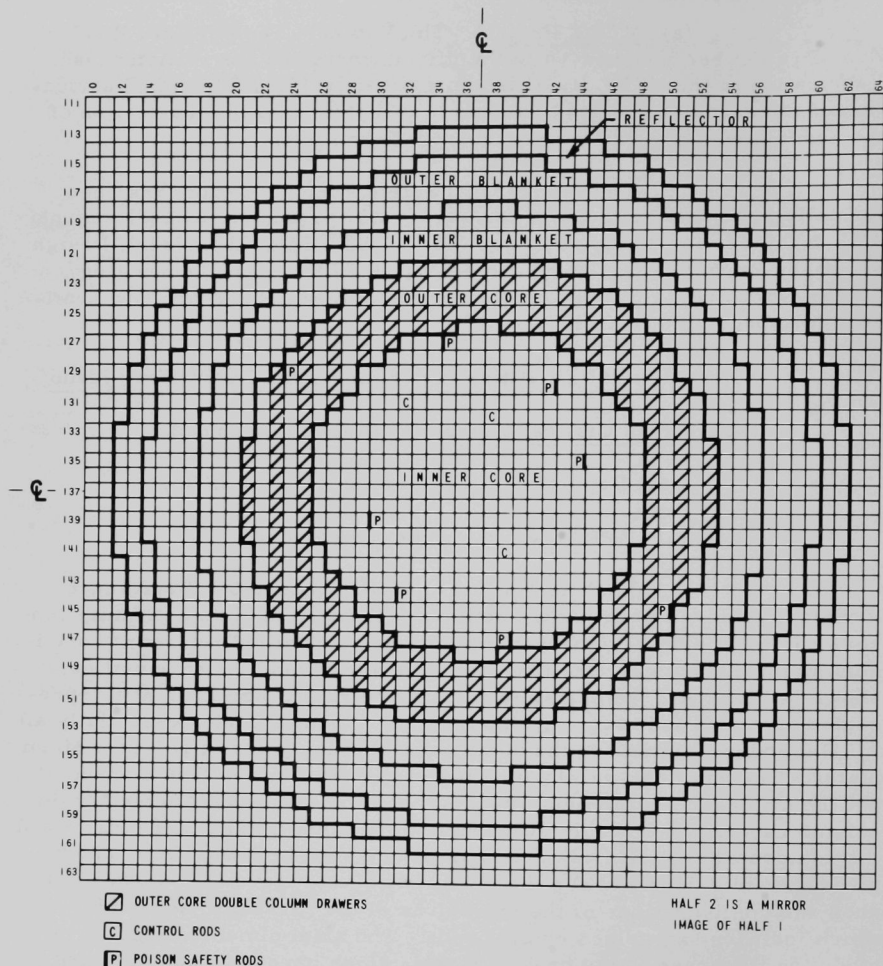
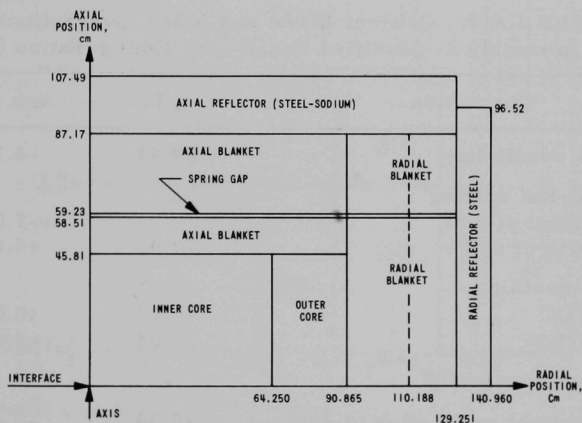


Fig. I.A.2. ZPPR Assembly 2--Reference Loading with Equal Zone Volumes (modified)

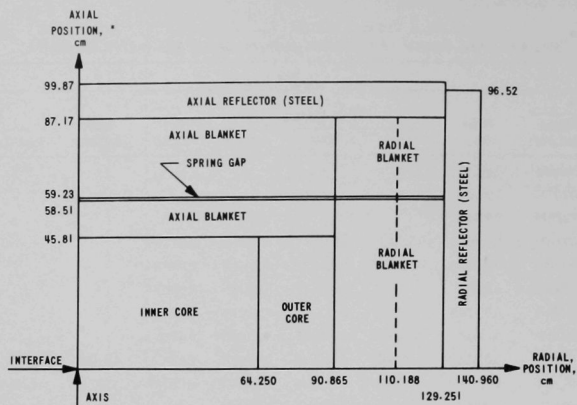
TABLE I.A.6. Atom Densities for the Modified Equal-zone Configuration of ZPPR Assembly 2

Isotope	$\times 10^{24}$ atoms/cc									
	Inner Core		Outer Core	Radial Blanket			Axial Blanket	Radial Reflector	Axial Reflector	
	As-built	Without Spiked Rods		Inner	Outer	Average			Steel (5 in.)	Na-Steel (8 in.)
^{239}Pu	0.0008477	0.0008456	0.0012757	-	-	-	-	-	-	-
^{240}Pu	0.0001123	0.0001120	0.0001689	-	-	-	-	-	-	-
^{241}Pu	0.0000174	0.0000173	0.0000260	-	-	-	-	-	-	-
^{235}U	0.0000123	0.0000123	0.0000116	0.0000243	0.0000243	0.0000243	0.0000153	-	-	-
^{238}U	0.0055723	0.0055702	0.0052068	0.0110242	0.0110242	0.0110242	0.0069369	-	-	-
Na	0.0088143	0.0088203	0.0085986	0.0063641	0.0059302	0.0061297	0.0086369	-	-	0.0089848
O	0.0131489	0.0131476	0.0117808	0.0200210	0.0200220	0.0200216	0.0137264	-	-	-
Mo	0.0002188	0.0002182	0.0003285	0.0000014	0.0000018	0.0000016	0.0000014	-	-	0.0000014
Fe	0.0125475	0.0125377	0.0138252	0.0070048	0.0076214	0.0073379	0.0101762	0.0717099	0.0727580	0.0332218
Ni	0.0013158	0.0013156	0.0012556	0.0009984	0.0010878	0.0010467	0.0012837	0.0005904	0.0007971	0.0019245
Cr	0.0027001	0.0026995	0.0025239	0.0020113	0.0021910	0.0021084	0.0026491	0.0012001	0.0016304	0.0044841
Mn	0.0002083	0.0002082	0.0002008	0.0001573	0.0001743	0.0001665	0.0002174	0.0005934	0.0006247	0.0005167
Si	0.0001472	0.0001472	0.0001296	0.0001061	0.0001139	0.0001103	0.0001435	0.0000636	0.0000888	0.0002365
C	0.0000061	0.0000061	-	0.0009860	0.0009864	0.0009862	0.0000133	0.0005398	0.0005386	0.0001914



*Includes drawer fronts.

Fig. I.A.3. As-built ZPPR Assembly 2--Equal-zone Configuration--Half 1



*Includes drawer fronts.

Fig. I.A.4. As-built ZPPR Assembly 2--Equal-zone Configuration--Half 2

TABLE I.A.7. Critical Mass and Mass Corrections in ZPPR Assembly 2--Modified Equal-zone Configuration (50/50)

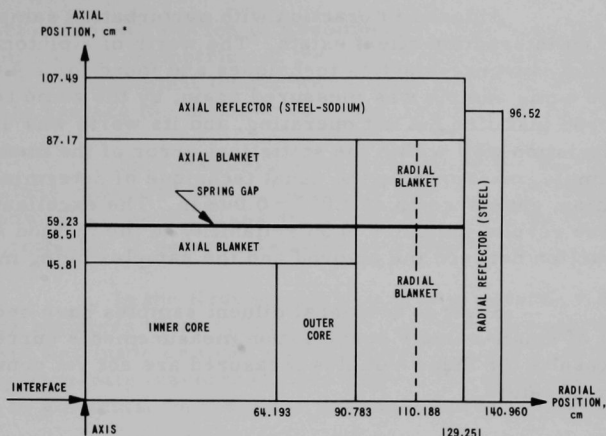
Correction	ρ, Ih	Δm (equiv)
Excess reactivity	69.43	-4.14 kg
Control-rod spiking		
Amount of fuel	-	-1.0 kg
Worth of spike	77.42	+4.62 kg
Edge smoothing		
IC/OC	-0.03	+0.002
OC/RB	+0.04	-0.002
Interface-gap worth	-	-0.11 kg
Temperature correction to 22°C	+9.34	-0.1 kg

Loaded $^{239+241}\text{Pu}$ mass = 1019.7 ± 1.0 kg.

Total correction = -1.2 ± 0.1 kg.

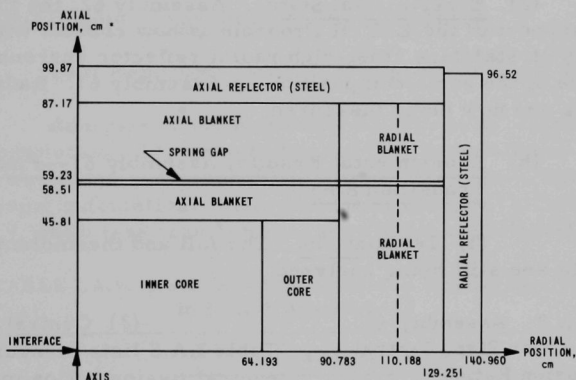
Corrected critical mass = 1018.5 ± 1.0 kg $^{239+241}\text{Pu}$.

Heterogeneous cylindrical reactor at 22°C.



*Includes drawer fronts.

Fig. I.A.5. ZPPR Assembly 2--Equal-zone Configuration Adjusted for Critical-mass Corrections--Half 1



*Includes drawer fronts.

Fig. I.A.6. ZPPR Assembly 2--Equal-zone Configuration Adjusted for Critical-mass Corrections--Half 2

Selected central-perturbation measurements were repeated in the modified core and compared with the same samples as measured before the change. The worths of tantalum, ^{10}B and selected plutonium samples showed a change of only 1% or less, which is within the expected error in the measurement. The ^{238}U fission traverse, reported in the previous monthly progress report, has been checked, and no significant change was noticeable. Further checks will be performed with ^{239}Pu and ^{235}U traverse counters.

Autorod interaction with perturbation samples was checked, and no interaction effect exists. The worth of a plutonium sample was measured by inverse-kinetics techniques and found to be 4.084 ± 0.018 Ih. The same sample was measured again, by the same technique, with the autorod installed but not operating, and its worth was 4.078 ± 0.017 Ih, a deviation well within the statistical error of the measurements. The same sample, measured by the usual technique of determining average autorod position, gave a worth of 4.079 ± 0.005 Ih. The excellent repeatability of these results indicates good reliability in the method and complete lack of interaction between the autorod and the samples being measured.

Several additional diluent samples have been measured in the series of small-sample perturbation measurements currently in progress. Results for these samples measured are not yet complete and will be reported later.

- (ii) Mockup Critical Experiments (W. P. Keeney, R. O. Vosburgh, and D. Meneghetti)

Last Reported: ANL-7705, pp. 31-38 (June 1970).*

(a) Experimental Status. Assembly 62, the third critical assembly in support of the EBR-II Program is now critical with a nominal two-drawer-thick stainless steel-rich radial reflector surrounding a quasi-hexagonal core of the same composition as Assembly 61. Radial reaction-rate traverses are now being measured.

- (b) Experimental Results, Assembly 61--Final Transition Step

(1) Irradiations. The foil and thermoluminescence dosimeter data are still being analyzed.

TABLE I.A.8. Assembly 61,
Final Transition Step, Central
Fission Ratios

Isotope	Experimental Ratio
$^{238}\text{U}/^{235}\text{U}$	0.0680
$^{234}\text{U}/^{235}\text{U}$	0.4350
$^{233}\text{U}/^{235}\text{U}$	1.5727
$^{236}\text{U}/^{235}\text{U}$	0.1486
$^{239}\text{Pu}/^{235}\text{U}$	1.2276
$^{240}\text{Pu}/^{235}\text{U}$	0.4669

- (2) Central Fission Ratios.

Table I.A.8 lists measurements of central fission ratios made with the spherical back-to-back chambers in 1-P-16 at the core center. The drawer loading diagrams for the drawer containing the counter will be published in the next compilation of loading drawings.

- (c) Assembly 62--Description.
Assembly 62 is a continuation of the

*Previously reported as part of ZPR-3 and ZPPR Operations and Analysis.

radial reflector-blanket studies of Assembly 61. The core composition and the compositions and geometries of the axial reflectors of Assembly 61 have been retained, but a nominal four-drawer-thick stainless steel-rich radial reflector is to replace the nickel-rich radial reflector of Assembly 61.

This stainless steel-rich reflector, having approximately the same composition (i.e., identical number of columns of stainless steel and sodium) as the stainless steel zone above and below the previous nickel-rich reflector is being installed in two steps.

In the first step, which is now critical, a nominal two-drawer-thick stainless steel reflector surrounded by the uranium-sodium radial blanket was made critical with the quasi-hexagonal core. After a set of radial reaction-rate traverses is performed, the stainless steel reflector is enlarged to a nominal four-drawer thickness in the second step.

(d) Assembly 62, First Step, Experiments. Assembly 62 is critical with the two rows of stainless steel-rich reflector in place. The critical loading, uncorrected for excess reactivity is 229.6 kg of ^{235}U . Edge worth measurements have been made and are now being analyzed.

(iii) Doppler Experiments (R. E. Kaiser)

Last Reported: ANL-7705, pp. 29-31 (June 1970).*

Analysis of the Assembly 53 reactivity Doppler experiments is nearing completion. The results for the UO_2 sample were redone after a discrepancy was found in the cross sections used in the original library for the 2-D diffusion calculations. The results of the new calculation, presented in Table I.A.9, show less than 10% deviation from experiment in all cases.

TABLE I.A.9. Results of UO_2 Reactivity Doppler Analysis in ZPR-3 Assembly 53

ΔT , °K	Reactivity, $\text{Ih/kg } ^{238}\text{U}$		
	Calculated	Experimental	C/E
300-500	-4.76	-4.43 ± 0.04	1.074
300-800	-9.72	-9.54 ± 0.04	1.019
300-1100	-14.56	-13.62 ± 0.04	1.069
300-total sample worth	-67.6	-59.1 ± 1.2	1.144

*Previously reported as part of ZPR-3 and ZPPR Operations and Analysis.

Calculation of total sample worth was determined as 10 times the worth of a 10% reduction in atom density in the gross sample, and differed from the measured worth by only 14.4%. The ratio of calculation to experiment is always greater than one, as expected, and the differences compare favorably with previous analyses.

The technique used Schmidt's parameters for resolved ^{238}U resonances and statistically generated resonances in the unresolved region (up to 25 keV) which were based on average parameters given by Schmidt. Both s- and p-wave resonances were included. Group cross sections as a function of temperature were obtained from the RABBLE code, where the s-wave cases were run first, and the results used as constant-background cross sections for the p-wave calculations. The two p-wave sequences were run together, allowing for interference effects between sequences.

The calculations of the reactivity effects were performed with the 2-D diffusion and perturbation modules of the ARC system. Core cross sections for this calculation were obtained from a homogeneous MC^2 run, and the basic cross sections for the sample and the steel regions around the sample were obtained from a heterogeneous MC^2 case with a UO_2 pin surrounded by steel, weighted over the fluxes from the homogeneous case. A similar analysis of the PuO_2 Doppler experiment in Assembly 53 is nearing completion and will be reported soon.

4. ZPR Materials

a. ZPR Materials Procurement (A. B. Shuck and F. B. Huke)

Last Reported: ANL-7688, pp. 55-64 (April-May 1970).

This report supplements the comprehensive report on the ZPR program in ANL-7688. Since then the FY-1970 procurements of experimental materials were completed. Preproduction and process variability studies were completed, and production was started on $(\text{U,Pu})\text{O}_2$ fuel rods at Kerr-McGee Corporation (KM).

(i) Process Materials. As of July 29, plutonium nitrate containing 87.768 kg of plutonium has been prepared by Atlantic Richfield Hanford Corporation (ARHCO) and shipped by the AEC to the KM plutonium plant. Four of the five shipments were certified to be within ANL Specification PF-1615 requirements. The total metallic impurities in the third shipment were stated to be 43 ppm above specification by the ARHCO analysis. The KM analysis showed the total metallic impurities to be within specification, and the shipment was accepted and cross-blended with other lots of lower metallic impurity.

(ii) Scrap Recovery from Metallic Fuel Fabrication. By July 29, NUMEC had shipped nitrate containing 287.38 kg of plutonium. Of this, 268.70 kg was recovered from the 11.5% ^{240}Pu composition and 18.68 kg from the 25.8% ^{240}Pu composition. Additionally, 6 kg of the latter were bottled awaiting analysis. ARHCO analysis found a number of bottles of nitrate to be out of specification with respect to iron, nickel, chromium, or total metallic impurities. Since this nitrate is being reblended for the KM contract, this causes additional difficulty in meeting Specification A2A for nitrate supplied to KM.

NUMEC has recovered only the high-yield residues. The company has not yet set up the incinerator and related plant equipment necessary to process combustible and low-yield residues, which records indicate may contain 6-8 kg of plutonium.

(iii) (U,Pu) O_2 Fuel Rods

(a) License. Contract No. 31-109-38-2313 between KM and ANL is for fabrication of 12,700 fuel rods containing oxide of 13.35 wt % plutonium and 5900 rods containing oxide of 26.7 wt % plutonium. KM completed a plutonium plant during calendar year 1969, but licensing problems delayed operation with plutonium. A limited license was received on February 20, 1970, allowing 300 g of plutonium for laboratory use. A production license was received on April 2, 1970. The first production quantities of plutonium were received under this license on April 20 and 28.

(b) Development of Analytical Methods. ANL has assigned an experienced plutonium analyst to follow and evaluate analytical controls at KM and at ANL. The analytical methods being used by the two organizations are as follows: KM determines plutonium by means of the coulometric method, while ANL uses amperometric titration. Both organizations use amperometric titration for determination of uranium. X-ray fluorescence is employed as a rapid secondary method for determining the U/Pu ratio for process control. KM is determining the oxygen-to-metal (O/M) ratio gravimetrically by oxidation and reduction techniques. KM analysts are determining nitrogen by the microkjeldahl method and hydrogen by hot-gas extraction followed up by mass spectrometry. ANL uses the inert-gas fusion method for the direct determination of oxygen, nitrogen, and hydrogen. Total metallic impurities are determined spectrographically at KM by the carrier-distillation method and at ANL by the copper-electrode-spark technique. Both organizations extract chlorine and fluorine by pyrohydrolysis and determine the concentration by means of specific ion electrodes.

(c) Development of Production Methods. The specifications called for a two-stage qualification-of-process for manufacture of the (U,Pu) O_2 fuel rods. The first stage called for laboratory-scale experimental

production to establish process parameters and to make a limited number of preproduction pellets and fuel rods. The second state as a full-scale process run of approximately 10,000 fuel pellets, upon which not less than 10 samples were to be analyzed in duplicate and not less than 1000 pellets measured in detail. The data from these are statistically evaluated to determine whether the product variations were within specified limits. These requirements were modified very slightly because of the delay in the program, to allow stepwise approval of sequential process steps of coprecipitation, calcining, pellet making, loading, welding, and inspection.

KM used a 250-g laboratory batch to establish the concentration, pH, temperature, and other parameters needed to coprecipitate ammonium diuranate-plutonium hydroxide and the calcining temperature and atmosphere to convert this to $(U,Pu)O_2$. These parameters were applied successfully to the continuous precipitation operation, and a uniform coprecipitate of the desired U/Pu ratio was produced on the first semiworks scale batch of about 15 kg of Pu. The only difficulty experienced was with plutonium concentration variation caused by holdup in delivery pipes. Piping changes corrected this condition.

The first calcining operation on a portion of the filtered coprecipitate was processed through the calcining operation at 800°C . This material, which was produced as a "gray-green" oxide, was found to be excessively surface-active. When exposed to air, it quickly oxidized to the "brown" oxide state. Successive portions were calcined at 825, 850, 875, and 900°C . A finishing temperature of $850\text{--}900^\circ\text{C}$ was required to produce air-stable oxide from this batch. The lower temperature may be used if the oxide is fully cooled before exposure to air.

Attempts were made to pellet the as-calcined oxide, but the powder was insufficiently free-flowing to feed through the shuttle feeders on the presses. The oxide was, therefore, granulated by cold-pressing into 0.600-in.-dia compacts, which were then granulated through an 18-mesh granulator screen. The fines were removed by sieving, and this product was fed through the shuttle feeder on the presses. A production-scale oxide lot run was authorized on June 3.

(d) Pellet Pressing. The pellets were pressed in 0.400-in.-dia dies on a double-acting hydraulic pelleting press. The filling position of the lower-punch ram pressures and closing speeds were each individually variable. The lower-punch fill position was adjusted to produce a green pellet weighing 8.9-9.1 g. Pressures were varied from 2 to 6 tons. The best results were achieved at between 3 and 4 tons pressure with about $1/4$ ton more on the upper ram than on the lower ram. The actual ram pressures to be used on any given batch of material must be determined by the pellet measurements from a pilot lot of pellets pressed and fixed from any given batch of powder. Equal pressures on top and bottom rams

resulted in pellets that were tapered 0.004 to 0.006 in. from top to bottom. Pressure compensation produced pellets with a slight hourglass configuration within the 0.006 limit allowed.

The (U,Pu)O₂ pellets could be fired at 1575-1650°C furnace temperature; the UO₂ pellets had required 1675-1700°C. The fired (U,Pu)O₂ pellets were much more resistant to chipping than the UO₂ pellets and were within the desired density range. The diameter was well controlled in the bottom half of the specified tolerance. This was desirable for fuel-rod loading. The diameter could be controlled by controlling the density of green pellets. The U/Pu and O/M ratios were within specified limits. After observing these results, ANL representatives, on June 18, authorized a production-scale pellet run for the process variability study.

(e) Pellet Loading. KM had simulated pellet-loading operations with UO₂ pellets, but initially had trouble in loading (U,Pu)O₂ pellets without contaminating the jackets and welds. Loading was done by means of a through-the-wall fixture in a partitioned glovebox. The pellet stack was made up premeasured, weighed, and placed on the loading fixture. The jacket was placed in alignment with the pellet stack on the opposite side of the partition in a counter-bored fitting. The pellets were then pushed through a funnel into the jacket. The contamination problem was reduced by redesign of the lip of the funnel so that it extended past the weld area of the jacket tube. The loaded jacket was then removed from the fixture, and the spacer seated on top the pellets. This spacer has six flutes that grip the jacket wall to hold it in place. The jacket was wiped with a gun patch moistened in ethanol to reduce any surface contamination, and the top end was alpha-monitored. If contamination-free, the top plug was installed and the fuel rod was transferred to the welding glovebox.

(f) Welding. The weld configuration was identical to that of the previously made UO₂ rods. The modified Merrick-Miller power sources were used. The welding machines were rebuilt with micrometer adjustments on the torch holder and precision bearings and spindles installed on the collet rotators. With these improvements, there was no difficulty in qualifying five welding operators.

(g) Testing and Inspection. Two new items of test apparatus were built for testing the (U,Pu)O₂ rods--an internal pressure tester and a leak-detection chamber with hot and cold zones. The internal pressure tester is a close-fitting, heatable pressure chamber in which the element to be tested is placed. The chamber is filled with inert gas and heated to 600°C. The pressure is adjusted to 300 psig. The valves are closed, and the fuel rod perforated. If the internal pressure of the fuel rod at 600°C is below 300 psig, the pressure in the chamber drops when the rod is perforated; if it is above 300 psig, the pressure rises. Calculations and tests with rods

to which water has been added have shown that large quantities of condensable materials would be needed to exceed 300-psig internal pressure.

The leak detection chamber was of T configuration--one leg of the T heated, the other water-cooled. The base of the T was connected to a pumping system and a helium M/S leak detector. In the test, a carrier of 25 rods is first leak-detected in the cold chamber. If no leaks are detected, the rods are transferred to the hot zone and the leak detector observed for leak indication. The cycle time has been found to be about $2\frac{1}{2}$ hr. To date, all leaks indicated in the hot leg have also been indicated in the cold leg of the chamber.

The visual and dimensional inspection equipment was well characterized during UO₂ rod production. Although new gauges have been made, they are similar to those used previously. The drops through the gauges were certified by the gauge builder and checked against gauge standards. Setting standards calibrated against gauge blocks were used to set dial indicator and air gauges.

(h) Product Variability Study. The specification required a detailed measurement and analysis of the first 10,000 pellets produced to determine whether the contractor's process is capable of meeting the product specification. Pellet composition and analytical methods were checked by a random sampling of each of the 50 boats passing through the sintering furnace. This was done by means of a numbered grid placed over the boat. Two adjacent samples were selected from the grid position indicated by a random number table. One of the two samples was sent to ANL. The other was held at KM. Ten samples were analyzed in duplicate by KM. Five of these were of split pellets, half of which were sent to ANL for interlaboratory comparison analysis. Two samples from the split pellets were also sent to AVCO and ANL mass spectrometry laboratories for comparative isotopic analysis. A statistical summary of the comparative lot analyses is shown by Table I.A.10. The results of the split-pellet analyses are given by Table I.A.11.

A comparison of the results from both laboratories shown in Table I.A.10 indicates that the KM process is generally capable of making (U,Pu)O₂ pellets that meet specification. Further work needs to be done to bring some analytical determinations into better agreement.

The determinations of major constituents--plutonium and uranium--by statistical analysis may be biased, based on the limited amount of information developed to date. Paired t-tests were made according to the relation

$$t = \frac{\bar{\Delta}}{\sigma_{\Delta}/\sqrt{n}},$$

TABLE I.A.10. Statistical Comparison of ANL and KM Analyses:
Preproduction and Process Variability. Lot No. 9819-20-01

	ANL				KM			
	Avg	σ	v	n	Avg	σ	v	n
<u>Composition</u>								
Pu, wt %	13.37	0.033	0.25%	12	13.34	0.016	0.12%	10
U, wt %	74.53	0.122	0.16%	12	74.87	0.133	0.18%	10
O, wt %	11.82	0.036	0.30%	10	11.84	0.0039	0.03%	10
Pu/U	0.179	0.006	-	10	0.178	0.005	-	10
O/M	2.001	0.005	-	10	2.000	0.001	-	10
²³⁹ Pu wt %	11.80	0.029	0.24%	10(4)	11.78	0.013	0.11%	10(4)
<u>Pu Isotopic, wt % ($f_{Pu} = {}^{239}Pu + {}^{241}Pu$)</u>								
²³⁸ Pu	0.05	-	-	4	0.05	-	-	4
²³⁹ Pu	86.61	0.034	0.04%	4	86.64	0.013	0.01%	4
²⁴⁰ Pu	11.50	0.041	0.36%	4	11.45	0.014	0.12%	4
²⁴¹ Pu	1.67	-	-	4	1.67	-	-	4
²⁴² Pu	0.19	-	-	4	0.19	-	-	4
Am	177 ppm			2				
<u>Impurities, ppm</u>								
Nonmetallic	230 (Est)			3(1)	103			3
Metallic	557			6	710			10
Rare earth	<4			4	<3			3
Refractory	<50			4	<36			3
Total	841				849			

TABLE I.A.11. Comparison of ANL and KM Analytical Precision
and Bias from Split Pellet Analysis. Lot No. 9819-20-01

Sample Number	ANL			Diff, d	KM			Diff, d	ANL-KM Δ
	Dup. 1	Dup. 2	Avg		Dup. 1	Dup. 2	Avg		
Plutonium, wt %									
F-01-2	13.41	13.37	13.39	0.04	13.40	13.36	13.38	0.04	0.01
F-01-3	13.34	13.40	13.38	0.06	13.36	13.32	13.34	0.04	0.04
F-01-35	13.42	13.38	13.40	0.04	13.33	13.33	13.33	0.00	0.07
F-01-36	13.35	13.42	13.38	0.07	13.36	13.34	13.35	0.02	0.03
F-01-37	13.40	13.40	13.40	0.00	13.41	13.30	13.36	0.11	0.04
				$\bar{d} = 0.052$				$\bar{d} = 0.052$	
				$\sigma_d = 0.027$				$\sigma_d = 0.041$	
$t_{0.05} = 2.78$									$\bar{\Delta} = 0.038$
$t(\text{calc}) = 3.86$									$\sigma_{\Delta} = 0.022$
Uranium, wt %									
F-01-2	74.24	74.71	74.48	0.47	74.74	74.46	74.60	0.28	-0.12
F-01-3	74.57	74.42	74.50	0.15	74.90	74.60	75.75	0.30	-0.25
F-01-35	74.74	74.61	74.68	0.13	75.19	74.85	75.02	0.34	-0.34
F-01-36	74.46	74.42	74.44	0.04	75.17	74.78	74.97	0.39	-0.53
F-01-37	74.52	74.43	74.48	0.09	74.78	74.74	74.76	0.04	-0.28
				$\bar{d} = 0.176$				$\bar{d} = 0.270$	
				$\sigma_d = 0.169$				$\sigma_d = 0.135$	
$t_{0.05} = 2.78$									$\bar{\Delta} = 0.300$
$t(\text{calc}) = 4.47$									$\sigma_{\Delta} = 0.150$

where $\bar{\Delta}$ represents the difference in the mean values, and n is the number of samples (five in this case). The calculated values of t are compared with the value of t at the 0.05 significance level. The calculated values shown in Table I.A.11 are larger than the "book" value, indicating statistically significant differences. The number of data is small, and an outlying value can have a rather profound effect on the result obtained. Split-pellet paired analyses are to be continued into production as a statistical-control device.

Duplicate analyses show the ANL precision to be somewhat better for plutonium analyses. Uranium precision is largely influenced in this limited test by one outlying value in the ANL group. Although the pooled result shows KM to have somewhat better precision, reproducibility has generally been better at ANL.

Nonmetallic impurities are shown as "estimated" by ANL in Table I.A.10. A rather large discrepancy exists between ANL and KM nitrogen determinations, whereas other nonmetallics, carbon, fluorine, and chlorine agree reasonably well. The ANL analysis for nitrogen by the total-gas-evolution method, yields results greater than 200 ppm. The KM microkjeldahl method showed nitrogen from 6 to 91 ppm. This anomaly has not yet been explained. Nitride phases are being studied at KM by X-ray diffraction and at ANL by microprobe analysis. Although the upper nitrogen level is specified at 200 ppm, at the 600°C service temperature of these elements, nitrogen is not a critical impurity.

(i) Granulating and Slugging. The slugging was done in an 0.600 die at 3.5-4.0 tons ram pressure. After granulation, particle size was sieved to 20 + 65 mesh. The pellets were pressed in 0.400 dies at 4.0 tons on the lower ram and 4.5 tons on the upper ram. Press dwell time was 1.5-2.0 sec. Green-pellet weight was 8.91-9.17 g, and length was 0.672 ± 0.005 in. The sintering furnace temperature was 1575-1600°C. The furnace atmosphere was nitrogen--6 vol % hydrogen, 10% water saturated.

Table I.A.12 indicates that the pellet manufacture can be within weight and dimensional control, although some sorting will be needed to assemble 10 pellet stacks within the specified core stack weight limits of 88.30-90.90 g and length limit of 5.682-5.742 in.

Pellet homogeneity is being studied at KM by autoradiography, X-ray diffraction, and metallography, and at ANL by microprobe analysis. All three methods indicate that the structure is essentially single-phase (solid solution) $(U,Pu)O_2$ with no significant areas of increased or decreased plutonium concentration. This situation was expected since the coprecipitation process does not begin with massive UO_2 or PuO_2 concentrations as does the mixed-oxide process.

TABLE I.A.12. Statistical Summary of Pellet Measurements^a

Dimension	Specified	Average \bar{x}	95.5% Confidence Limit		% Out of Specification
			2σ	$\bar{x} \pm 2\sigma$	
Weight, g	Report	8.92	0.22	8.70-9.14	
Max length, in.	Report	5.71	0.014	0.557-0.585	
Min length, in.	Report	5.69	0.014	0.555-0.583	
Δ length, in.	<0.002	0.002	0.002	0.000-0.004	2.69
Wt/max L, g/in.	15.30-16.30	15.64	0.22	15.42-15.86	0.4
<u>Diameter, in.</u>					
Top	<0.348	0.334	0.002	0.332-0.338	
Middle	<0.348	0.337	0.002	0.335-0.339	
Bottom	<0.348	0.338	0.002	0.336-0.340	
Δ diameter	<0.006	0.004	0.002	0.002-0.006	
Avg diameter	<0.348	0.337	0.002	0.335-0.339	

^aSample n = 1002 pellets randomly selected from Lot 9819-20-01.

(j) Preproduction Fuel Rods. Fifty fuel rods from the process variability pellet lot were made up and submitted to ANL for evaluation. The KM data from these were processed through the ANL ZPR Fuel Computer Program, which yielded the data shown by Table I.A.13.

TABLE I.A.13. Evaluation of Data from 50 KM Preproduction Fuel Rods

Dimension	Average \bar{x}	2σ Confidence Interval $\bar{x} \pm 2\sigma$	Specified or Target
Core length, in.	5.710	5.686-5.734	5.682-5.742
Rod length, in.	5.959	5.955-5.967	5.965-5.965
Gross weight, g	101.394	100.802-101.986	Report
Core weight, g	89.108	88.500-89.716	88.3-90.9
SS weight, g	12.286	12.110-12.462	Report
Linear density, g/in.	15.606	15.504-15.708	15.30-16.30 ^a
g oxygen	10.550	10.478-10.602	Report
g uranium	66.706	66.250-67.162	Report
g plutonium	11.887	11.805-11.969	Report
g ²³⁹ Pu + ²⁴¹ Pu	10.497	10.425-10.569	10.30-10.60
g ²⁴⁰ Pu	1.361	1.351-1.371	Report

^aMeasured on individual pellets.

ANL has completed visual and dimensional inspection, X-radiography, and gamma-scan spectrometry on the 50 fuel rods. All rods met inspection tolerances. Gamma-scan assay was in essential agreement with the total plutonium indicated by the KM report, although there were some anomalous readings from the individual KM data. These anomalies are being further studied. Several of the rods are being destructively evaluated. Internal pressure tests show these to be about one-third the 300 psig at 600°C limiting value. The evaluation of the cores are still underway. Sections of three pellets have been scanned on the microprobe analyzer. Preliminary reports of this work show no significant inhomogeneities.

Although the ANL reports were not complete for reporting purposes, sufficient information was available by July 22 to give KM a conditional release to start manufacture and shipment of the contracted for (U,Pu)O₂ fuel rods. The first production shipment, made on July 22, consisted of 468 fuel rods containing 41,825 kg of (U,Pu)O₂ and 5579 kg of plutonium.

(iv) Nonfissile Elements (6-30-70)

(a) Tantalum Plate Elements. Four sizes of plates were obtained from Wah Chang Corp., Albany, Oregon on P. O. 672766. Specification RF-C4a, Revision 2, provides for a matched set of plates ± 2 wt % of the average for each type. Wah Chang was able to achieve this by blanking the parts out of rolled sheet. The plates tended toward the high side of the thickness tolerance, and this coupled with the normally expected warp or bow has led to some difficulty in passing the drop-through gauge. About 75% pass by free fall, and about 25% require some "coaxing."

The order was supplemented to take advantage of a reduced price offered by Wah Chang for plates, which deviated slightly from the specifications or which were produced in excess. In all, 1914.2 kg (4220.1 lb) of tantalum plates were obtained in the quantities shown by Table I.A.14.

TABLE I.A.14. Sizes and Quantities of Tantalum Elements Ordered and Delivered

Nominal Size, in.	Number Ordered		Number Delivered		Total Delivered
	Original	Supp	Original	Supp	
1/16 x 2 x 2	3,500	90	3,500	90	3,590
1/16 x 2 x 3	13,800	743	13,644	743	14,387
1/16 x 2 x 1	5,000	325	5,000	325	5,325
1/16 x 1 x 1	800	650	800	650	1,450
Totals	23,100	1,808	22,944	1,808	24,752

(b) Molybdenum Foil Elements. Philips Elmet Corp., of Lewiston, Maine, supplied four sizes of elements on P. O. 682778 in accordance with Specification RF-C3d2 (ZPR). Thicknesses and lengths were chosen to provide a set of plates having weight ratios of 2:1 and 1.5:1. The average weight of any size plate was to be within $\pm 2\%$ of a target, and each plate making up a set was to be $\pm 2\%$ of the average. Senzimir mill rolling produced sheet of high-precision thickness from which the elements were sheared.

The pieces obtained were within target tolerances, weighed 191.7 kg (422.6 lb), and were distributed as shown in Table I.A.15.

TABLE I.A.15. Sizes and Quantities of
Molybdenum Elements Ordered and
Delivered under P. O. 682778

Nominal Size, in.	Number of Pieces	
	Ordered	Delivered
0.0089 x 2 x 6	3,000	3,033
0.0134 x 2 x 6	500	533
0.0089 x 2 x 12	3,000	3,039
0.0134 x 2 x 12	500	502
Totals	7,000	7,107

(c) Sodium and Sodium Carbonate Tunnel Elements. Instrument traverse or "tunnel" elements are provided with a hole near one end of the element, which traverses the thickness dimension. Fuel tunnel elements have been provided and a number of sodium and sodium carbonate units similar in construction were required to complement these.

The elements were fabricated in ANL Central Shops. Materials used were obtained from previous procurements for other types of elements. D. K. Aerospace supplied the stainless steel jackets, sodium carbonate wafers were manufactured by NUMEC, and the sodium supplied by U.S.I. was that used for calandria filling. The types produced are shown in Table I.A.16.

TABLE I.A.16. Sizes and Quantities of Tunnel
Plates Ordered and Delivered

Nominal Size, in.	Filling	Number	
		Ordered	Delivered to Idaho
1/3 x 2 x 4	Sodium	100	125
1/2 x 2 x 4	Sodium	100	114
1/4 x 2 x 4	Sodium carbonate	50	56
1/2 x 2 x 4	Sodium	50	56

(d) Iron Oxide Plates. The latest acquisition of Fe_2O_3 plates was limited to one size, 1/8 x 2 x 3 in. All of the 15,000 ordered from D. M. Steward Manufacturing Company of Chattanooga, Tennessee, on P. O. 674486 have been received, but inspection is not yet complete. The structure and appearance of these plates are somewhat different from material previously supplied. This difference is attributed to different forming techniques, i.e., hot pressing versus cold forming and sintering. The characteristics of the plates such as density and purity will match those previously supplied, however.

B. Component Development

1. Instrumentation and Control

a. Instrumentation Development for Instrumented Subassembly

(i) Instrumented-subassembly Flowmeters (G. A. Forster)

Last Reported: ANL-7688, p. 65 (April-May 1970).

(a) Procurement of Mark-III (Sodium-calibratable) Flowmeters. Of the two purchase orders issued for procurement of these flowmeters, one vendor is close to schedule (in the final assembly stage) and plans to deliver about the end of July. The other vendor is proceeding with fabrication of parts, but still has problems with complete documentation to meet our quality-assurance requirements. If these problems are resolved, the vendor will deliver on schedule.

(b) Modification of Calibration Loop for Mark-III Flowmeters. The sodium-level probes have been repaired; however, two sets of replacement probes were fabricated before satisfactory operation was achieved. The first set of probes failed in processing when the sealant used to bond the Nichrome heater wire into the ceramic insulators expanded and cracked all of the insulators. The second set employs only an outer seal.

The Mark-II-002 flowmeter is installed in the loop, and testing is scheduled for completion by the middle of August.

(ii) Instrumented-subassembly Coolant Thermocouples (A. E. Knox)

(a) Tests of Prototype Coolant and Spacer-wire Thermocouples

Last Reported: ANL-7669, p. 41 (Feb 1969).

Eleven of the 14 coolant-type (Chromel/Alumel) thermocouples in the Test XX01 EBR-II Instrumented Subassembly developed no gross defect during the irradiation period.

Time-domain reflectometer measurements of coolant thermocouples OTC 6 and PSTC 16 (see Progress Report for June, ANL-7705, p. 39) indicate that the failures occurred in the region of the drywell where the sheathed and flexible leads are joined.

Of the four spacer-wire thermocouples (SWTC), thermocouple SWTC 7 developed an intermittent failure within the subassembly system. Location and mode of the failure varied with time; hence a definite diagnosis could not be made. Current evidence indicates that of all the coolant thermocouples, only SWTC 7 may have failed in its high-temperature sensing region.

Coolant thermocouples in Test XX02 EBR-II Instrumented Subassembly also employ the same sheathed-to-flexible lead joint as the XX01 Subassembly. To date, one outlet thermocouple in XX02 (OTC 15A), has failed due to open-circuited leads in the lead joint region of the drywell.

The XX01 test and out-of-reactor tests (see Progress Report for February 1970, ANL-7669, p. 41) show that the high-quality coolant thermocouples employed in EBR-II instrumented subassemblies are reliable; they have also demonstrated the reliability of a relatively new thermocouple construction, i.e., a dual-diameter (0.062- to 0.040-in.-OD) thermocouple that is spiraled and replaces a 0.040-in.-OD EBR-II fuel-pin spacer wire. However, the connection between the thermocouples and the flexible lead wires has not been as reliable as desired. A modified lead joint connection has been developed and will be used on future subassemblies.

The extent of possible radiation-induced decalibrations in the coolant thermocouples will be evaluated after postirradiation examinations are complete.

b. FFTF Instrumentation (R. A. Jaross)

(i) In-core Flowsensor (T. P. Mulcahey)

(a) Permanent Magnet Probe-type Flowsensors (F. Verber)

Last Reported: ANL-7705, p. 39 (June 1970).

Bids have been received from three suppliers of Type A-4 $\frac{1}{4}$ in-core, permanent-magnet, probe-type sodium flowsensors. The bids are being reviewed and evaluated.

Final assembly of an ANL-fabricated Type A-4 $\frac{1}{4}$ flow-sensor for testing in the Core Component Test Loop (CCTL) has been completed. This includes attachment of the flowsensor to a probe shaft extension and welding of four coolant thermocouples to the shaft immediately behind the flowsensor. The entire assembly is similar to the configuration planned for FFTF.

Figure I.B.1 shows the principal components of the assembly before insertion into the CCTL test vessel. The sodium seal prevents leakage up the annulus between the probe-shaft guide and the probe-shaft extension, and also between the probe-shaft guide and an outer guide tube (not shown) attached to the test vessel.

In response to an inquiry on permanent magnets (see Progress Report for April-May 1970, ANL-7688, p. 68), the supplier advises that: (1) we have been using the highest grade of Cast Alnico VIII material; (2) the calibration requirement that the operating points of the magnets (in lots of 50 and 100) will not differ by more than $\pm 5\%$, $\pm 2\frac{1}{2}\%$, or $\pm 1\%$, might be feasible but very expensive; and (3) his company would attempt the calibration only on a "best-effort" basis and not on the basis of a guarantee.

(b) Eddy-current Probe-type Flowsensor (J. Brewer)

Last Reported: ANL-7705, p. 40 (June 1970).

Flowtesting of E-C Probe No. 10 in the CAMEL has been limited in favor of completing the simulated fission-gas-injection-detection tests with the Type A-4, permanent-magnet, probe-type flow-sensor in this facility.

The flowtests that were performed on Probe No. 10 related signal amplitude and excitation frequency at sodium velocities of 1.05, 2.1, 6.3, and 10.5 ft/sec, and temperatures of 300, 400, 500, and 600°F. Eventually, the tests will be extended to 1200°F. These tests provide calibration and linearity information that will aid in selecting the optimum excitation frequency for a given temperature range.

Figure I.B.2 shows the E-C probe signal output at the above-mentioned sodium velocities and temperatures, using a drive current of 500 mA at 1000 Hz. A frequency of 1000 Hz was selected because, at this time, it appears to be a near optimum value for the 300-1200°F range.

With regard to reproducibility, a comparison of the data at 600°F with that taken two weeks earlier at the same temperature shows no deviation in probe sensitivity. In the ensuing period, the CAMEL was operated intermittently (7 hr/day, 5 days/week) at sodium velocities up to 10.5 ft/sec and temperatures from 350 to 600°F. Most of the operating time was devoted to gas-injection tests.

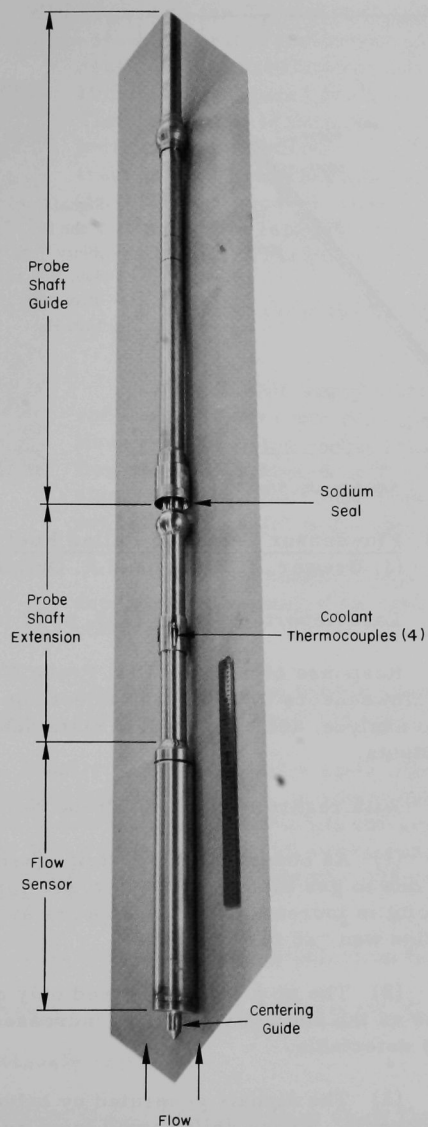


Fig. I.B.1. Test Configuration of Type A-4 $\frac{1}{4}$
Permanent-magnet Flowsensor

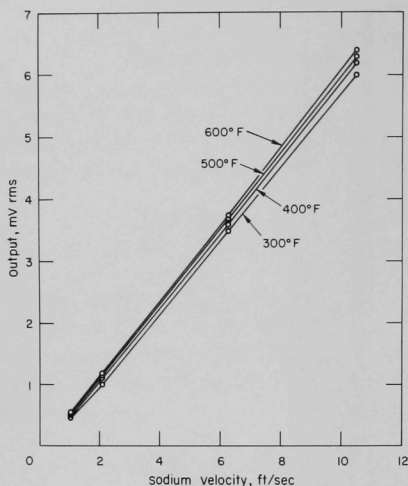


Fig. I.B.2
Signal Output of Eddy-current
Probe No. 10 vs Sodium Ve-
locity in the CAMEL at 300,
400, 500, and 600°F. Probe
drive current = 500 mA at
1000 Hz.

(c) Flowsensor Tests for Failed Fuel Monitoring
(J. Brewer, J. Bobis, and A. Quigley)

Last Reported: ANL-7705, p. 42 (June 1970).

Response of both the E-C Probe No. 10 and Type A-4 permanent-magnet flowsensors to argon-gas injections into the CAMEL has been difficult to analyze, and only general statements can be made regarding signal outputs.

With regard to the E-C Probe No. 10:

(1) As observed on the strip-chart recorder, the dc signal deviation due to gas injected at 100 cc/sec for 6 sec decreases as the sodium velocity is increased, and disappears at ~ 9.5 ft/sec. At 2 ft/sec, the deviation was ~ 25 mV positive.

(2) The ac signal, observed only on an oscilloscope, appears to decrease as the sodium velocity is increased. At 10.5 ft/sec, a bubble signal was detectable.

(3) The signals generated by bubbles have both phase and amplitude components. Phase shift varied from as much as 90° at 2 ft/sec to several degrees at 10.5 ft/sec. At 2 ft/sec, an amplitude signal of ~ 70 mV peak-to-peak was generated.

With regard to the Type A-4 flowsensor: signals generated by gas injections of various rates and durations were observed on an oscilloscope at sodium velocities between 2.1 and 10.5 ft/sec. Figure I.B.3 shows a typical display. The upper trace is the noise signal, without gas injection, at a sodium velocity of 7.4 ft/sec. The lower trace is the signal 8 sec after the start of a gas injection of 100 cc/sec that lasted 6 sec. The peak-to-peak amplitude of the large (60-Hz) noise signal is $\sim 50 \mu\text{V}$. The dc output of the flowsensor is about 4 mV.

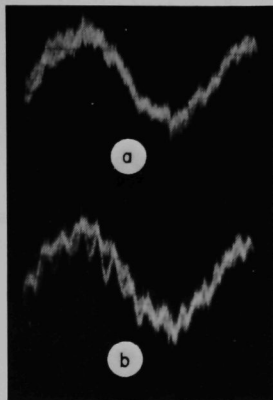


Fig. I.B.3

Noise Response of Type A-4 Permanent-magnet Probe-type Flowsensor (a) without Gas Injection and (b) with Gas Injection

General conclusions from these tests are as follows:

(1) Bubble signals are observed at most sodium flow rates and gas-injection conditions. However, the noise signal with no bubbles at high flow rates is comparable in amplitude to bubble signals at low flow rates; therefore the latter cannot be made useful under the present conditions.

(2) The bubble signal is ~ 600 Hz and independent of sodium flow rate and bubble-injection conditions.

(3) The flowsensor ac bubble signals are so small they would be difficult to separate from the noise signals.

Finally, throughout these tests, the gas injections have had a prolonged effect on both flowsensors, in some cases lasting many minutes. This effect is attributed to retention in the horizontal test chamber of pockets of gas that slowly release and sweep past the flowsensors. The gas is not recirculated in the loop, since gas injected downstream of the flowsensors was not detected.

This concludes the gas-injection tests in the CAMEL.

c. Plant Dynamics and Control Analysis (W. C. Lipinski)

Not previously reported.

The objective of this program is to study the control systems proposed for the large LMFBR plant designs in conjunction with the 1000-MWe LMFBR plant-design studies. This effort will focus on the adequacy of the control systems proposed to meet the overall control and performance goals of the large LMFBR's and will identify (1) current and potential LMFBR control problems, (2) systems where further control-system

optimization would improve the economic and operational aspects of an LMFBF, and (3) development required in LMFBF reactor and plant control.

Initially, most of the effort in this program will be in component and system model development. The 1000-MWe design studies will be reviewed, and the work scopes for the forthcoming 1000-MWe LMFBF dynamic simulation studies will be evaluated. A simplified model will be developed which can be programmed on the existing ANL hybrid computer.

The various conceptual plant designs and overall plant control schemes in the Task II Reports of the 1000-MWe LMFBF Follow-on Studies* have been reviewed. Also, an extensive review is being made of publications on modeling and simulation of entire nuclear power plants and plant components. Based on these reviews, the major plant system components and the basic problems for the initial modeling of these components will be identified. The models will be used in simulation of mild transients which would be grouped as resulting from normal or upset conditions according to ASME classifications, with provision for future extension to more severe transients resulting from emergency or faulted conditions. General descriptions of the component models to be simulated are given below. These models are subject to necessary revision which may be indicated during the actual simulation.

(i) Reactor. For the mild transients to be considered, the single-node or point-model description of neutron kinetics with six delayed-neutron groups is adequate. The dynamics of the coolant and fuel temperature in the core is assumed to be adequately represented by a single-channel model using four axial nodes. Average temperatures in the radial direction in the channel are used, and changes in cladding and structural-material energy storage are ignored. The dynamics of the temperature of the coolant which passes through the reflector, blanket, and bypass channels are modeled by an additional representative channel with a single axial node. Feedback reactivity of the core is a linear function of the temperatures in each axial node. Single-node models are also used in describing mixing and transport lags in both the inlet and outlet plenums.

(ii) Intermediate Heat Exchanger (IHX). The dynamics of the secondary and primary sodium temperature in the IHX is also based on the dynamics of a single representative channel. Four nodes in the channel will be used, and the changes in the structural heat storage are not to be included.

*1000 MWe LMFBF Follow-on Study, Conceptual System Design Descriptions, AI-AEC-12791, Vol. 2 (Feb 1968); 1000 MWe LMFBF Follow-on Study, Conceptual System Design Descriptions, BAW-1328, Vol. 3 (Feb 1969); 1000 MWe LMFBF Follow-on Study, Conceptual Plant Design, System Descriptions, and Costs for a 1000 MWe Sodium-Cooled Fast Reactor, GEAP-5678 (Dec 1968); 1000 MWe LMFBF Follow-on Study, Conceptual Design, WARD-2000-97 (April 1969).

(iii) Reheater. The model of the component for reheating the steam before it enters the intermediate- and low-pressure turbines is similar to that of the IHX.

(iv) Steam Generator. A once-through steam generator, which includes the vaporizer and superheater in a single unit, has been selected as the steam source for the turbines. Simulation of this component will comprise a major effort, since it is potentially the most sensitive to instabilities and is difficult to model. The difficulty is due to the change of phase in the tube side and the change of heat-transfer coefficients which correspond to the transition to different flow regimes. Recent publications have demonstrated the advantages of using continuous-space-discrete-time (CSDT) simulations for counterflow heat exchangers.* However, this approach complicates the total-plant simulation, since a discrete-space-continuous-time (DSCT) approach is used in simulation of the remaining plant components. A compromise approach which appears to have merit is to use a DSCT simulation with parameters based on spatial temperature profiles computed using the continuous-space model. The parameters in the continuous-time simulation would be updated at appropriate intervals based on new computations of spatial temperature profiles. The quasi-linearization procedure for solving nonlinear multipoint boundary-value problems may be of use in obtaining the spatial temperature profiles.**

An additional possibility is the use of a DSCT simulation in which the zone lengths are continuously varied to coincide with the varying lengths of the different flow regimes.[†] However, this approach also requires further development to determine its value.

Although the above discussion covers the simulation of the steam generator, the same techniques can be used for simulations of thermohydraulic processes in the IHX or reactor core.

Before completion of an advanced steam-generator model which includes all salient features, a simplified model of this component will be developed for use in an overall plant simulation.

*Brux, J. F. L. M., and Tessier, J. H., "Serial Solution of Nonlinear Partial Differential Equations of a Counterflow Heat Exchanger Using S/360-CSMP," Proc. 1970 Summer Computer Simulation Council, pp. 360-371 (June 1970); Carling, L. N., Hybrid Computer Solution of Heat Exchanger Partial Differential Equations, Annales de l'Association internationale pour le Calcul Analogique 1, 6, pp. 6-18 (Jan 1968); Chamboredon, C., Hery, M., and Marion, B., Study of a Fast-Reactor Nuclear Power Plant on a Hybrid Computer, ANL-TRANS-771. Translated from Proc. 5th Inter. Analogue Computation Meetings, pp. 1065-1070 (1967).

**Bellman, R., and Kalaba, R., Quasilinearization and Nonlinear Boundary-Value Problems, American Elsevier Publ. Co., Inc., N.Y. (1965); Habegger, L., and Hsu, C., The Use of Quasilinearization for the Solution of Nonlinear Space-Dependent Reactor Equations, Trans. Amer. Nucl. Soc. 12, p. 830.

[†]Proctor, W. G., and Wilson, B., "The Simulation of a Once Through Sub-Critical Boiler," Proc. 4th Inter. Analogue Computation Meeting, pp. 421-436 (1964).

(v) Coolant Pipelines. The transport of coolant between plant components is assumed to introduce pure time delay. Such delays are simulated by storing sampled values in the digital computer and are re-introduced one transport-time later.

(vi) Turbine, Generator, Condenser, and Feedwater Heaters. These components will not be included in the initial plant simulation, but will be included in the advanced plant simulation to provide a complete closed loop.

(vii) Control Systems. The overall plant simulation will include the following control actuators: a control rod for reactor power control; a primary pump for reactor-coolant flow control; an intermediate pump for control of intermediate coolant flow; feedwater pump, feedwater pump turbine, and control valves for control of feedwater flow; intermediate coolant bypass valve to control intermediate coolant flow to the steam generator; a reheater control valve to control intermediate coolant flow to the reheater; and a main steam-throttle valve and steam-bypass valve to control steam flow from the steam generator to the high-pressure turbine. Various modes of operation for the above systems and their associated controllers will be considered to determine overall control-system performance and to identify and resolve problems.

(viii) Multiple Loops. The advanced simulation will include two IHX and steam-generation loops to determine their interaction during transients.

2. Fuel Handling, Vessels, and Internals

a. Core Component Test Loop (CCTL) (R. A. Jaross)

Last Reported: ANL-7705, pp. 45-46 (June 1970).

(i) Operation of Loop to Test Second FFTF Subassembly. As of June 18, 1970, five samplings of CCTL sodium have been taken and analyzed for oxygen and carbon content. The results are summarized in Table I.B.1.

TABLE I.B.1. Oxygen and Carbon Content in CCTL Sodium

Sample No.	Date Taken	Temp, °F	Oxygen, ^a ppm	Carbon, ^a ppm
CCTL 1	5-20-70	400	4; 5	18
CCTL 2	5-26-70	800	4; < 2	58; 28; 52 ^b
CCTL 3	6-3-70	800	5	13
CCTL 4	6-10-70	800	< 2	6
CCTL 5	6-18-70	1050	2	7

^aAllowable limits: O₂ = 10 ppm; C = 20 ppm.

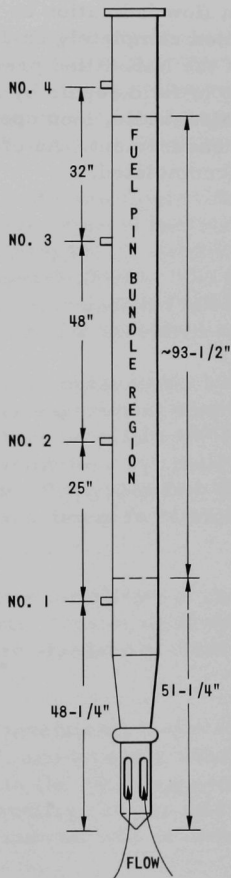
^bHigh content attributed to deficiencies in analytical equipment and techniques.

Table I.B.2 lists the results of a second flow rate-pressure relationship test of the FFTF Mark-II fuel assembly at 800°F. This test was started after a check analysis of system sodium (CCTL 3) indicated low carbon content; it was interrupted on June 5 to repair a small sodium leak and to clean out vapor traps in the inert-gas system, and resumed on June 12.

TABLE I.B.2. Sodium Flow Rate Pressure Relationship for
FFTF Mark-II Fuel Assembly at 800°F

Sodium Flow Rate, gpm	Pressure, psig ^a			
	Tap No. 1	Tap No. 2	Tap No. 3	Tap No. 4
<u>June 5, 1970</u>				
132	2.9	3.0	1.0	0.4
194	7.2	6.3	2.2	0.6
254	12.4	10.3	3.7	2.1
318	19.2	15.3	5.5	2.7
380	27.4	21.0	7.6	2.5
429	36.8	27.8	10.2	3.5
496	47.4	35.8	13.4	4.8
520	51.2	38.3	14.4	5.1
427	37.4	27.8	10.1	3.6
405	32.6	24.0	8.8	3.0
343	23.9	17.8	6.5	2.1
280	16.6	12.5	5.4	2.4
219	10.6	7.8	2.7	0.7
155	5.6	4.3	2.5	0.5
85	2.3	1.6	0.5	0.2
<u>June 12, 1970</u>				
465	41.5	31.1	11.5	4.2
501	47.1	34.7	12.9	4.7
516	49.7	36.2	13.9	5.0
520	49.8	36.7	13.7	5.0
502	46.7	34.2	12.9	4.7
456	41.7	30.6	11.3	4.1
423	36.2	27.0	10.0	3.5
396	31.8	23.4	8.7	3.0
371	27.1	20.1	7.5	2.5
346	22.9	17.7	6.3	2.1
286	16.5	12.1	4.5	1.4
223	9.9	7.9	2.9	0.9
164	6.1	4.1	1.6	0.4

^aCorrected to 0 psig at no flow.



On June 13, following confirmation of low carbon and oxygen levels from sodium sample CCTL 4, loop temperature was increased gradually, reaching 1050°F on June 15. Sodium flow rate was increased to 525 gpm on June 16. Operations at these conditions continued until June 23, pending analysis of sodium sample CCTL 5. On June 24, the loop temperature was increased to 1100°F, signifying the start of the 9000-hr flow test of the Mark-II fuel assembly.

With one exception, system operation has been satisfactory: Sodium flow indication by the loop flowtube became increasingly erratic, and failed completely on July 7. The failure appears related to the oil side of the NaK-filled pressure-transducer system. Diagnosis of the possibility of field repair by ANL staff and the transducer vendor is under way. Meanwhile, loop operation is continuing, using the EM flowtube for flow measurement. As of July 20, 613 hr at 1100°F and 525 gpm have been accumulated.

C. EBR-II--Research and Development

1. New Subassemblies and Experimental Support (E. Hutter)

a. Experimental Irradiation Subassemblies

(i) Mark-M1 Irradiation Subassembly (O. Seim and W. Ware)

Not previously reported.

The Mark-M1 subassembly was designed for irradiating large samples of structural or other nonfissionable materials. The materials are packaged in a specimen cage, not longer than 20 in., that will fit inside the 2.210-in.-ID hexagonal tube. The specimen cage is designed by the experimenter, with guidance and final approval by the EBR-II Project.

The design objective for the Mark M1 was to provide a simple and economical vehicle to be used for a wide range of material-irradiation experiments. In keeping with this philosophy, the hardware items are mainly standard parts used in other subassemblies. The only new hardware item, outside of the specimen cage, is a modified lower shield that has a fastening device at its top to secure the specimen cage.

The rate of coolant flow through the subassembly will be set by balancing the cooling needs of the particular experiment with the requirement that the subassembly outlet temperature be within 100°F of the outlet temperatures of the surrounding subassemblies. Normally, an orifice plate will be needed to reduce coolant flow. Preirradiation flow-tests of the subassembly will be made for each experiment to establish an orifice size for that particular experiment.

Figure I.C.1 illustrates the relative simplicity of the Mark-M1 design. The outer structural components, consisting of the top end fixture, hexagonal tube, and lower adapter, are standard to most subassemblies.

The lower shield is a modified conventional lower shield. A three-plate orifice is welded into its lower end, and lugs are attached to its upper end. The specimen cage is fastened to the lugs by a removable pin so that the cage can be removed by remote handling devices after irradiation. This pin is trapped in place when the hexagonal tube is lowered over the shield pieces and specimen cage.

The upper shield is identical to the upper shield in the Mark-L61 subassembly and has provisions for installing two temperature sensors.

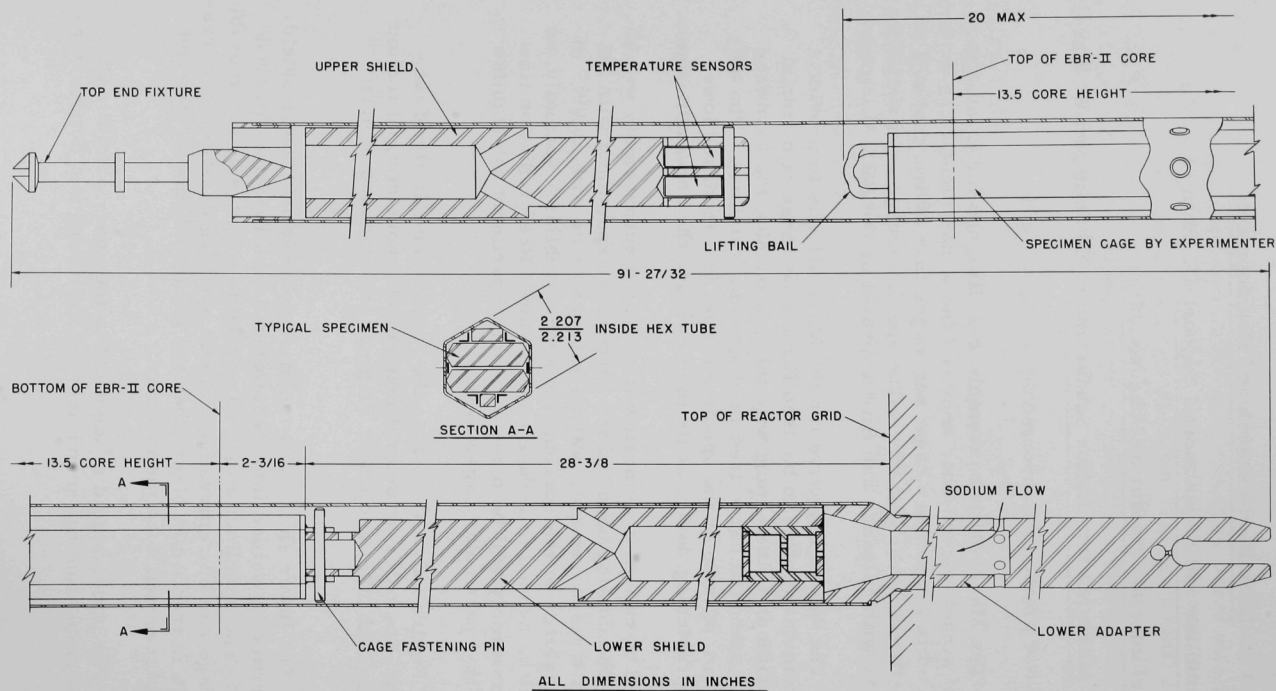


Fig. I.C.1. EBR-II Mark-M1 Irradiation Subassembly

The bottom edge of the cage will be $2\frac{3}{16}$ in. below the lower edge of the reactor core. The cage will be designed and fabricated by the experimenter to suit the type of materials he intends to test. The mass of the test materials should be as great as possible so that a large flow of coolant and, therefore, large orifice holes may be used. Small orifice holes restrict draining of trapped sodium while the subassembly is being removed from the reactor and have a greater chance of plugging.

2. Instrumented Subassemblies (E. Hutter and A. Smaardyk)

a. Instrumented-subassembly Test 4 (XX03)

(i) Flux Monitor for Subassembly XX03 (J. Poloncsik)

Not previously reported.

The method used for installing the flux monitor in the test-2 (XX01) instrumented subassembly (see Progress Report for November 1969, ANL-7640, p. 40) has been modified for instrumented subassembly XX03.

With the previous method, the irradiated flux monitor and its lead were withdrawn from the flux-monitor tube before the sensor leads from the subassembly were cut when preparing to remove the subassembly from the reactor. This was done to ensure that the monitor lead above the cut would not drop out of the upper severed portion of the flux-monitor tube after the lead-cutting operation. With the new method, the highly radioactive monitor and lead do not have to be removed from the flux-monitor tube before the lead-cutting operation. The monitor lead is cut with the other sensor leads, with assurance that no part of the severed lead will drop from the tube.

Figure I.C.2 shows how the two flux monitors planned for XX03 will be installed. The flux-monitor tube, formerly one 0.187-in.-OD tube, now is made in two tubular sections. The upper tube (0.187-in. ID) fits over the top portion of the lower tube. A sleeve brazed to the monitor leads fits into the large tube and supports the upper portions of the severed leads by resting on the upper end of the small tube (the "flux monitor support shoulder" shown in the figure).

A mockup of this method of supporting the flux-monitor leads has been fabricated and appears to be satisfactory. The bellows arrangement to allow differential expansion between the flux monitor and the extension tube is retained. However, the bellows assembly has been made more compact to gain sufficient space for incorporating the creep-test micropositioning motors in the terminal box.

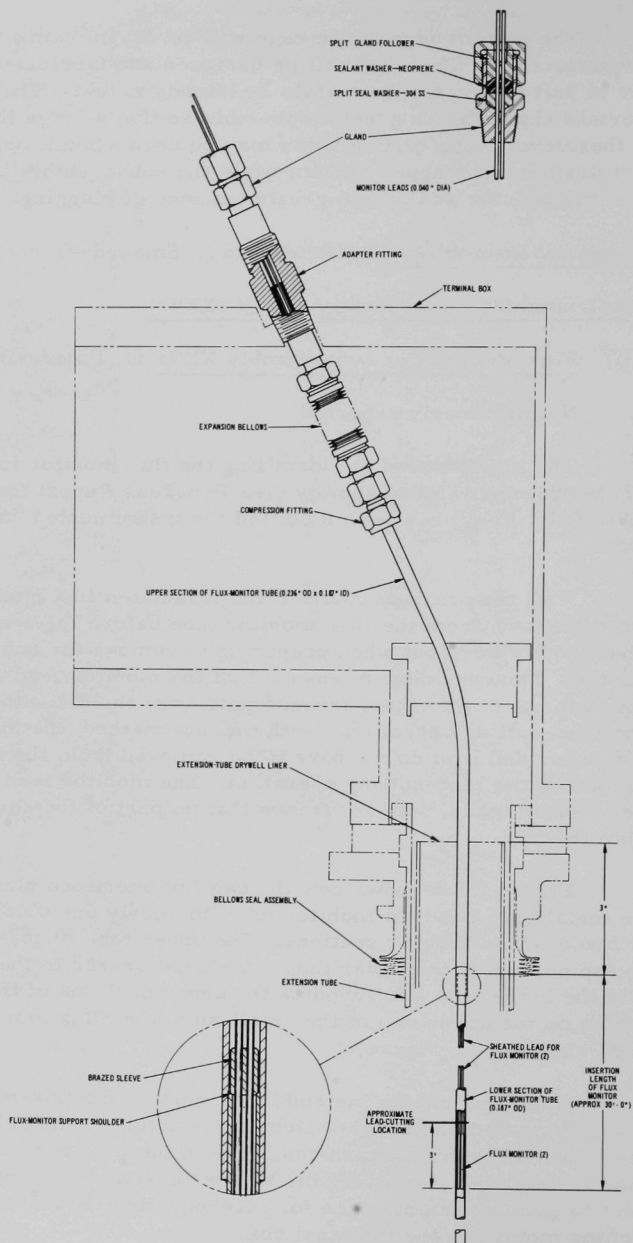


Fig. I.C.2. Flux-monitor Installation for Instrumented Subassembly XX03

Since the flux monitors in XX03 are sealed within the flux-monitor tube by a gland while the subassembly is in the reactor, the isolation valve for the flux-monitor tube (see ANL-7640) has been eliminated for XX03. The valve was originally planned to provide isolation while the flux monitor is being retracted and reinserted.

3. Coolant Chemistry (D. W. Cissel)

- a. Monitoring of Sodium-coolant Quality (W. H. Olson, C. C. Miles, T. P. Ramachandran, E. R. Ebersole, and G. O. Haroldsen)

Last Reported: ANL-7688, pp. 85-94 (April-May 1970).

(i) Radionuclides in Sodium. Table I.C.1 lists results of analyses for ^{137}Cs and ^{131}I in primary sodium. Sodium-22 activity is $\sim 4.5 \times 10^{-2} \mu\text{Ci/g}$.

TABLE I.C.1. ^{137}Cs and ^{131}I in Primary Sodium^a

Sample Date	Sample Size, g	Sample Flow, gpm	Sample Temp, °F	^{137}Cs , $\mu\text{Ci/g}$	^{131}I , $\mu\text{Ci/g}$
5/13/70	11.3	0.5	570	1.3	2.0
5/22/70	12.6	0.4	570	-	2.7
5/27/70	11.0	0.4	580	-	2.0
6/1/70	12.6	0.3	590	-	1.6
6/5/70	12.4	0.4	590	1.1	2.0
6/10/70	13.1	0.4	580	1.2	2.1
6/19/70	13.1	0.4	590	1.2	2.2
6/24/70	12.9	0.4	590	1.0	2.5
6/29/70	13.5	0.4	590	-	2.1

^aFlush time for all samples was 15 min.

Table I.C.2 lists total activities of activation products in 86,000 gal of primary sodium. Determinations were made on the vacuum-distillation residue from 50-g samples taken from the primary system on the dates listed.

TABLE I.C.2. Activation Products in 86,000 gal of Primary Sodium
(Total activities in Ci)

Sample Date	^{117m}Sn	^{113m}In	^{125}Sb	^{110m}Ag	^{54}Mn
1/6/70	1.3	1.4	0.19	0.16	0.9×10^{-4}
2/5/70	1.3	1.6	0.21	0.13	1.9×10^{-4}
3/19/70	1.7	1.8	0.08	0.15	0.8×10^{-4}

(ii) Trace Metals in Sodium. Table I.C.3 lists results of analyses for trace-metal impurities in primary and secondary sodium. Metal concentrations were measured by atomic-absorption spectrophotometry.

TABLE I.C.3. Trace Metals in Sodium, ppm

Sample Date	Sample Size, g	Sample Flow, gpm	Flush Time, min	Sample Temp, °F	Ag	Al	Bi	Ca	Co	Cr	Cu	Fe	In	Mg	Mn	Mo	Ni	Pb	Sn
<u>Primary Sodium</u>																			
5/18/70 ^a	56.1	0.5	15	580	0.06	<0.6	2.0	<0.02	<0.02	0.1	<0.02	0.15	<0.06	<0.005	<0.005	<0.07	<0.04	9.4	21.6
6/16/70 ^a	56.0	0.6	15	575	0.04	<0.6	1.6	<0.02	<0.02	<0.02	<0.02	0.1	<0.06	<0.005	<0.005	<0.07	<0.04	7.5	20.6
<u>Secondary Sodium</u>																			
5/26/70 ^b	64	0.5	15	435	<0.01	<0.6	<0.1	<0.02	<0.02	0.15	<0.02	0.7	<0.06	<0.005	0.02	<0.07	0.1	0.1	<0.5
6/23/70 ^c	124	0.8	18	520	0.01	<0.3	<0.05	<0.01	<0.01	0.035	0.05	0.2	<0.03	0.025	0.015	<0.04	0.05	0.7	<0.3

^aSampled in titanium; sodium separated by laboratory distillation.

^bSampled in tantalum; sodium separated by laboratory distillation.

^cSampled in titanium; sodium separated by in-line distillation.

(iii) Oxygen in Sodium. Table I.C.4 lists results of analyses for oxygen in sodium by the mercury amalgamation method. Samples of ~15 g were taken in stainless steel vessels and extrusion aliquoted for analyses.

TABLE I.C.4. Oxygen in Sodium

Sample Date	Sample Flow, gpm	Sample Temp, °F	Number of Aliquots ^a	Average Concentration, ppm	Oxygen Equivalent of Plugging Run, ppm
<u>Primary Sodium</u>					
5/18/70	0.35	560	4	1.7 ± 0.8	<0.5
6/19/70	0.40	570	2	1.0 ± 0.3	<0.5
<u>Secondary Sodium</u>					
5/7/70	0.85	420	3	2.9 ± 1.1	<0.5
6/10/70	0.75	460	3	1.0 ± 0.1	<0.5

^aAliquot size was ~1 g.

(iv) Carbon in Sodium. Table I.C.5 lists results of analyses for carbon by the oxyacidic flux method. Samples of ~15 g were taken in stainless steel vessels and extrusion aliquoted for analysis.

TABLE I.C.5. Carbon in Sodium^a

Sample Date	Sample Flow, gpm	Sample Temp, °F	Number of Aliquots ^b	Average Concentration, ppm
<u>Primary Sodium</u>				
5/18/70	0.35	560	3	1.0 ± 0.2
6/19/70	0.4	570	3	0.7 ± 0.17
<u>Secondary Sodium</u>				
5/7/70	0.85	420	3	1.2 ± 0.3
6/10/70	0.75	460	3	0.6 ± 0.15

^aFlush time for all samples was 15 min.

^bAliquot size was ~1 g.

Most of the carbon-recovery tests on the oxyacidic flux method have been run with carbon standards about 100 µg in weight, rather than in the range of 0-10 µg, because of the difficulty in accurately measuring out the small quantities of the standards. Some criticism of this approach has been voiced because

carbon values in sodium samples normally are below 10 µg. Recovery tests have now been made in the range of 0-5 µg by adding carbon as

potassium acid phthalate to sodium samples whose carbon content was established by prior analysis. Table I.C.6 gives the results of these recovery tests.

TABLE I.C.6. Results of Carbon-recovery Tests

Run No.	Carbon Added, μg	Carbon in Na, μg	Total Found, μg	Blank, μg	Net Recovery, μg	Percent Recovery
1	3.3	1.0	4.6	0.4	3.2	97
2	3.3	1.0	4.5	0.4	3.1	93

(v) Hydrogen in Sodium. A sample of secondary sodium taken March 10, 1970 was analyzed at Pacific Northwest Laboratory by the amalgam-reflux method. Results of two determinations were:

0.21 and 0.29 ppm H as hydroxide, and

0.05 and 0.07 ppm H as hydride plus free hydrogen.

(vi) Nitrogen in Sodium. Preliminary work on the determination of nitride nitrogen in sodium has been started after some modifications of the Kjeldahl distillation were made. About 10 g of sodium was sampled in quartz beakers and dissolved in a mixture of 30 vol % water and alcohol. The liberated ammonia was collected by purging with argon gas through 5% boric acid. The distillate was kept hot to keep its volume small by continuous evaporation. Table I.C.7 lists the results obtained on primary sodium.

TABLE I.C.7. Nitride Nitrogen in Primary Sodium

Sample Date	Sample Size, g	Nitride N, ppm
3/21/70	11.5	0.18
3/22/70	11.5	0.15
5/1/70	12.0	0.22
5/25/70	6.6	0.17

(vii) Silicon in Sodium. A method for determining silicon in sodium has been investigated. It involves vacuum distillation of the sodium, dissolution of the silicon in the distillation residue with dilute hydrofluoric acid, and spectrophotometric determination of silicon as the reduced heteropoly molybdosilicic acid. The color-development method may be applied directly to sodium residues dissolved from tantalum cups, but an additional separation step for removing titanium is required for samples dissolved from titanium cups. Titanium dissolves and interferes in the subsequent color development.

Recovery tests run on silicon added as sodium silicate to 10 g of sodium indicate that silicon remained quantitatively in the distillation residue.

Secondary sodium sampled in a tantalum cup was distilled, and the residue was analyzed for silicon by a colorimetric procedure. About 3 ppm of silicon was found in the sodium.

(viii) In-line Vacuum-distillation Sodium Sampler. For weight determinations, three samples were removed from the system without distilling. The samples weighed 124.0, 123.2, and 123.6 g. The sampling temperature was $\sim 550^{\circ}\text{F}$.

Two samples taken earlier at 350°F weighed 123.2 and 124.1 g. Reproducibility of sample weight appears to be better than 1%.

(ix) Hydrogen and Nitrogen in Cover Gas. Table I.C.8 summarizes the concentrations of hydrogen and nitrogen in the primary and secondary argon cover-gas systems. Measurements were made with on-stream gas chromatographs.

TABLE I.C.8. Hydrogen and Nitrogen in Argon
Cover-gas Systems, ppm

	Primary			Secondary		
	High	Low	Average	High	Low	Average
<u>June</u>						
H ₂	144	4	17	4	4	4
N ₂	6,000	2,100	3,600	200	100	150
<u>July</u>						
H ₂	128	4	11	4	4	4
N ₂	9,000	2,300	3,600	200	100	150

4. Experimental Irradiation and Testing (R. Neidner)

a. Experimental Irradiations

Last Reported: ANL-7705, pp. 66-69 (June 1970).

Table I.C.9 shows the status of the experimental subassemblies in EBR-II on July 15, 1970.

TABLE I.C.9. Status of EBR-II Experimental Irradiations as of July 15, 1970 (Run 44A Completed)

Subassembly No. and (Position)	Date Charged	Capsule Content and (Number of Capsules)		Exper- imenter	Accumulated Exposure, MWd	Estimated Goal Exposure, MWd	Burnup ^a
XG03 (7D1)	7/16/65	UO ₂ -20 wt % PuO ₂	(2)	GE	32,360	37,000	7.8
XG04 (7B1)	7/16/65	UO ₂ -20 wt % PuO ₂	(2)	GE	33,556	45,000	8.1
X018B (4E2)	10/2/69	Structural	(3)	GE	8,050	10,000	3.0 + 5.8 ^b = 8.8
		Structural	(2)	ANL			3.0 + 5.8 ^b = 8.8
		Structural	(1)	ANL			3.0
		Structural	(1)	PNL			3.0
X021C (2D1)	4/17/70	Structural	(3)	PNL	3,594	3,200	1.5
		Structural	(4)	PNL			1.5 + 8.3 ^b = 9.8
X034A (2F1)	9/30/69	Structural	(3)	ORNL	8,050	7,500	3.4 + 4.8 ^b = 8.2
		Structural	(4)	ORNL			3.4
X035 (7B3)	4/13/68	Structural	(7)	ORNL	20,634	44,800	4.7
X036 (7E1)	7/25/68	UO ₂ -25 wt % PuO ₂	(19)	GE	18,240	43,300	4.9
X042B (7D5)	3/4/70	Structural	(5)	PNL	4,712	6,400	1.0 + 2.1 ^b = 3.1
		Structural	(2)	PNL			1.0
X051 (3A2)	12/16/68	UO ₂ -25 wt % PuO ₂	(37)	PNL	14,501	18,200	2.8
X055 ^c (6A4)	2/23/69	(U _{0.85} -Pu _{0.15})C	(19)	UNC	14,726	20,000	4.6
X056 ^d (5C2)	4/2/69	UO ₂ -25 wt % PuO ₂	(37)	GE	13,356	13,000	6.3
X057 (2B1)	2/23/69	Structural	(7)	PNL	14,726	16,000	6.2
X058 (6F1)	4/24/69	UO ₂ -25 wt % PuO ₂	(37)	GE	12,780	16,000	4.7
X059 (4A1)	4/23/69	UO ₂ -25 wt % PuO ₂	(37)	PNL	12,780	17,500	4.2
X061 (7A5)	4/23/69	Structural	(7)	INC	13,550	18,000	2.9
X062 (6F3)	5/23/69	UO ₂ -25 wt % PuO ₂	(37)	GE	10,877	13,400	4.7
X064 (4F2)	5/28/69	UO ₂ -25 wt % PuO ₂	(19)	GE	11,648	11,400	6.0
X065D (7E5)	6/25/70	Structural	(26)	ANL	900	1,350	0.2
X068 (4A3)	1/30/70	Mark IA	(61)	ANL	6,079	9,700	1.9
X069 (4F1)	10/1/69	UO ₂ -25 wt % PuO ₂	(37)	PNL	8,050	20,700	2.7
X070 (3E1)	1/10/70	UO ₂ -20 wt % PuO ₂	(8)	NUMEC	6,679	6,000	3.4 + 6.2 ^b = 9.6
		UO ₂ -20 wt % PuO ₂	(7)	GE			3.7 + 5.4 ^b = 9.1
		(U _{0.8} -Pu _{0.2})C	(1)	LASL			3.5 + 1.4 ^b = 4.9
		(U _{0.8} -Pu _{0.2})C	(1)	LASL			3.6
		(U _{0.8} -Pu _{0.2})C	(1)	W			3.7
		(U _{0.8} -Pu _{0.2})N	(1)	BMI			3.6
X072 (6B2)	12/12/69	UO ₂ -20 wt % PuO ₂	(18)	ANL	7,450	9,200	2.9
		Structural	(1)	ANL			1.9
X073 (6C3)	12/12/69	UO ₂ -25 wt % PuO ₂	(37)	PNL	7,450	29,600	1.8
X074 (5A2)	1/10/70	UO ₂ -25 wt % PuO ₂	(37)	PNL	6,679	14,500	3.1
X075 ^d (5E4)	1/30/70	(U _{0.8} -Pu _{0.2})C	(18)	UNC	6,079	6,000	2.8 + 6.0 ^b = 8.8
X076 (7D3)	3/27/70	UO ₂ -25 wt % PuO ₂	(19)	W	3,751	15,000	1.3

TABLE I.C.9 (Contd.)

Subassembly No. and (Position)	Date Charged	Capsule Content and (Number of Capsules)		Experi- menter	Accumulated Exposure, MWd	Estimated Goal Exposure, MWd	Burnup ^a
X077 (8C4)	3/26/70	Structural Structural	(2) (1)	ORNL PNL	3,751	8,100	0.6 0.6
X078 (4E3)	4/17/70	Mark 1A	(1)	ANL	3,594	5,800	1.1 + 2.7 ^b = 3.8
X079 (4B2)	4/17/70	(U _{0.85} -Pu _{0.15})C	(19)	UNC	3,594	6,300	1.9
X081 ^c (7C5)	5/24/70	UO ₂ -25 wt % PuO ₂	(9)	GE	2,250	16,000	0.8 + 6.7 ^b = 7.5
X082 (5E2)	5/24/70	Mark 1A	(61)	ANL	2,250	5,400	0.6 + 1.8 = 2.4
X087 (5B4)	5/24/70	UO ₂ -25 wt % PuO ₂	(61)	PNL	2,250	2,700	0.6
X088 (6F4)	5/24/70	UO ₂ -25 wt % PuO ₂	(19)	W	2,250	12,500	0.6
XX02 (5F3)	4/13/70	UO ₂ -25 wt % PuO ₂	(36)	PNL	3,594	8,000	1.4

^aEstimated accumulated center burnup on peak rod, based on unperturbed flux but considering depletion effects (fuels, at. %; nonfuels, nvt x 10⁻²²).

^bPrevious exposure from another subassembly.

^cX085 relocated to 6A4 after Run 43; X081 to be relocated to 7F5 after Run 44A.

^dTerminated at the end of Run 44A.

During the loading changes for Run 44A, two experimental subassemblies that had reached their exposure goals were removed. They are X041, containing PNL structural-material capsules, and X071, containing ANL Mark-II driver fuel. Reconstituted Subassembly X065D, containing ANL pressurized creep capsules, was installed in the grid. Subassembly X078 was relocated in the grid to recenter the nuclear center of the reactor, and Subassembly X055 was relocated from Row 7 to Row 6.

b. Operational In-cell Handling and Examination Equipment
(M. J. Feldman)

Last Reported: ANL-7640, pp. 44 and 46 (Nov 1969).

(i) Examination Equipment (J. P. Bacca)

New equipment for remote interim and terminal examination of experimental-irradiation capsules and elements is being planned and developed. A prototype of a device to remotely measure the bow and length of irradiated experimental capsules and elements has been developed and placed in operation in the FCF air cell. With this device, the length can be measured to ± 0.001 in. and the bow to ± 0.020 in. Bow location can be determined to $\pm 1/32$ in.

- c. Experimental Support (M. J. Feldman, J. P. Bacca, N. R. Grant, R. V. Strain, S. T. Zegler, J. W. Rizzie, C. L. Meyers, D. B. Hagmann, and G. C. McClellan)

Last Reported: ANL-7705, pp. 120-125 (June 1970).*

(i) Subassembly X012A. Measurements were made of the diameter and density of the irradiated Type 304L stainless steel tubing of Capsule D-5 and used to calculate the change in volume of the tubing with irradiation. This capsule had been irradiated to a maximum fluence of 7.4×10^{22} nvt ($E > 0.1$ MeV). Diameters were measured at 1-in. intervals along the capsule at 0 and 90° orientations, with a DR-25 optical gauge, both before and after the fuel element was removed from the capsule. Densities were determined on 1-in.-long samples of the capsule tubing.

Figure I.C.3 is a plot of the diameter measurements before and after the element was removed; each point is the average of measurements made at 0 and 90° orientations. The capsule diameters were significantly larger when the element was still in the capsule. Figure I.C.4 is a plot of the density determinations. Figure I.C.5 compares the volume changes of the capsule tubing based on diameter measurements with those based on density measurements. The diameter measurements were converted to percent volume changes by using 0.3755 in.** as the original diameter of the capsule and multiplying by three the $\Delta D/D$ based on this value (assumes isotropic swelling). An original density of 7.900 g/cm³** was used in calculating the percent density change of the tubing. The percent density change was taken to be equal to the percent volume change

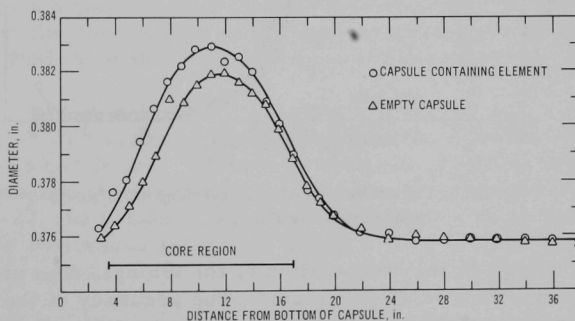


Fig. I.C.3. Diameters of Capsule D-5 from Subassembly X012A

*Previously reported as part of Operations--Fuel Cycle Facility.

**These values are the average of several measurements of the upper portion of the irradiated capsule (see Figs. I.D.3 and I.D.4). This portion is believed to have been far enough from the reactor-core region so as not to have changed in dimensions or density with irradiation.

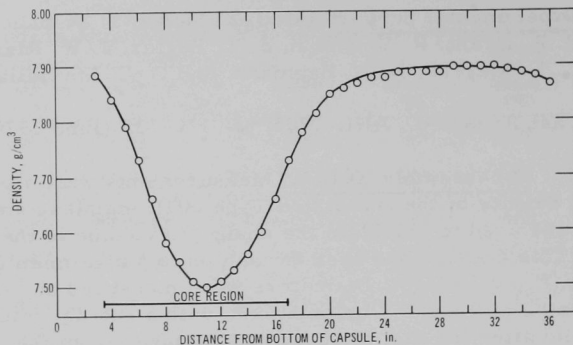


Fig. I.C.4. Density Profile of Tubing of Capsule D-5
from Subassembly X012A

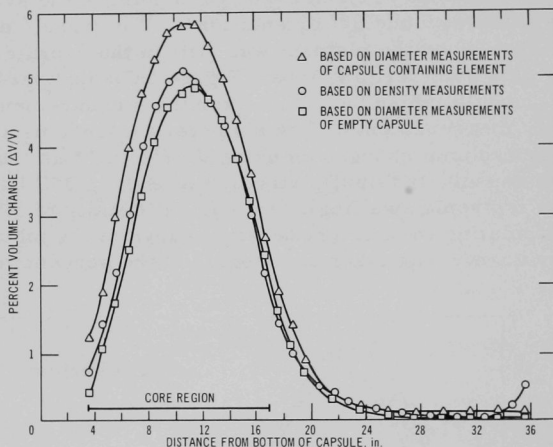


Fig. I.C.5. Percent Volume Change in Tubing of Capsule D-5
from Subassembly X012A

(assumes no change in the composition of the tubing). The precision of the density determinations is $\pm 0.005 \text{ g/cm}^3$. The accuracy of the density determinations is not known, but it is not important, because all the values were compared with the measured values (7.900 g/cm^3) near the top of the capsule.

The volume changes of the tubing based on density determinations do not coincide exactly with the volume changes calculated from either set of diameter measurements. However, they agree much better

with those calculated from the diameter measurements of the empty capsule than with those calculated from the diameter measurements of the capsule when it contained the fuel element. The changes in the diameter of the element were large, so the element may have been exerting a mechanical force on the capsule tubing while it was in the capsule. A calculation of the dimensions of the fuel element and its spacer wire, which took thermal-expansion effects and maximum fabrication tolerances into consideration, indicated that interference would occur between the fuel element and the capsule during reactor operation. Metallographic examination of samples of the capsule tubing revealed small defects at the inside diameter of the tubing that could have resulted when the element was withdrawn from the capsule. This evidence also indicated that the element had swollen sufficiently to force the spacer wire of the element against the inner diameter of the capsule.

These results indicate that diameter measurements on the Mark-A19 capsules may not be reliable for determining swelling of stainless steel at fluences above about 8×10^{22} nvt total, especially if fuel element-to-capsule interference is present.

(ii) Subassembly X027. Interim examination of Subassembly X027 was completed. This Mark-A19 subassembly contained 18 GE encapsulated mixed-oxide elements with maximum burnup of 9.7 at. % and one PNL structural capsule. A summary of the results of the interim examination is as follows:

(1) Longitudinal scratches were observed on the capsules. These scratches appear to have been caused by an interference fit between the cladding at the core region of the capsule and the dimples of the shroud tube near the bottom of the hexagonal can, and probably occurred during disassembly.

(2) Neutron radiography revealed that the element in GE Capsule EIH-33 had failed. There was evidence of mixing between the insulator regions and the fuel region of the vibratory-packed fuel pins. In Element EIH-22, the bottom insulator pellet appears to be missing. All elements have continuous centerline voids, and in some cases, the pellets appear to be cracked.

(3) Diameter surveys of the capsules revealed a maximum diameter change of 0.0060 in. ($\Delta D/D = 1.69\%$). The measured diameter profiles agree quite well with profiles calculated using the Westinghouse-PNL equation* for irradiation swelling of stainless steels.

* Claudson, T. T., Barker, R. W., and Fish, R. L., The Effects of Fast Flux Irradiation on the Mechanical Properties and Dimensional Stability of Stainless Steel, Nucl. Appl. Tech. 9(1), 10 (1970).

Twelve of these capsules are to be loaded into a new subassembly for further irradiation. Special hardware will be used to accommodate the 0.004- to 0.006-in. maximum diameter increases measured for these capsules.

(iii) Subassembly X038. Postirradiation examinations have been completed on this Mark-B7 irradiation subassembly. The subassembly, which contained only structural samples, had accumulated a fluence of $\sim 3 \times 10^{22}$ nvt ($E > 0.1$ MeV).

The hexagonal can of the subassembly enlarged by as much as 0.015 in. ($\sim 2/3\%$) across the flats at a location near the EBR-II core midplane. A diametral profile along the axis of each capsule revealed that all had expanded somewhat, predominantly within a longitudinal range of about 29-31 in. above the bottom of each capsule, a location near the EBR-II core midplane. The diametral expansion ranged from 0.002 to 0.004 in. ($\Delta D/D \approx 1/4$ - $1/2\%$); the lesser amount was found on a capsule on the side of the subassembly away from the EBR-II core centerline. The capsules have been returned to the experimenter. The hexagonal can will be cut longitudinally into two halves, one to be examined at Atomics International and the other retained at the FCF for future EBR-II Project examinations.

(iv) Subassembly X040A. Interim examination of Subassembly X040A was completed. This Mark-B37 irradiation subassembly contained 16 GE and 18 ANL mixed-oxide elements irradiated to a maximum burnup of 5.8 at. % (maximum total fluence of 4.3×10^{22} nvt). Some of the GE elements had Type 316 stainless steel cladding, and some had Type 304L stainless steel cladding. All ANL elements had Type 304L stainless steel cladding. The examination results are summarized as follows:

(1) Measurements of the subassembly hexagonal tubing indicated an increase of 0.005 in. in the flat-to-flat dimension in the core region and a slight increase (0.059 in. increase in total indicated runout), based on pre- and postirradiation measurements, in the bow of the subassembly.

(2) Visual examination indicated no abnormal conditions on the element surfaces.

(3) Neutron radiography revealed no unusual or abnormal features in the elements.

(4) Diameter surveys revealed maximum diameter changes of ~ 0.0017 in. ($\Delta D/D = 0.6\%$) for the GE elements clad with Type 316 stainless steel, ~ 0.0032 in. ($\Delta D/D = 1.1\%$) for the GE elements clad with Type 304L stainless steel, and 0.0043 in. ($\Delta D/D = 1.5\%$) for the ANL elements (all clad with Type 304L stainless steel). The differences in

diameter changes of the GE elements may be due to differences in the creep strengths of the Types 316 and 304L stainless steel claddings. The differences in diameter changes of the GE elements clad with Type 304L and the ANL elements (all clad with Type 304L) may be due to the difference in the design of the elements.

(5) Bow measurements of the elements indicate that the elements tend to bow away from the center of the subassembly at the mid-lengths of the elements, thus indicating that the bow is caused by thermal gradients within the subassembly rather than by a flux gradient across the subassembly.

(6) Length measurements of the GE elements revealed maximum length changes of ~ 0.086 in. for the elements clad with Type 304L stainless steel and ~ 0.024 in. for those clad with Type 316 stainless steel. Length increases for the ANL elements (all clad with Type 304L), calculated on the basis of nominal preirradiation values, were 0.050-0.080 in.

(v) Subassembly X050. Interim examination of Subassembly X050 was completed. This subassembly contained 12 GE encapsulated mixed-oxide elements (average burnup for lead element, 11.3 at. %), five ORNL encapsulated mixed-oxide elements (average burnup, 5.4 at. %), and two Westinghouse encapsulated mixed-carbide elements (average burnup, 5.4 at. %). A summary of the results of the examination is as follows:

(1) Shallow longitudinal scratches were observed on the capsules; these apparently resulted from the rubbing of dimples on the shroud tubes while the hexagonal can was being removed during disassembly.

(2) Neutron radiography clearly revealed failure in the Type 347 stainless steel cladding of GE mixed-oxide element F2D. Neutron radiography also revealed possible failures in Westinghouse mixed-carbide elements W2X and W8X. No failure was indicated in the outer cladding (the capsule) of any of the three elements.

(3) Diameter surveys of the capsules revealed a maximum diameter change of ~ 0.010 in. ($\Delta D/D = 2.6\%$) for the GE capsules. This diameter change was appreciably higher than the maximum change calculated using the Westinghouse-PNL equation for irradiation swelling of stainless steel.

(vi) Subassembly X065D. For the ANL experiment on in-core creep, 25 helium-pressurized tubes and 12 dummy elements were loaded into this subassembly for further irradiation. Twenty-one of the pressurized tubes began their fifth irradiation cycle in reactor run 44.

(vii) Subassembly X071. This subassembly, containing 37 encapsulated Mark-II driver elements with a burnup of about 6 at. %, has been received from the reactor and dismantled. Interim examination is under way.

(viii) Subassembly X080. As reported last month, Subassembly X080 could not be assembled because misalignment caused by the bow of the NUMEC mixed-oxide capsules previously irradiated in Subassembly X012A prevented the upper preassembly from being completely lowered. (Subassembly X080 also was to contain GE capsules of structural elements previously irradiated in Subassembly X039.)

The capsules from Subassembly X012A have been reexamined to determine the depth of the longitudinal scratches observed on them during the interim examination of Subassembly X012A and to determine the magnitude and direction of the bow of the capsules. The examination of the scratches consisted of visual and photographic observation of the capsules through a stereomicroscope and metallographic studies of samples from Capsule D-5. The maximum scratch depth found during the metallographic studies on transverse sections from the region of maximum diameter of Capsule D-5 was 0.001 in. A comparison of the most severe scratches (as viewed through the stereomicroscope) on Capsule D-5 and on the other capsules from Subassembly X012A after the attempt to load them into Subassembly X080 indicates that the severity of the scratches is quite similar. Therefore, it appears that the most severe scratch on the capsules has a depth of the order of 0.001 in.

Bow measurements of these capsules were made on a device capable of measuring the magnitude of the bow (deviation from a straight line through the ends of the capsules) to an accuracy of ± 0.020 in. and the direction of the bow to $\pm 1^\circ$. The measurements show that all the capsules were bowed parallel to the subassembly grid bars and that Capsules C-1, C-11, and C-15 had significantly greater bow than the other capsules from Subassembly X012A. It has been recommended that these three capsules not be irradiated further because they would be hard to load into a subassembly.

5. Materials-Coolant Compatibility (D. W. Cissel)

a. Evaluation and Surveillance of EBR-II Materials

Last Reported: ANL-7705, pp. 69-70 (June 1970).

(i) Substitution of Other Stainless Steels for Type 304 Stainless Steel (S. Greenberg and W. E. Ruthen)

This screening program has been terminated. Metallographic examination and weight-change data indicated unacceptable behavior

of the "free-machining" grades of stainless steel. The weight-change data for all the stainless steels tested are summarized in Table I.C.10.

TABLE I.C.10. Weight Changes of Stainless Steels Exposed in Sodium

Type of Stainless Steel	Sample No.	Temp, °F	Sodium Velocity, m/sec	Weight Change, in mg/cm ² , after ...				
				34 days	35 days	69 days	77 days	146 days
304	2 ^a	700	2.0		-0.0068	-0.014		+0.014
304	4 ^b	700	1.0		0.00	-0.028		-0.041
304	1 ^c	1050	2.0		-0.068	-0.12		-0.17
304	3 ^b	1050	1.0		-0.062	-0.090		-0.12
301	2	700	2.0		0.00	-0.027		+0.04
301	4	700	2.0		+0.014	-0.014		+0.04
301	6 ^d	700	1.0		+0.014			
301	1	1050	2.0		-0.069	-0.14		-0.19
301	3	1050	2.0		-0.082	-0.12		-0.15
301	5 ^d	1050	1.0		-0.041			
304LN	2	700	2.0		+0.022	-0.022		+0.033
304LN	4 ^e	700	1.0		+0.022	-0.011		+0.019
304LN	1	1050	2.0		-0.076	-0.13		-0.18
304LN	3 ^e	1050	1.0		-0.065	-0.098		-0.14
201	2	700	2.0		+0.037	-0.037		+0.11
201	4	700	2.0		+0.037	-0.074		+0.074
201	6 ^d	700	1.0		+0.074			
201	1	1050	2.0		-0.15	-0.26		-0.33
201	3	1050	2.0		-0.074	-0.18		-0.29
201	5 ^d	1050	1.0		-0.037			
316	2	700	2.0				+0.024	
316	4	700	1.0				+0.037	
316	1	1050	2.0				-0.073	
316	3	1050	1.0				-0.073	
303	2	700	2.0		-0.064	-0.091		
303	4	700	2.0		-0.064	-0.10		
303	6 ^d	700	1.0		-0.073			
303	1	1050	2.0		-0.46	-0.51		
303	3	1050	2.0		-0.45	-0.51		
303	5 ^d	1050	1.0		-0.48			
203EZ ^f	2	700	1.0	-0.10				
203EZ	4	700	1.0	-0.10				
203EZ	1	1050	1.0	-0.38				
203EZ	3	1050	1.0	-0.38				
303CMC ^g	21	700	1.0	-0.15				
303CMC	4	700	1.0	-0.13				
303CMC	1	1050	1.0	-0.27				
303CMC	31	1050	1.0	-0.29				

^aFirst (leading) sample exposed to sodium.

^bSample was cut approximately in half after first exposure period to provide samples for metallographic examination.

^cSample may have been slightly damaged when removing it from holder after last exposure period.

^dRemoved from test for metallographic examination after first exposure period.

^ePart of sample removed for metallographic examination after second exposure period.

^fAllegheny-Ludlum: C, 0.05 wt %; Mn, 6.00 wt %; P, 0.03 wt %; S, 0.30 wt %; Cr, 17.00 wt %; Ni, 6.00 wt %; Cu, 2.00 wt %; Fe, balance.

^gArmco: C, 0.15 wt % max; Mn, 2.00 wt % max; P, 0.20 wt % max; S, 0.15 wt % min; Si, 1.00 wt % max; Cr, 17.00-19.00 wt %; Ni, 8.00-10.00 wt %; Mo, 0.60 wt % max; Fe, balance.

The weight changes of the 18.8 materials are comparable. (Type 304LN, one of the 18.8 materials, is Type 304L to which ~0.14% nitrogen is added. It is a U.S. Steel experimental alloy designed for increased resistance to intergranular corrosion.)

The small size of the available samples of Type 201 reduced the accuracy of their measurements.

(ii) Prooftesting of Bellows Valves for Radioactive Sodium Chemistry Loop (W. E. Ruther and D. J. Dorman)

Belloseal valves manufactured by Wm. Powell were operated for 5000 complete cycles while containing sodium at 700°F and 30 psig. No evidence of bellows failure or other operating difficulty was noted. The valves tested were a standard, hand-operated, 1-in. valve and a tandem-bellows, air-operated, 2-in. valve. These tests were part of the quality-assurance program for the radioactive sodium-chemistry loop (RSCL).

The cycled bellows will be given a complete metallographic examination. The valves have been returned to Wm. Powell for refitting with new bellows.

6. Reactor Analysis, Testing, and Methods Development

Last Reported: ANL-7705, pp. 79-102 (June 1970).

a. Nuclear, Thermal, and Hydraulic Surveillance

(i) Evaluation of Fission-gas Monitor (G. S. Brunson)

As part of an effort to extract all the information possible from data for activity in the cover gas, some studies have been done with the fission-gas monitor (FGM). A 512-channel pulse-height analyzer was connected to the auxiliary channel of the FGM. The detectors in both channels are 2 x 2-in. NaI (Tl) crystals, but the auxiliary channel was used because it appears to have better energy resolution.

The plotted points in Fig. I.C.6 are the data from an 800-min count. For comparison, the solid line gives the FGM spectrum obtained with a similar detector in 1963, when the equipment was installed at EBR-I.* Although the same isotopes are present, there is a marked difference in the relative abundance of ^{88}Rb and ^{138}Cs . Presumably, this difference occurs because ^{88}Kr , the precursor of ^{88}Rb , has a half-life of 2.8 hr and ^{138}Xe has a half-life of only 17 min. Hence, the ^{88}Kr has a far higher probability of disengaging from the EBR-II core and appearing in a higher concentration in the cover gas.

*Smith, R. R., and Doe, C. B., Fission Product Monitoring in EBR-I, Mark IV, ANL-6788 (Jan 1964).

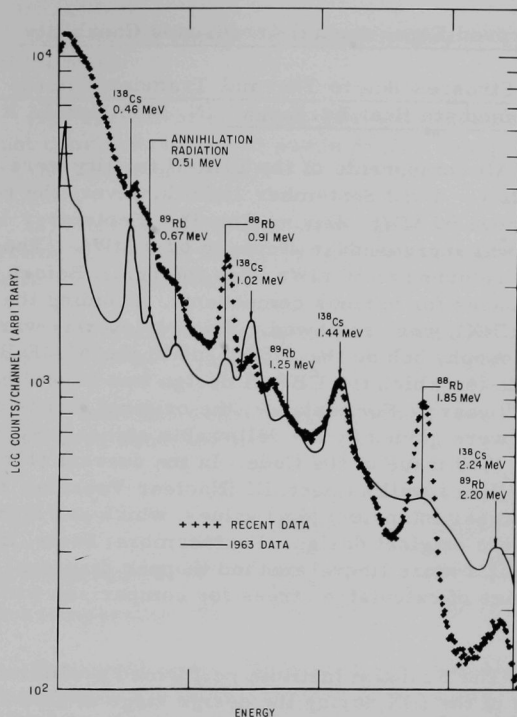


Fig. I.C.6. Gamma Spectra of Fission-gas Monitor Taken Recently and in 1963, When Monitor Was Installed at EBR-I

During this work, some other characteristics of the FGM were noted. During the life of a spool of wire that carries the precipitated ions in the FGM, the effective diameter of the take-up spool changes by a factor of about two. The speed of the wire, and thus the transit time for the precipitated ions, changes proportionately. (The median wire speed is roughly 1 fpm, and the average transit time for the precipitated ions is of the order of $1\frac{1}{2}$ min.) Because of the change in transit time, there is a perceptible change in count rate when a new spool of wire is put on. It was also observed, as had been noted some years ago, that the count rate increased when the volume of collecting water was increased.

b. Improved Experimental-irradiation Capability

(i) Stresses due to Thermal Transients in the EBR-II Intermediate Heat Exchanger (N. Bulut and L. K. Chang)

All components of the EBR-II facility were designed to operate at 62.5 MWt. Until September 1969, however, the reactor had not been operated above 50 MWt. During Run 38A (September 14-28, 1969) the power level was increased, in steps, to 62.5 MWt. (The operating power level was returned to 50 MWt after the run.) Before that run, the original design bases for various components, including the intermediate heat exchanger (IHX), were reviewed. This review was warranted because some of the philosophy behind the 1959 issue of the ASME Boiler and Pressure Vessel Code (on which the EBR-II design was based) has changed within the last 10 years. For instance, the original stress analysis and design for EBR-II were guided by the "allowable stress" (S_a) values of Sect. VIII of the 1959 issue of the Code. In the current (1968) issue, Division 2 of Sect. VIII, as well as Sect. III (Nuclear Vessels), recommends the use of "design stress intensity" (S_m) values, which are higher than the S_a values used for the original design. Furthermore, Sects. III and VIII in the 1968 issue permit a more liberal method (hopper diagram) of combining various categories of calculated stress for comparison with the given values for S_m .

The Franklin Institute performed preliminary and final stress analyses of the IHX during the design stage of EBR-II. Stresses due to static loading and to thermal steady-state and thermal-transient loadings were investigated and reported in 1960. Stresses were calculated for four different loadings:

- (1) Static loading with a secondary-sodium pressure of 150 psig and a reaction force of 1271 lb on the 14-in.-OD pipe through which secondary sodium enters the IHX.
- (2) Steady-state thermal loading with the mean temperature of the center shell 20.9°F higher than that of the tubes.
- (3) Transient thermal loading for a reactor scram that causes the mean temperature of the center shell to be 60°F higher than that of the tubes.
- (4) Transient thermal loading for a failure of the secondary-sodium pump that causes the mean temperature of the center shell to be 60°F lower than that of the tubes and the temperature at the outer edge of the lower tube sheet to be 200°F higher than it is during steady-state operation.

Some of the simplifying assumptions used in making the design calculations were:

(1) The effect of radial flow of primary sodium across the tubes was not considered. It was assumed that hexagonal flow was valid throughout the length of the IHX.

(2) Heat transfer was assumed to occur symmetrically about the centerline of the IHX and to be the same at each elementary hexagon, whose faces are adiabatic.

(3) Overall coefficient of heat transfer was assumed constant ($k' = 63.38 \text{ Btu/hr-ft-}^\circ\text{F}$ for one pipe).

(4) Inlet and outlet temperatures of both primary and secondary sodium were assumed to be:*

	<u>Primary Sodium</u>	<u>Secondary Sodium</u>
Inlet temperature, $^\circ\text{F}$	900 (883)	610 (586)
Outlet temperature, $^\circ\text{F}$	700 (700)	880 (872)

The actual temperature readings show that the second and fourth assumptions were not valid. Temperature readings at the lower orifice plate, which is near the primary-sodium outlet of the IHX, indicated that the primary sodium is channeling along the periphery of the tube bundle. This channeling causes the temperatures of the center and outer shells to be higher than they would be with no channeling. The thermal stresses due to transient as well as steady-state loadings are related directly to the difference between the mean temperatures of the center shell and the tubes. An increase in the mean temperature of the center shell, therefore, would increase the thermal stresses in the IHX.

The indication of channeling motivated planning for a study of the stresses in the IHX under current operating conditions. In the first phase of the two-phase study, the response of temperatures at selected points to various operating anomalies such as scram of the reactor, failure of the flow of primary sodium and of secondary sodium, and unusual temperature excursions of the secondary sodium will be determined. In the second phase, the IHX stresses caused by the anomalies will be calculated.

*For comparison, actual values (in parentheses) obtained during Run 38A have been included.

Five loadings will be studied:

- (1) Steady-state thermal loading.
- (2) Transient thermal loading for a reactor scram, followed 2 sec later by shutdown of the secondary-sodium pump (all primary-sodium pumps--two main and one auxiliary--remaining in operation).
- (3) Transient thermal loading for a failure of the secondary-sodium pump, followed 5 sec later by a reactor scram (all primary pumps remaining in operation).
- (4) Transient thermal loading for failure of all primary-sodium pumps, followed 0.2 sec later by a reactor scram that, in turn, is followed 2 sec later by shutdown of the secondary-sodium pump.
- (5) Transient thermal loading for a sudden drop in the temperature of the secondary sodium while the temperature of the primary sodium entering the IHX and the flows of the primary and secondary sodium through the IHX remain constant.

A computer program referred to as EBRIHX* has been written using S/360-CSMP.* This program is capable of determining the response of the various temperatures in the IHX to time-dependent variations in flow and temperature of the primary and secondary sodium.

c. Computational Methods and Data Development

- (i) Gamma Heating in EBR-II (L. B. Miller, R. E. Jarka, and P. Fullerton)

(a) Gamma-energy Balance. Additional checks have been made of the computations of gamma-ray flux for EBR-II. The most significant of these checks was a comparison of the total gamma energy deposited in the reactor per second with the total energy of all the gamma rays produced in the reactor per second.

The total energy produced by fission and subsequent neutron capture (as reported by M. F. James of Winfrith) is distributed as shown in Table I.C.11. Additional gamma rays (besides those identified in the table) are produced by conversion of 85% of the neutron kinetic energy to gamma rays through inelastic scattering collisions. The sum of the energy produced by these gamma rays and the gamma energy shown in

*Based on a code developed by J. F. L. M. Brukh and J. H. Tessier and described in "Serial Solution of Non-linear Partial Differential Equations of a Counterflow Heat Exchanger Using S/360-CSMP," presented at the Computer Simulation Conference, Denver, Colorado, June 1970.

Table I.C.11 is the total gamma energy (listed in Table I.C.12) to be included in the gamma-heating calculations.

TABLE I.C.11. Distribution of Energy Produced by
Fission and Neutron Capture (MeV/fission)

	^{235}U	^{238}U
<u>Energy Produced and Deposited in Reactor</u>		
<u>Kinetic Energy</u>		
Fission products	166.2	166.9
Neutrons (net kinetic energy)	4.8	2.4
Beta particles	7.0	8.9
Total	178.0	178.2
<u>Gamma Energy</u>		
Prompt	8.0	7.5
Delayed	7.2	8.4
(n, γ)	9.2	9.2
Total	24.4	25.1
Total	202.4	203.3
<u>Energy Not Deposited</u>		
Antineutrinos	9.6	11.9
Total Energy Produced	212.0	215.2

TABLE I.C.12. Total Gamma Energy (MeV/fission)
Including Gammas from Inelastic Scattering

	^{235}U	^{238}U
Total gamma energy from Table I.C.11	24.4	25.1
Neutron kinetic energy converted to gammas	4.1	2.0
Total gamma energy	28.5	27.1

The kinetic energy of the fission fragments and the beta particles is, of course, converted to gamma rays as these charged particles are slowed down. However, this radiation is very soft and is absorbed within a few millimeters of the point of fission. The energy from this radiation, therefore, is considered to be converted directly to heat at the point of fission and is not included in the gamma-heating calculations.

The total gamma energy resulting from fission in ^{235}U and ^{238}U , as given in Table I.C.12, and the relative rates of fission in ^{235}U and ^{238}U in EBR-II were used to compute the average gamma energy per fission (28.3 MeV) and the total energy deposited in the reactor per fission (202.6 MeV). Therefore, 14% of the total energy deposited is included in the gamma-heating calculation. This means that if the reactor is operating at 50 MWt, 7.0 MWt is in the form of gamma energy. Essentially all this energy is deposited in the reactor; according to the gamma-transport calculations, only 0.014% of the gamma rays leak from the reactor reflectors and blanket.

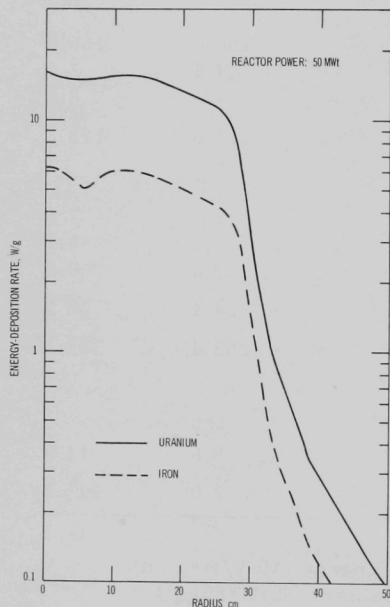


Fig. I.C.7. Rates of Deposition of Gamma Energy vs Radius at Midplane of EBR-II Run -31F Core

According to gamma-production and -transport calculations based on the correct neutron-flux level but otherwise unnormalized, the total gamma energy deposited in the reactor was 5.342. The calculated gamma fluxes and heating rates, therefore, should be multiplied by the factor 1.31 to conserve the gamma energy produced in the reactor. This factor should be applied to the preliminary curves of gamma-heating rate per cm^3 versus position given in earlier Progress Reports.*

(b) Gamma Heating of Iron and Uranium in EBR-II. Figure I.C.7 shows the rates of deposition of gamma energy per gram of uranium and of iron as a function of radius at the core midplane. Figures I.C.8 and I.C.9 show the rates of deposition of gamma energy for iron and uranium as a function of axial position in Rows 7 and 5 of the reactor. The three figures are based on the gamma flux normalized to conserve the gamma energy produced in the reactor.

*ANL-7669, pp. 81-83 (Feb 1970); ANL-7679, pp. 66-67 (March 1970).

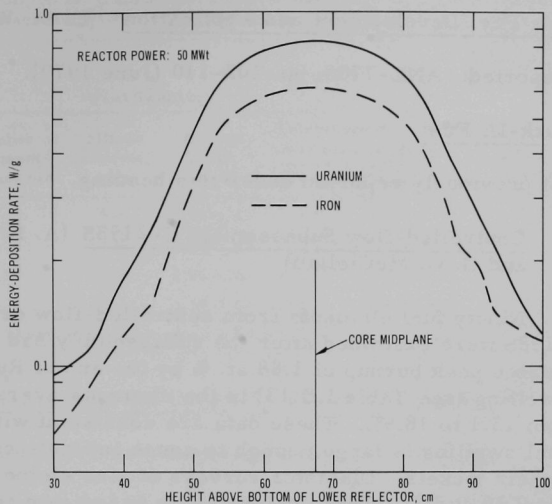


Fig. I.C.8. Rates of Deposition of Gamma Energy vs Axial Location in Row 7 of EBR-II Run-31F Core (averaged over all Row-7 positions)

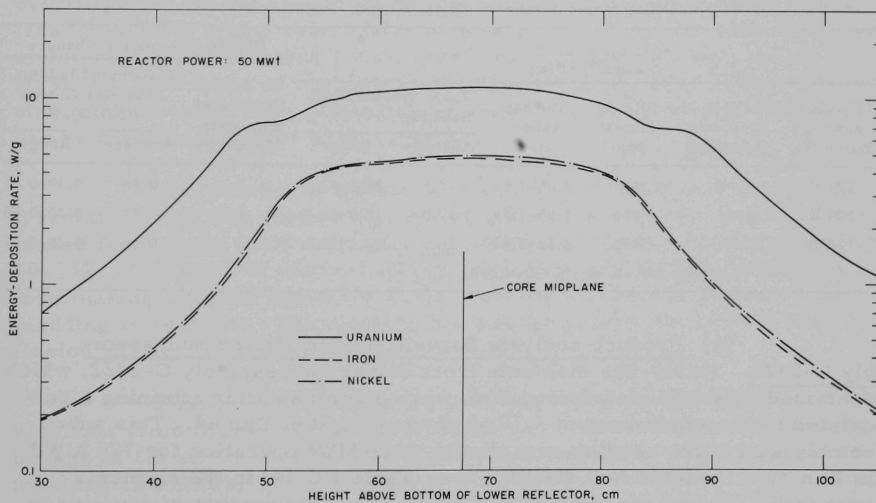


Fig. I.C.9. Rates of Deposition of Gamma Energy vs Axial Location in Row 5 of EBR-II Run-31F Core (averaged over all Row-5 positions)

7. Metal Driver Fuel Development and Application* (C. M. Walter)

Last Reported: ANL-7705, pp. 102-110 (June 1970).

a. Mark-IA Fuel

Not previously reported under this heading.

(i) Controlled-flow Subassembly C-2198S (A. K. Chakraborty and G. C. McClellan)

Ninety fuel elements from controlled-flow driver subassembly C-2198S were examined after the subassembly had been irradiated to a calculated peak burnup of 1.88 at. % by the end of Run 42. Volume fuel swelling (see Table I.C.13) in the elements averaged 17.0% and ranged from 13.1 to 18.9%. These data are consistent with those expected when fuel swelling is large enough to cause intimate contact of the fuel pins with their jackets. Diameter surveys of nine elements indicated $\Delta D/D$ values of 0.20-0.58%. These values seem to indicate the presence of 0.1% creep strain in addition to the diameter increase due to swelling of the stainless steel only.

TABLE I.C.13. Fabrication and Irradiation Data for Controlled-flow Driver Subassembly C-2198S
(Calculated burnup: 1.88 at. % max; 1.65 at. % avg)

Injection-casting Batch No.	Number of Elements Examined	Fuel Swelling				Cladding-diameter Changes		
		Silicon Content, ppm	Burnup Range, at. %	Total Volume Fuel Swelling ($\Delta V/V$), %		Number of Elements Measured	Maximum Cladding- diameter Change ($\Delta D/D$), %	
				Average	Range		Average	Range
127 II	6	336	1.66-1.86	17.1	16.8-17.8	3	0.46	0.39-0.55
129 II	40	314	1.65-1.84	17.0	15.2-18.9	4	0.37	0.20-0.58
132 II	44	323	1.62-1.82	16.9	13.1-18.6	2	0.36	0.35-0.37
Average for elements examined				17.0				

(ii) Product-analysis Surveillance of Driver Subassembly C-2122. Thirty-one elements from driver subassembly C-2122, which contained only ANL-fabricated fuel, were examined after attaining a calculated maximum burnup of 1.70 at. % at the end of Run 40. This subassembly was in the reactor core during 62.5-MWt operation for 770 MWd in Run 38A. Volume fuel swelling (see Table I.C.14) in the elements averaged 7.3% and ranged from 5.9 to 10.2%. This amount of swelling is similar to that observed in the past for ANL-fabricated fuel irradiated to the same burnup level. Diameter surveys of three elements indicated $\Delta D/D$ values of 0.1-0.2%, which can easily be accounted for by swelling of the stainless steel.

*Previously reported under heading "Driver Fuel Development."

TABLE I.C.14. Fabrication and Irradiation Data for Product-analysis Driver
Subassembly C-2122 (Calculated burnup: 1.70 at. % max; 1.44 at. % avg)

Injection-casting Batch No.	Number of Elements Examined	Fuel Swelling		Total Volume Fuel Swelling ($\Delta V/V$), %		Cladding-diameter Changes		
						Number of Elements Measured	Maximum Cladding- diameter Change ($\Delta D/D$), %	
		Silicon Content, ppm	Burnup Range, at. %	Average	Range		Average	Range
0460	2	690	1.62-1.67	6.8	6.3-7.3	0	-	-
4238	15	302	1.58-1.67	7.6	7.1-8.2	1	0.06	-
4241	12	450	1.58-1.66	6.9	5.9-8.0	1	0.17	-
4239	2	530	1.58-1.61	8.5	6.9-10.2	1	0.16	-
Average for elements examined				7.3				

b. Advanced Fuel (Mark II) (W. N. Beck and R. V. Strain)

Not previously reported under this heading.

A total of 546 Mark-II elements are being irradiated in six modified 91-pin subassemblies. The Mark-II element is 26 in. long. The ID and wall thickness of its cladding are 0.150 and 0.012 in., respectively. The fuel pin is made of U-5Fs alloy, 64% enriched, and is 0.130 in. in OD and 14.2 in. long. The pin is sodium-bonded to the cladding; the sodium overfill above the pin is 1.5 in. Eighty percent of the 546 elements being irradiated have crimp restrainers located 0.5 in. above the fuel, 10% have crimp restrainers located 1.0 in. above the fuel, and 10% have no restrainer. Two types of cladding materials--annealed Type 304L stainless steel and annealed Type 316 stainless steel--are being used so that they can be evaluated as part of the program.

The concept of the Mark-II element is based on experimental irradiation data that showed significant quantities of fission gas to be released from metal fuels only after the volume of the fuel has increased by 30-33%. The Mark-II element allows the fuel to expand 33% radially before making intimate contact with the cladding. Thus, the stress on the cladding is kept low. The element has a large plenum for holding the fission gas released from the fuel.

Postirradiation examinations are being completed on Mark-II elements from Subassembly C-2201S that were irradiated to a maximum burnup of 2.2 at. %. The results of the examinations to date are summarized as follows.

Neutron radiographs of 12 elements showed fuel elongations of 0.25-0.9 in. The crimp restrainers located 0.5 in. above the fuel were effective in limiting axial elongation of the fuel. Lengths of elements at the outer edges of the subassembly hexagonal can, where the irradiation

temperatures were lowest, increased less than 0.5 in. There was no significant tendency for the pins to ratchet off the bottom plug, no matter where the restrainer was located.

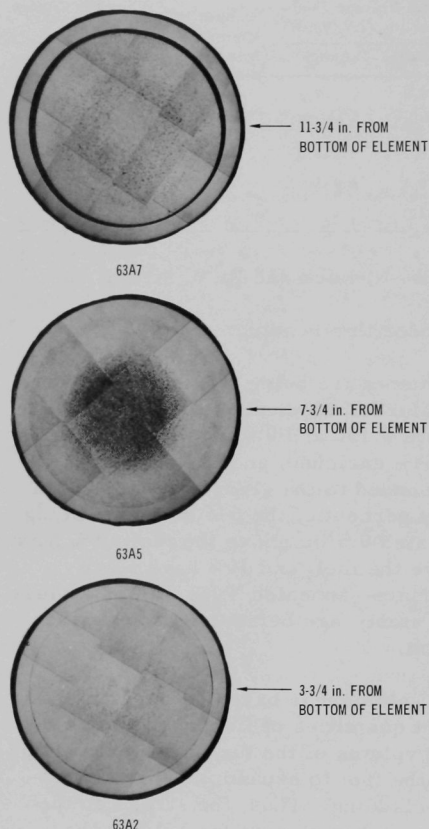


Fig. I.C.10. Transverse Sections of Mark-II Element 24 from Subassembly C-2201S after Maximum Calculated Burnup of 2.2 at. %. Mag. $\sim 8.5X$.

was no more than that observed in Mark-IA elements. At the burnup level of the elements, no clear comparison can be made between the irradiation behavior of the Types 316 and 304L stainless steel claddings.

The plenums of the elements were punctured, and the fission gas was recovered from them. The reduced volume of gas recovered

Diametral measurements of the 12 elements revealed a maximum $\Delta D/D$ of $\sim 0.4\%$, all of which could be attributed to stainless steel swelling. These results are in good agreement with those predicted by BEMOD.

Of the 12 elements, five (No. 24, 34, 46, 54, and 73) have been destructively examined. Transverse sections through different axial positions showed the fuel swollen to make intimate contact with the cladding near the midlength of the fuel, but separated from the cladding at the top and bottom of the fuel. Figure I.C.10 shows macrophotos of Element 24; these are typical for all elements examined, except No. 46. Macrophotos of Element 46 showed a large shrinkage void, which was identified as a casting defect. The microstructure of the fuel near the centerline of all elements indicates the presence of two to three phases, none of which is an acicular phase. This indicates that fuel-centerline temperatures had been below $\sim 640^\circ\text{C}$.

Examination of the fuel-cladding interfaces did not indicate any reaction between the elements in the fuel and those in the cladding. Sensitization of the cladding was observed in the regions above the midplane of the fuel, but the degree

indicated that only a portion of the fuel length had experienced sufficient volumetric expansion to permit interlinking of fission-gas bubbles. A more accurate determination of the percentage of gas being released will be possible when the fuel swells uniformly to fill the inside of the cladding

The results of these examinations show that the elements are performing as predicted and that the element design is capable of achieving much higher burnups.

c. Blanket Studies (A. K. Chakraborty and G. C. McClellan)

Not previously reported under this heading.

Elements from blanket subassembly A-795, which attained a calculated peak burnup of 0.31 at. % at the end of Run 40, have been examined. During its reactor residence, this subassembly was successively in grid position 7B3 (for 8102 MWd) and 7D4 (for 6502 MWd). It had been in the reactor for the 770 MWd of operation at 62.5 MWt in Run 38A. The examination results follow.

(i) Diameter Changes. Precision diameter surveys of the elements were made at 2-in. intervals with the Bausch and Lomb DR-25B. Figure I.C.11 shows the mean values of the diameters of four elements measured at three orientations as a function of the distance from the bottom of the elements. The highest maximum diametral increase ($\Delta D/D$) of the four elements, which came from different corners of the subassembly, was 0.85%; the maximums ranged from 0.32 to 0.85%.

(ii) Burnup Analysis and Burnup Profile. One element (No. 8) was gamma scanned axially at 2-in. intervals to obtain the relative zirconium and niobium activity. Then, one 3/4-in.-long longitudinal sample from the midsection of the element (27 in. from the spade) was analyzed for technetium to determine the actual burnup at that location. This burnup was related to the activity profile from the gamma scan to obtain the burnup profile shown in Fig. I.C.12.

Calculated maximum burnup for this element is significantly higher than the burnup determined by chemical analysis. The maximum burnup calculated with the IPBU (Individual Pin Burnup) code is 0.31 at. %; the maximum burnup determined by chemical analysis is 0.22 at. %.

The production rate and burnup rate for the midsection of the element, as determined from analysis for uranium and plutonium, were:

MWd of Irradiation	U, g	Pu, mg	Pu/U, mg/g	Production Rate, (mg Pu/g U)/MWd	Burnup Rate, at. %/MWd
14,520	18.82	99.0	5.26	3.62×10^{-4}	1.51×10^{-5}

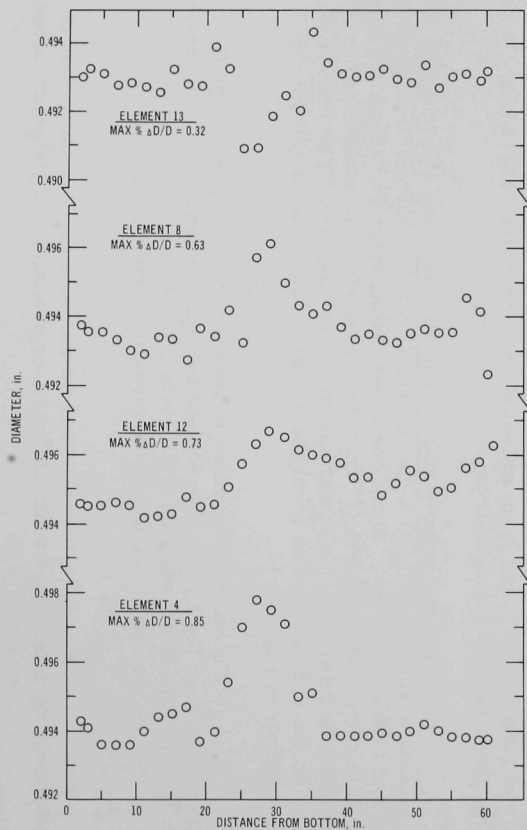


Fig.I.C.11. Diameters of Elements 13, 8, 12, and 4 from Blanket Subassembly A-795

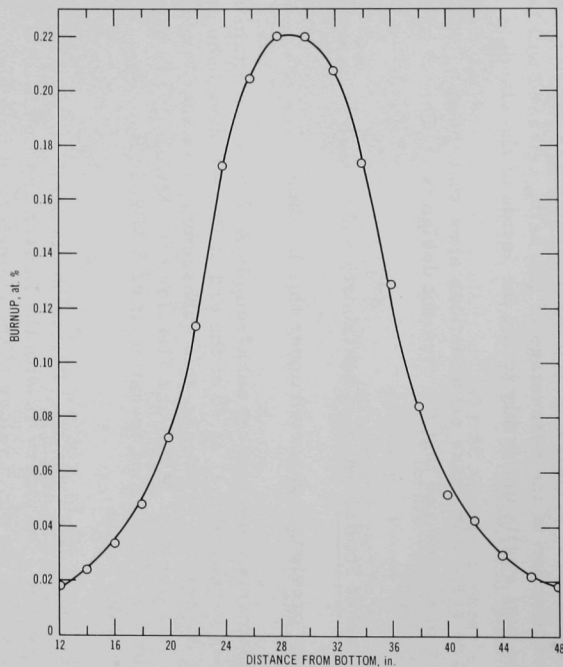


Fig. I.C.12. Burnup Profile of Element 8 from Blanket Subassembly A-795. (Derived from chemically determined burnup and relative zirconium and niobium activity.)

(iii) Cladding Density. Densities of the cladding of Element 8, as determined from 2-in.-long sections, are plotted in Fig. I.C.13 as a function of the distance from the bottom of the element. At the midlength, the density falls abruptly to 0.75% of its maximum value. The decrease in density occurs where the burnup is highest, indicating that the swelling of the stainless steel increases with an increase in burnup and cladding fluence.

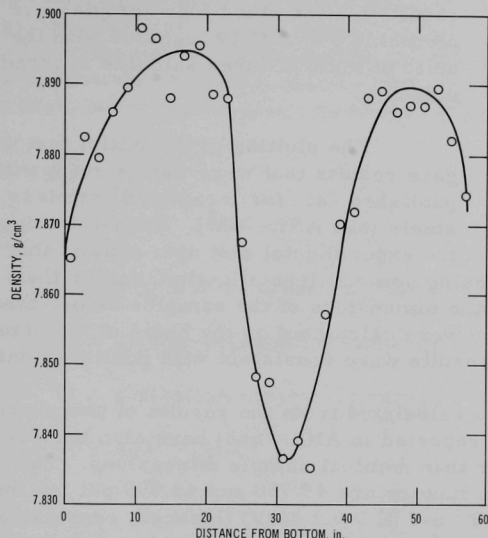


Fig. I.C.13

Density of Cladding of Element 8
from Blanket Subassembly A-795

The maximum diametral change ($0.63\% \Delta D/D$) for Element 8 occurred 27 in. from the bottom end. The contribution of stainless steel swelling to this change, as calculated from the density change, is only $0.25\% \Delta D/D$. The difference between the 0.63 and $0.25\% \Delta D/D$ ($=0.38\% \Delta D/D$) can only be explained by plastic deformation (or creep) of the stainless steel cladding. Calculations with the revised BEMOD code, which computes the effect of creep, show that at a calculated burnup of 0.27 at. % obtained at 50-MWt reactor operation, the contribution of creep to the diameter change is $0.33\% \Delta D/D$ for a blanket rod from Row 7.

d. Cladding Studies (C. L. Meyers)

Last Reported: ANL-7688, pp. 131-132 (April-May 1970).
(Under heading "Cladding Surveillance.")

A surveillance program is being conducted for monitoring the performance of the cladding of EBR-II fuel elements. This program is concerned primarily with irradiation-induced changes in the mechanical and physical properties of the cladding and with the associated changes in microstructure of the cladding.

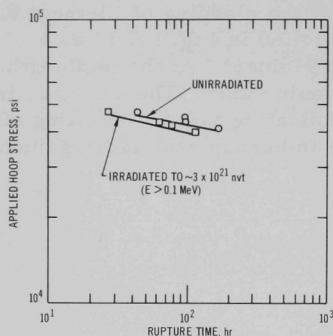


Fig. I.C.14. Results of Stress-to-rupture Tests of Type 304L Stainless Steel Cladding at 950°F

Five more stress-to-rupture tests on samples of unirradiated Type 304L stainless steel cladding were performed at 950°F* in the ANL biaxial rupture-anticipating tubing tester (BRATT). One of these samples failed prematurely near a defect in the inner surface of its wall. The results for the other four samples are plotted in Fig. I.C.14 together with the results of tests of three samples of irradiated cladding.

The plotting of the initial test data gave results that were inconsistent with published data for irradiated stainless steels (see ANL-7688). Reexamination of the experimental test data showed that the inconsistency was caused by using nominal (specification) rather than actual (measured) values for the dimensions of the samples before the test. When hoop stresses at rupture were calculated on the basis of the actual pretest dimensions, the test results were consistent with published data.

The hoop stresses calculated from the results of two short-time burst tests at 950°F (as reported in ANL-7688) have also been recalculated using actual rather than nominal sample dimensions. The recalculated hoop stresses at rupture are 45,750 and 43,900 psi for the samples with zero and $\sim 3 \times 10^{21}$ nvt ($E > 0.1$ MeV) fluences, respectively. The fact that the hoop stress at rupture for the irradiated sample was less than that for the unirradiated sample indicates that there may have been a defect in the wall of the irradiated sample, which caused premature failure. No such defect was detected, however.

Analyses of the sets of data for the unirradiated and the irradiated samples show that the following reasonably satisfactory linear relationships exist for each set when the data are plotted as $\log \sigma_H$ versus $\log t_R$ (where σ_H is the hoop stress at rupture, in psi, and t_R is the time to rupture, in hours:

Data for unirradiated samples

$$\log \sigma_H \approx 4.82 - 0.0919 \log t_R \quad (1)$$

(standard deviation of sample for $\log \sigma_H$ is 0.0144)

Data for irradiated samples

$$\log \sigma_H \approx 4.83 - 0.1135 \log t_R \quad (2)$$

(standard deviation of sample for $\log \sigma_H$ is 0.0078)

*Test temperature selected to be approximately the irradiation temperature.

Several stress-to-rupture parameters were examined as potential means of representing and extrapolating the very limited amount of experimental data now available for this surveillance program. The Larson-Miller and the Manson-Haferd parameters are unsuitable for this purpose, because the tests of the program are limited at present to one temperature. These two parametric methods use graphical constructions (based on data taken over a range of temperatures) to determine the values of the constants for various materials and then use the constants to establish the mathematical relationships for the materials. The Orr-Sherby-Dorn parameter* has been used tentatively as a means of representing the data available from the program tests. This parameter can be expressed as

$$\sigma_H^m = t_R^{-Q/RT}, \quad (3)$$

where

σ_H and t_R are as defined above,

m = stress-dependency exponent,

Q = activation energy for creep,

R = gas constant,

and

T = test temperature, °K.

This relation can also be expressed as

$$\log \sigma_H = -\frac{1}{m}Q/RT + \frac{1}{m} \log t_R. \quad (4)$$

Comparisons of Eq. 1 with Eq. 4 and Eq. 2 with Eq. 4 give the following estimated values for the parameters Q and m :

Data for unirradiated samples

$Q \approx 82,400$ cal/mole;

$m \approx 11.0$.

Data for irradiated samples

$Q \approx 65,900$ cal/mole;

$m \approx 6.95$.

*Frequently called the "Dorn" or the " θ " parameter.

From these values and Eq. 3, the following tentative relationships can be expressed for the stress-to-rupture behavior of the driver-fuel cladding:

Unirradiated cladding

$$\sigma_H = \left(t_R^{-82,400/RT} \right)^{0.091} \quad (5)$$

Irradiated cladding

$$\sigma_H = \left(t_R^{-65,900/RT} \right)^{0.114} \quad (6)$$

Caution must be used, however, when using these relationships. Although the values for Q may be reasonable, the value of m for the unirradiated material is so high that it is difficult to interpret. (It would be expected that m would take some value between -3 and -7.) In addition, the data have been obtained at only one temperature, 950°F (783°K); the values for Q at other temperatures may be different from those determined by this empirical analysis. Therefore, more information and analysis are needed to provide better understanding of Eqs. 5 and 6 so that the applicability of the Orr-Sherby-Dorn parameter (and the closely related Barrett-Ardell-Sherby parameter) to the analysis of the test data can be established. At present, only Eqs. 1 and 2 are recommended for describing the results of biaxial stress-to-rupture tests on Type 304L stainless steel cladding.

8. Hot Fuel Examination Facilities

a. Improvement of Fuel Cycle Facility (M. J. Feldman)

Last Reported: ANL-7705, pp. 111-113 (June 1970).

(i) Leak in Inert-gas System of Argon Cell (N. R. Grant and K. H. Kinkade)

Last month, it was reported that the argon atmosphere of the argon cell had become diluted to 80% air because of a major leak that developed while minor leaks were being searched for. The major leak was subsequently found and stopped. The atmosphere was replenished during the month by adding approximately 120,000 cu ft (approximately two cell volumes) of argon to the cell. After the argon had mixed with the existing cell atmosphere, the oxygen reading was 1.2%. The oxygen content, which is being reduced further by the cell-purification system, will be below 100 ppm by August 1.

9. Characterization of Irradiation Environment* (D. Meneghetti)

Last Reported: ANL-7705, pp. 113-114 (June 1970). (Experimental results for the ZPR-3 assemblies discussed here are reported in Sect. I.A.4, "ZPR-3 and ZPPR Operations and Analysis," of the April-May and June Progress Reports--ANL-7688 and 7705, respectively. Current experimental results are reported in Sect. I.A.3, "ZPR and ZPPR Operations and Analysis," of the present progress report.)

a. Calculated k_{eff} Values for ZPR-3 Assembly 61 (D. Meneghetti, K. E. Phillips, and D. G. Stenstrom)

The nickel-rich, radially reflected ZPR-3 Assembly 61 has a core composition similar to that of the previous ^{238}U -rich, radially reflected ZPR-3 Assembly 60, except that the atom densities (in 10^{24} atoms/cm³) of ^{235}U and ^{238}U are modified from 0.00559 to 0.00508 and from 0.00457 to 0.00505, respectively. The atom-density composition of the ~8.7-in.-thick, nickel-rich reflector is: Ni, 0.0662; Na, 0.00205; Fe, 0.00662; and Cr, 0.00164. This radial reflector is surrounded by an ~8.7-in.-thick blanket with the same composition as in Assembly 60. The reported critical mass, including an estimated correction for excess reactivity, is 208 kg of ^{235}U .

Two-dimensional, RZ-geometry, S_4 -transport calculations with the DOT code gave a k_{eff} value of 1.025. The calculations used 29-energy-group cross sections based on the ENDF/B (Version I) data files and energy collapsed, with the MC² code, specifically for the regional composition of the assembly. The calculated value has been corrected by a reactivity increment of 0.009 $\Delta k/k$ to account for thin-plate heterogeneity. It has not, however, been corrected for the hexagonal shape of the radial outline of the core.

b. Radial and Axial Reaction-rate Traverses for ZPR-3 Assembly 61 (D. Meneghetti, D. G. Stenstrom, and K. E. Phillips)

Radial and axial reaction-rate traverses for ZPR-3 Assembly 61 have been calculated based on the flux solutions of the two-dimensional, RZ-geometry, S_4 approximations and compared with experimental values reported by the ZPR-3 experimental group in the Progress Reports for April-May 1970 (ANL-7688, pp. 50-53) and June 1970 (ANL-7705, pp. 33-38). Figures I.C.15, I.C.16, and I.C.17 compare the calculated and experimental values for radial traverses for $^{235}\text{U}_f$, $^{238}\text{U}_f$, and $^{10}\text{B}_c$, respectively, in the axial midplane. Figures I.C.18 and I.C.19 compare the calculated and experimental values for central axial traverses for $^{235}\text{U}_f$ and $^{238}\text{U}_f$, respectively; Figs. I.C.20 and I.C.21 make analogous comparisons for axial traverses

*Previously reported under heading "Physics Mock-up Studies."

approximately one-half core drawer in from the radial interface of the core and blanket. In all cases, the 29-group cross sections used for the detectors corresponded to the MC² averaging of the particular regional composition.

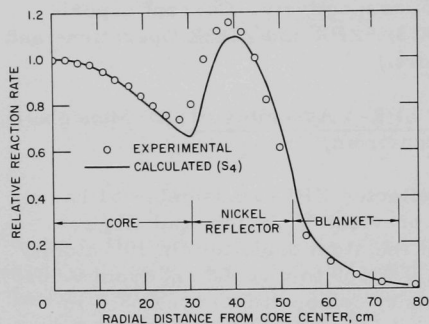


Fig. I.C.15. ^{235}Uf Radial Traverse at Axial Midplane of Core of ZPR-3 Final Assembly 61

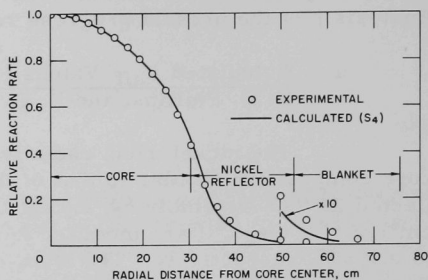


Fig. I.C.16. ^{238}Uf Radial Traverse at Axial Midplane of Core of ZPR-3 Final Assembly 61

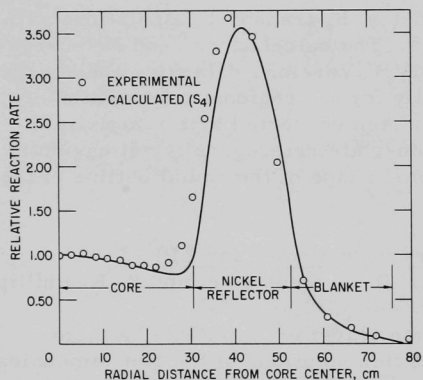


Fig. I.C.17. ^{10}Bc Radial Traverse at Axial Midplane of Core of ZPR-3 Final Assembly 61

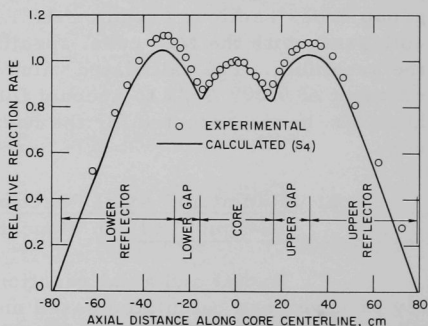


Fig. I.C.18. ^{235}Uf Central Axial Traverse of ZPR-3 Final Assembly 61

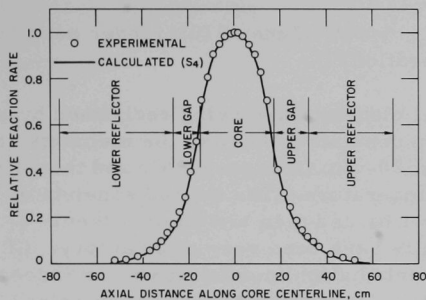


Fig. I.C.19. $^{238}\text{U}_f$ Central Axial Traverse of ZPR-3 Final Assembly 61

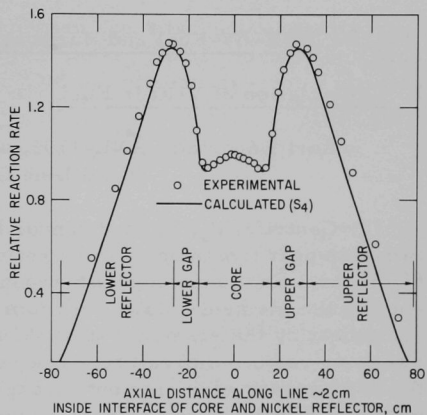


Fig. I.C.20. $^{235}\text{U}_f$ Axial Traverse near Radial Interface of Core and Nickel Reflector of ZPR-3 Final Assembly 61

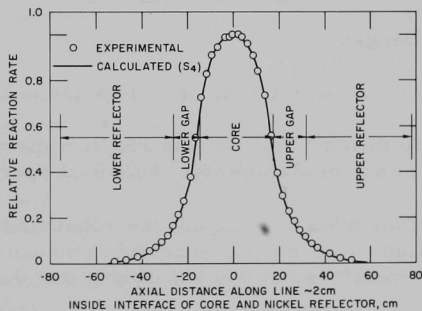


Fig. I.C.21. $^{238}\text{U}_f$ Axial Traverse near Radial Interface of Core and Nickel Reflector of ZPR-3 Final Assembly 61

D. EBR-II--Fuel and Hardware Procurement (M. J. Feldman)

1. Reclamation of Vendor Fuel (D. L. Mitchell)

Last Reported: ANL-7705, pp. 115-116 (June 1970) (under heading "Cold Line Operations").

Centrifugally bonded vendor fuel elements are being reclaimed by a two-step heat treatment. The first step consists of heating the elements at 660°C for 1 hr, quenching with argon (at 20-cfm flow) to 350°C, and then air-cooling the elements slowly to room temperature. The second consists of again heating the elements at 510°C for 1 hr and then air-cooling them slowly to room temperature. The results have been very satisfactory. Of the 473* vendor elements put through reclamation to date, 458 were "accept" elements and 15 were "reject" elements. The principal causes for rejection were size of bubbles and voids** in the sodium bond. The "reject" elements may be reclaimed by impact bonding; or they may prove acceptable on the basis of the approved Revision 7 of Specification FCF-1.

E. EBR-II--Operations

1. Reactor (G. E. Deegan)

Last Reported: ANL-7705, pp. 116-117 (June 1970).

From June 16 through July 15, the reactor operated for 1277 MWd in Runs 43 and 44A. The accumulated total of EBR-II operation is 37,490 MWd.

Run 43 was concluded on June 23, the scheduled shutdown date, after 1350 MWd of operation. Rod-drop kinetics were measured and noise of the primary pumps was monitored at 500 kW during the shutdown.

Fuel handling for Run 44A was accomplished, and the reactor was started up again on June 26. After the reactor was critical, a toggle switch for raising and lowering a control rod failed. The reactor was shut down, the switch was replaced, and the reactor was restarted. Run 44A, a 900-MWd run, was completed without interruption on July 15.

During the shutdown between Runs 44A and 44B, the 5-ton hoist on the reactor-building crane was replaced by a 20-ton hoist. Scheduled fuel handling was interrupted by difficulty in inserting Subassembly C-2158 in

* Heat-treating runs are being made on a limited basis while production equipment is being installed.

** Rejection for void size was based on the definition in Revision 6 of Specification FCF-1, Product Specification for the EBR-II Elements. Revision 7 of this specification, which allows acceptance of larger void sizes (radial width of 125 mils) than does Revision 6, has been approved, but the present sodium-bond testers can measure voids having a radial width up to only about 80 mils. New sodium-bond testers are being procured to measure the larger voids acceptable under Revision 7.

core position 5A4. This position is between control-rod thimbles 8 and 9. Because of previous problems in positions adjacent to control rod 8, the decision was made to remove and replace the thimble for the rod. In addition, replacement of safety-rod thimble 1, which had been scheduled for the end of Run 44B, was advanced to this shutdown to reduce plant downtime.

Fuel handling for Run 44A involved experimental subassemblies, as reported under Sect. I.D.4.a, and also included the following changes: Two surveillance subassemblies containing Mark-II driver fuel elements, one containing impact-bonded vendor fuel elements, and one containing vendor fuel elements in which the centrifugally cast fuel pins had been inverted were removed from the grid. Three surveillance subassemblies containing impact-bonded vendor fuel elements and one controlled-flow subassembly containing impact-bonded vendor fuel elements were installed.

2. Fuel Cycle Facility (M. J. Feldman)

a. Fuel Assembly (D. L. Mitchell)

Last Reported: ANL-7705, pp. 115-116 (June 1970) (under heading "Cold Line Operations").

Thirty-one Mark-IA subassemblies containing vendor-fabricated elements were assembled in the cold line during this reporting period. As of July 15, 22,643 vendor-fabricated elements were available after verification inspection. (This figure does not include the vendor elements impact-bonded by ANL.) Table I.E.1 summarizes the production activities for June 16 through July 15, 1970, and for fiscal years 1970 and 1971.

b. Fuel Handling and Transfer (N. R. Grant, W. L. Sales, and K. DeCoria)

Last Reported: ANL-7705, pp. 120-123 (June 1970).

Table I.E.2 summarizes the fuel-handling operations performed.

c. Reactor Support (J. P. Bacca and N. R. Grant)

Last Reported: ANL-7705, p. 125 (June 1970).

Nineteen depleted-uranium, inner-blanket subassemblies were fabricated, inspected, and transferred to the reactor for use as needed. Hardware and blanket elements are available for at least 50 additional subassemblies.

TABLE I.E.1. Production Summary for FCF Cold Line

	FY 1970		FY 1971	
	6/16/70 through 6/30/70	Totals for FY 1970	7/1/70 through 7/15/70	Totals for FY 1971
Subassemblies Fabricated with Mark-IA Fuel				
With cold-line elements	0	46	0	0
With vendor elements	18	71	13	13
Preirradiation Treatment of Vendor Mark-IA Fuel				
Impact bonding of unbonded elements (11,853 ^a)				
Impact-bonded, inspected, and accepted ^b	0	11,107	0	0
Impact-bonded, inspected, and rejected	2	736	0	0
Total Elements Available for Subassembly				
Fabrication as of 7/15/70				
Cold-line fuel: Mark IA		323		
Mark II		223		
Vendor fuel: (Mark IA)		22,643 ^c		

^aThis is the total number of unbonded vendor fuel elements scheduled for impact bonding by ANL. Ten unbonded elements were set aside for historical samples; all the rest have been impact-bonded.

^bThirty "accept" impact-bonded elements were set aside for historical samples, and 10 additional "accepts" were decanned for metallographic examination.

^cDoes not include vendor elements impact-bonded by ANL. The 22,643 elements contain fuel cast and centrifugally bonded by the vendor. All were accepted by FCF verification inspection, but are not yet approved for general use in the reactor. They are being heat-treated to reclaim them (see Sect. I.D.1). Of the 473 elements heat-treated to date, 458 were accepted and are available for assembling in subassemblies.

TABLE I.E.2. Summary of FCF Fuel Handling

	FY 1970		FY 1971	
	6/16/70 through 6/30/70	Totals for FY 1970	7/1/70 through 7/15/70	Totals for FY 1971
<u>Subassembly Handling</u>				
Subassemblies Received from Reactor				
Driver fuel (all types)	0	141	6	6
Experimental	0	24	2	2
Other (blanket)	2	12	0	0
Subassemblies Dismantled for Surveillance, Examination, or Shipment to Experimenter				
Driver fuel	1	70	0	0
Experimental	0	24	1	1
Other (blanket)	1	6	0	0
Driver-fuel Elements to Surveillance	56	3454	0	0
Number from subassemblies	1	69	0	0
Subassemblies Transferred to Reactor				
Driver fuel				
From air cell	0	21	0	0
From cold line ^a	1	106	2	2
Experimental	0	16	0	0
<u>Fuel-alloy and Waste Shipments</u>				
Cans to Burial Ground	0	19	0	0
Skull Oxide and Glass Scrap to ICPP	0	5	0	0
Recoverable Fuel Alloy to ICPP				
Fuel elements ^b	1 (17.52 kg of alloy)	25 (433.86 kg of alloy)	1 (17.56 kg of alloy)	1 (17.56 kg of alloy)
Subassemblies ^b	6 (33.15 kg of alloy)	58 (301.55 kg of alloy)	3 (14.60 kg of alloy)	3 (14.60 kg of alloy)
Nonspecification material	0	0	0	0

^aCold-line subassemblies, following fabrication and final tests, are transferred either to the reactor or to the special-materials vaults for interim storage until needed for use in the reactor.

^bFigure outside parentheses is number of shipments made; figure inside is weight of alloy shipped.

PUBLICATIONS

Recent Developments in Fast Reactor Kinetics

D. K. Butler and D. A. Meneley

Nucl. Safety 11, 289-295 (July-August 1970)

Conceptual System Design Description for EBR-II Standby Heat Rejection System (SHEAR)

J. D. Cerchione, N. Bulut, M. W. Jackson, F. D. McGinnis, R. E. Rice,

C. C. Stone, D. J. Veith, and F. D. Wagner

ANL/EBR-022 (July 1970)

Compton Recoil Gamma-Ray Spectroscopy

Raymond Gold

Nucl. Instr. Methods 84, 173 (1970)

Materials-Coolant Interactions in EBR-II

W. E. Ruther, T. D. Claar, Sherman Greenberg, and R. V. Strain

ANL-7670 (March 1970)

Sodium Technology Quarterly Report, January, February, March 1970

ANL/ST-2

II. OTHER FAST REACTORS--OTHER FAST BREEDER REACTORS--FUEL DEVELOPMENT

A. Irradiation Effects, Mechanical Properties and Fabrication

1. Neutron Simulation Studies Using 4-MeV Dynamitron (A. Taylor)

Last Reported: ANL-7679, p. 107 (March 1970).

The Model 910 Physicon heavy-ion source has been tested on the ion-source test stand in the Physics Division. The parameters for operating the source on the Dynamitron have been investigated. Using the CCl_4 method* in conjunction with a nickel tube inserted in the arc chamber, low-divergence beams of nickel ion of $\sim 5 \mu\text{A}$ have been obtained. The nickel beam can be made approximately 20-fold greater than the Cl^+ beam from the dissociated support gas by adjusting the gas pressure in the source. The tests indicate that the Physicon source is compatible with the Dynamitron.

2. Mechanical Properties of Cladding Materials

a. Surface Defects as Failure Sites in AISI Type 304L Welded Stainless Steel Tubes (F. L. Yaggee)

Last Reported: ANL-7688, p. 155 (April-May 1970).

Artificially defected tubes of AISI Type 304L welded stainless steel (HT 840505) were used in these biaxial creep tests instead of the Type 304 stainless steel tubes previously used. Identical material (HT 850761) from the same commercial vendor has been used as cladding material for irradiation experiments in EBR-II.

Biaxial creep tests of Type 304L stainless steel tubes have been concluded, but similar tests have been initiated for AISI Type 316 seamless stainless steel tubes (PNL source material) in various cold-worked and annealed conditions. The biaxial creep results of annealed Type 304L stainless steel tubes at 650°C are summarized in Table II.A.1 and Figs. II.A.1-3.

(i) Stress, Strain, and Strain Rates of Pressurized Type 304L Welded Stainless Steel Tubes. In Table II.A.1, the applied hoop stress (σ_a) is that stress initially applied to the tube as a result of internal pressurization with

*Sidenius, G., and Skilbreid, O., Proc. Intl. Symp. on Electromagnetic Separation of Radioactive Isotopes, Vienna, May 1960, Springer-Verlag, Vienna, 1961, pp. 243-249.

helium gas. This stress will vary along the length of a specimen and between specimens pressurized simultaneously to the same pressure, as a result of variations in the wall thickness. The effective hoop stress (σ_{eff}) is derived from the applied hoop stress (σ_a) by invoking the Von Mises yield criterion.

TABLE II.A.1. Biaxial Creep Data for AISI Type 304L Welded Stainless Steel Tubes (HT 840505)
Tested at 650°C and Nominal Hoop Stresses of 7,500, 10,000, 15,000, and 20,000 psi^a

Applied Hoop Stress				Time to Start of $\dot{\epsilon}_m$, hr	Diametral Strain at Start of $\dot{\epsilon}_m$, %	Average Minimum Creep Rate ^b $\dot{\epsilon}_m$, in./in./hr	Time of Test, hr	Diametral Strain Range, %	Remarks
$\sigma_a = \frac{Pd}{2t}$		$\sigma_{\text{eff}} = 0.866 \sigma_a$							
psi	kgf-mm ⁻²	psi	kgf-mm ⁻²						
7,618-7,679	5.36-5.40	6,597-6,650	4.64-4.68	200	0.36-0.6	4.87×10^{-6}	1,000	0.64-1.11	No specimen failures.
10,066-10,143	7.08-7.13	8,717-8,784	6.13-6.18	200	0.58-0.86	1.42×10^{-5}	1,000	1.42-2.59	No specimen failures.
15,140-15,286	10.64-10.75	13,111-13,238	9.22-9.31	75	2-4	2.50×10^{-4}	217	3.38-13.8 ^c	Two specimens (3AD41 and 1AD90) failed by pinhole leak at weld-base-metal interface.
20,096-20,213	14.13-14.21	17,403-17,505	12.23-12.31	<10	<3	3.58×10^{-3}	18.8	3.2-22.8 ^c	One specimen (6AD41) failed by rupture.

^aData for 0.290-in.-OD by 0.250-in.-ID tubes in annealed condition.

^bAverage of measurements at five locations on each of six specimens tested simultaneously.

^cMaximum strain measured at pinhole failure or at area adjacent to failure by rupture.

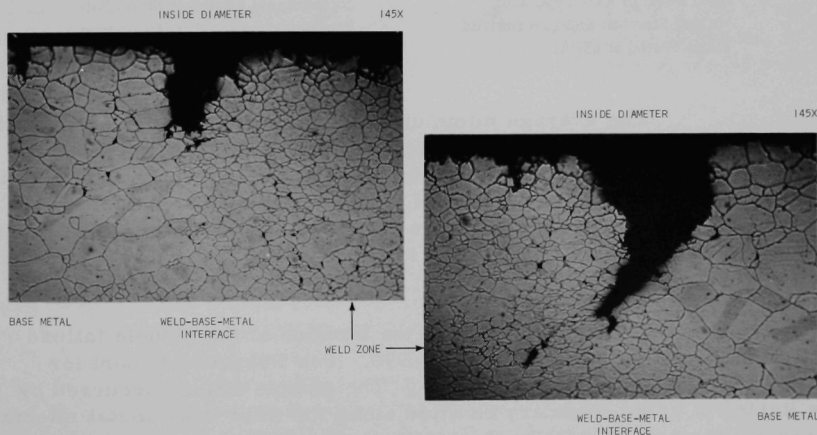


Fig. II.A.1. Location of Pinhole Failure at Weld-Base-metal Interface of an AISI Type 304L Welded Stainless Steel Tube (specimen 1AD90) Tested under Internal Pressure at 650°C and an Effective Hoop Stress of 13,111 psi (nominal hoop stress, 15,000 psi). Failure in 200 hr.

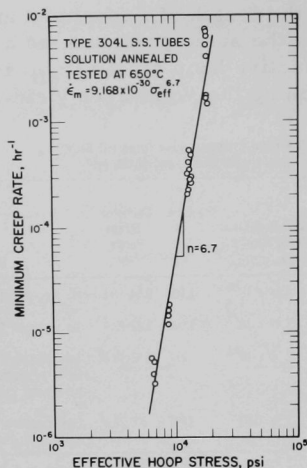


Fig. II.A.2

Minimum Creep Rate vs Effective Hoop Stress of AISI Type 304L Welded Stainless Steel Pressurized Tubes Tested at 650°C

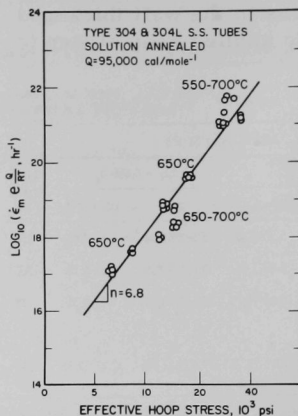


Fig. II.A.3

Zener-Hollomon Temperature-compensated Minimum Strain Rate Parameter vs Effective Hoop Stress of Solution-annealed AISI Type 304L Stainless Steel Pressurized Tubes

The average minimum creep rate ($\dot{\epsilon}_m$) is the average of strain rates measured at five locations on each of six specimens tested simultaneously. The diametral strain range is the minimum and maximum diametral strains ($\Delta D/D_0$) measured at five locations on each of six specimens. At applied hoop stresses of 15,000 and 20,000 psi, the maximum diametral strains correspond to the failure strains of the three specimens indicated.

Figure II.A.1 shows the location of the pinhole failure previously reported for specimen 1AD90. (See Progress Report for March 1970, ANL-7679, pp. 108-109.) The pinhole failure occurred by the linking of grain-boundary cavities along the weld-base-metal interface. A second specimen (3AD4I), which failed after 217 hr at a nominal applied hoop stress of 15,000 psi, also developed a pinhole leak at the weld-base-metal interface. Grain-boundary cavities in the weld zone and the base metal are clearly seen in Fig. II.A.1, both at triple points and at carbide precipitation sites along the grain boundaries. The diametral strain at the cross section of the tube is about 13.8%.

(ii) Stress and Temperature Dependence of the Minimum Strain Rate for Pressurized Types 304L and 304 Stainless Steel Tubes. Figure II.A.2 shows the stress dependence of the minimum strain rate ($\dot{\epsilon}_m$) at 650°C for annealed Type 304L welded stainless steel tubes

under biaxial stress. The stress dependence is 6.7, which yields the following expression for the minimum creep rate as a function of stress:

$$\dot{\epsilon}_m = 9.168 \times 10^{-30} \sigma_{\text{eff}}^{6.7}$$

Figure II.A.3 is a plot of the Zenor-Hollomon temperature-compensated, minimum strain-rate parameter versus effective hoop stress for annealed Types 304L and 304 stainless steel, assuming a 95,000 cal-mole⁻¹ activation energy for creep. This approach was taken because biaxial creep data for Type 304L stainless steel tubes were not obtained at a second temperature and at the same stresses. However, biaxial creep data were available for Types 304L and 304 stainless steel tubes at various hoop stresses and temperatures between 550 and 700°C. An activation energy of 95,000 cal-mole⁻¹ was reported by Cuddy* for Type 304 stainless steel, and by Davies *et al.*** for irradiated and unirradiated Type 304 stainless steel. The slope of the curve in Fig. II.A.3 is 6.8, which is in good agreement with the stress dependence indicated in Fig. II.A.2.

The internal surface of specimen 1AD90 showed intergranular radial cracks along the entire length of the specimen. The number and depth of penetration of these cracks ranged from a maximum at the cross section of the pinhole failure ($\Delta D/D_0 = 13.8\%$) to a minimum at the opposite end of the specimen where the measured diametral strain was approximately 5.8%.

b. Biaxial Creep of AISI Type 316 Seamless Stainless Steel Tubes (PNL Source Material) (F. L. Yaggee)

Not previously reported.

Tube specimens of AISI Type 316 seamless stainless steel are being prepared for biaxial creep tests in the temperature range 450-700°C and in the stress range 15,000-60,000 psi, with nominal tube dimensions 0.230-in.-OD by 0.200-in.-ID. The AISI Type 316 seamless stainless steel is the PNL source material purchased under a PNL Specification for Fuel Pin Cladding (Requisition B-58991, Revision 2, February 11, 1969). The initial biaxial creep test will be conducted in the temperature range 500-550°C and, tentatively, at nominal hoop stresses of 20,000, 30,000, 40,000, and 50,000 psi. Twenty-four specimens, in four bundles of six specimens each, will be tested for creep simultaneously in vacuum in a newly developed biaxial creep apparatus. The six specimens in each bundle will be connected to a common pressure source, and each bundle will contain

*Cuddy, L. J., Effects of Stress, Temperature and Structure on Creep of 304 Stainless, J. of Metals 19, 104 (Sept 1967).

**Davies, P. W., and Dutton, R., On the Mechanisms of Tertiary Creep in Face Centered Cubic Metals, Acta Met. 15, 1365-1372 (Aug 1967).

duplicate specimens of 20% cold-worked, 20% cold-worked and annealed, and 10% cold-worked material. Thus, from a single experiment, creep data will be generated for three material conditions at the same temperature and four widely different stresses.

The 20 and 10% cold-worked tubing has passed the prescribed NDT inspection (eddy current) for defects. The 4-in.-long specimens have been dimensionally inspected using precision air-gauging equipment. The following dimensional variations have been obtained from a few specimen lengths:

Material Condition	Diameter Variations, in.		Ovality, in.	Wall Thickness, in.
	ID	OD		
20% cold-worked	0.19976	0.23024	>0.0002	0.01524
	$\pm 5.2 \times 10^{-5}$	$\pm 2.76 \times 10^{-5}$		$\pm 7.7 \times 10^{-6}$
20% cold-worked and annealed	0.19951	0.23025	>0.0002	0.01537
	$\pm 9.06 \times 10^{-5}$	$\pm 4.57 \times 10^{-5}$		$\pm 1.57 \times 10^{-5}$
10% cold-worked	0.19947	0.22086	>0.0005	0.01519
	$\pm 2.18 \times 10^{-4}$	$\pm 7.26 \times 10^{-5}$		$\pm 1.63 \times 10^{-5}$

After the end closures are welded into the specimens, the test assemblies will be made.

III. GENERAL REACTOR TECHNOLOGY

A. Applied and Reactor Physics Development

1. Theoretical Reactor Physics--Research and Development

a. Theoretical Reactor Physics

(i) Neutronics Computational Capability

Not previously reported.

(a) Solution of the Neutron Diffusion Equation by Space-Energy Factorization (W. M. Stacey, Jr.)

An approximate method is proposed for solving a given outer iteration of the energy-dependent neutron-diffusion equation. The basis of the method is the factorization of the neutron flux into a purely energy-dependent term and a spatially dependent term with weak energy dependence

$$\phi(r, E) = \psi(r, E)\rho(E). \quad (1)$$

When Eq. 1 is substituted into the neutron-diffusion equation and the latter is integrated over space, the following equation for $\rho(E)$ is obtained:

$$\left[- \int dr \nabla \cdot D(r, E) \nabla \psi(r, E) + \int dr \Sigma(r, E) \psi(r, E) \right] \rho(E) = \int_E^\infty dE' \left[\int dr \Sigma_s(r, E' \rightarrow E) \psi(r, E') \right] \rho(E') + \chi(E). \quad (2)$$

Substitution of Eq. 1 into the neutron-diffusion equation followed by an integration over the energy interval $\Delta E_g = E_g - E_{g+1}$ and the approximation

$$\psi(r, E) = (1 - \theta) \psi_{g+1}(r) + \theta \psi_g(r), \quad E_g \geq E \geq E_{g+1} \quad (3)$$

results in the following equation for $\psi_{g+1}(r)$:

$$\begin{aligned} (1 - \theta) \left\{ - \nabla \cdot \left[\int_{\Delta E_g} dE \rho(E) D(r, E) \right] \nabla + \int_{\Delta E_g} dE \rho(E) \Sigma(r, E) - \int_{\Delta E_g} dE \int_{\Delta E_g} dE' \rho(E') \Sigma_s(r, E' \rightarrow E) \right\} \psi_{g+1}(r) \\ = \theta \left\{ \nabla \cdot \left[\int_{\Delta E_g} dE \rho(E) D(r, E) \right] \nabla - \int_{\Delta E_g} dE \rho(E) \Sigma(r, E) + \int_{\Delta E_g} dE \int_{\Delta E_g} dE' \rho(E') \Sigma_s(r, E' \rightarrow E) \right\} \psi_g(r) \\ + \frac{S(r)}{\lambda} \int_{\Delta E_g} dE \chi(E) + \sum_{g' < g} \int_{\Delta E_g} dE \int_{\Delta E_{g'}} dE' \rho(E') \Sigma_s(r, E' \rightarrow E) \left\{ (1 - \theta) \psi_{g'+1}(r) + \theta \psi_{g'}(r) \right\}. \quad (4) \end{aligned}$$

When $\theta = 1$, Eq. 4 is the conventional multigroup diffusion equation. $S(r)$ and λ are the fission source and eigenvalue computed on the previous outer iteration.

Equations 2 and 4 are solved iteratively:

- (1) ψ_1 is obtained by solving the first fine-group equation.
- (2) $\rho(E)$ is obtained as the solution of a fine-group calculation with many groups in the interval $E_1 > E > E_2$, with $\theta = 1$.
- (3) ψ_2 is obtained by solving Eq. 4.
- (4) Steps 2 and 3 are repeated a specified number of times, with θ set to a specified value.
- (5) Steps 2-4 are repeated for the second interval $E_2 > E > E_3$, and subsequent intervals.

Thus, the energy range is divided into a number of broad intervals ΔE_g . Within each of these, the spatial flux shape is assumed to be given by Eq. 3 for the purpose of weighting group constants for a fine-group spectrum calculation of $\rho(E)$, $E_g > E > E_{g+1}$. Once an initial estimate of $\rho(E)$, $E_g > E > E_{g+1}$ is obtained, the spatial shape used in this interval is improved and $\rho(E)$ is recalculated. This is repeated for subsequent intervals.

In essence, the method couples a fine-group fundamental-mode type calculation (for ρ) with a broad-group spatially dependent calculation (for ψ). On physical grounds, the method should be effective when the spatial dependence of the neutron flux does not vary rapidly with energy. In the limit that the ψ are calculated with the same group structure as ρ is, the method reduces to the standard multigroup diffusion equations with $\theta = 1$.

The method has been successfully tested on several 1D models representative of fast breeder reactors with several core zones, blankets, and reflectors. For one representative calculation, space-energy factorization with eight, four, and two broad energy intervals agreed with a direct 24-group solution to within 0.12, 0.26, and 0.79% Δk , respectively. Similar agreement was obtained in the other calculations. Flux spectra constructed from Eq. 1 agreed closely with direct solutions, except in regions of low importance.

Space-energy factorization has potential application in ultrafine-group (~ 2000) spatially dependent calculations, where an approximate method of treating spatial dependence is currently being sought, or in fine-group (20-100) calculations, where it could be used as an approximate method or to accelerate the convergence of the exact solution.

(b) Anisotropic Elastic Moderation of Neutrons
(W. M. Stacey, Jr.)

The energy lost by a neutron in an elastic collision with an atomic nucleus is correlated with the scattering angle by the laws of classical mechanics. Any angular bias in the neutron-scattering properties of an isotope is thus reflected in the parameters characterizing the moderation of neutrons by that isotope.

Continuous slowing-down theory provides a convenient representation in which to study the effect of scattering anisotropy upon the elastic moderation of neutrons. The Greuling-Goertzel (G-G) approximation* has been extended to include anisotropic CM scattering for a mixture of isotopes, with the moderating parameters expressed in terms of the moments of the scattering transference function $T_{\ell\ell}^n$, discussed by Hurwitz and Zweifel.** This approximation reduces to the results obtained in a different manner by Amster† for a single isotope. The improved G-G approximation introduced by Stacey†† has also been extended‡ to include anisotropic CM scattering.

The zeroth (ξ^i) and first (a^i) moments of the slowing-down kernel for isotope i , which define the moderating parameters of the G-G approximation, are

$$\xi^i = - \sum_{\ell'=0} \frac{\sigma_1^{\ell'}}{\sigma_1^0} T_{0\ell',i}^1, \quad a^i = \sum_{\ell'=0} \frac{\sigma_1^{\ell'}}{\sigma_1^0} T_{0\ell',i}^2, \quad (1)$$

where $\sigma_1^{\ell'}$ is the ℓ' th Legendre moment of the CM scattering cross section of isotope i . The G-G moderating parameters for a mixture are constructed from

$$\xi = \sum_i \Sigma_{si} \xi^i / \sum_i \Sigma_{si}, \quad \gamma = \sum_i \Sigma_{si} a^i / \sum_i \Sigma_{si} \xi^i, \quad (2)$$

where Σ_{si} is the macroscopic total scattering cross section of isotope i .

*Goertzel, G., and Greuling, E., An Approximate Method for Treating Neutron Slowing Down, Nucl. Sci. Eng. **7**, 69 (1960).

Zweifel, P. F., and Hurwitz, H., Jr., Transformation of Scattering Cross Sections, J. Appl. Phys. **25, 1241 (1954). Hurwitz, H., Jr., and Zweifel, P. F., Slowing Down of Neutrons by Hydrogenous Moderators, J. Appl. Phys. **26**, 923 (1955).

†Amster, H. J., Heavy Moderator Approximations in Neutron Transport Theory, J. Appl. Phys. **29**, 623 (1958).

††Stacey, W. M., Jr., Continuous Slowing Down Theory Applied to Fast-Reactor Assemblies, Nucl. Sci. Eng., to be published.

‡Stacey, W. M., Jr., Continuous Slowing Down Theory for Anisotropic Elastic Neutron Moderation in the P_N and B_N Representations, Nucl. Sci. Eng., to be published.

Making use of the heavy mass expansion for the $T_{\ell\ell}^n$ given by Amster,* the isotopic parameters of Eqs. 1 may be written

$$\xi^i = A_1^i \left(\frac{\sigma_1^1}{\sigma_1^0} \right) (1 - \alpha_i) + A_2^i \left(\frac{\sigma_1^1}{\sigma_1^0}, \frac{\sigma_1^2}{\sigma_1^0} \right) (1 - \alpha_i)^2 + \dots \\ + A_n^i \left(\frac{\sigma_1^1}{\sigma_1^0}, \dots, \frac{\sigma_1^n}{\sigma_1^0} \right) (1 - \alpha_i)^n + \dots, \quad (3)$$

$$a^i = B_2^i \left(\frac{\sigma_1^1}{\sigma_1^0}, \frac{\sigma_1^2}{\sigma_1^0} \right) (1 - \alpha_i)^2 + \dots + B_n^i \left(\frac{\sigma_1^1}{\sigma_1^0}, \dots, \frac{\sigma_1^n}{\sigma_1^0} \right) (1 - \alpha_i) + \dots, \quad (4)$$

where A_n^i and B_n^i are functions of the indicated arguments and

$$\alpha_i = \left(\frac{M_i - 1}{M_i + 1} \right)^2.$$

The moderating parameters of the improved G-G approximation have the same functional dependence upon the atomic mass and scattering moments.

Because $1 - \alpha_i \approx 0.01$ for heavy elements and ≈ 0.1 for light and intermediate elements, the moderating parameters ξ and γ depend primarily upon the $\ell = 0, 1$ and $\ell = 0, 1, 2$ scattering moments, respectively. Thus, retention of the first few scattering moments suffices in evaluating the moderating parameters. This is in sharp contrast to the multigroup treatment of elastic moderation wherein many higher-order scattering moments must be retained to evaluate ultrafine-group scattering matrices.

A series of calculations has been performed for mixtures typical of fast breeder reactors, using ENDF/B angular scattering data. Isotopic and mixture-composite moderating parameters have been examined as a function of energy and the number of scattering moments retained. The moderating parameters ξ and γ differ considerably from the parameters for isotropic scattering and vary dramatically with energy. Anisotropy is predominantly forward, which reduces the moderating parameters relative to their isotropic values, but at some energies is predominantly backward, which increases the moderating parameters. This is illustrated in Fig. III.A.1 by ξ and γ for oxygen, which vary considerably about their isotropic values of 0.1194 and 0.0816, respectively.

These rapid variations in the moderating parameters with energy produce sharp fluctuations in the flux, in much the same manner as a scattering resonance would. The moderating parameters of the improved

*Amster, op. cit.

G-G approximation, in which the scattering properties are averaged over the scattering interval

$$u > u' > u - 2 \ln \frac{M_i + 1}{M_i - 1},$$

exhibit less rapid fluctuation than is found in the G-G parameters. Anisotropy affects the competition between scattering and absorption, and thus affects the slowing-down density.

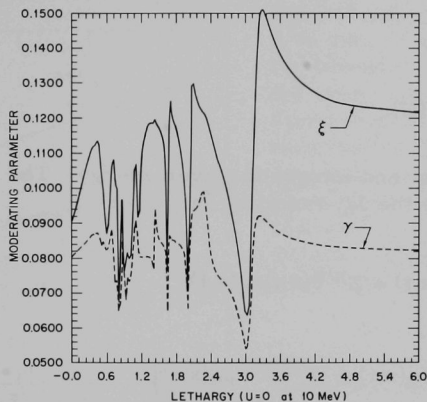


Fig. III.A.1
Moderating Parameters for ^{16}O

(c) Studies of Spectral Synthesis in Spatially Dependent Fast-reactor Dynamics (W. M. Stacey, Jr.)

The idea of calculating the neutron-flux spectrum by combining known trial spectra was introduced* to compute spatially dependent thermal spectra. This idea was subsequently applied to calculate spatially dependent spectra in fast reactors.** The theory for combining trial spectra to compute space- and time-dependent spectra has been developed† and has subsequently been applied†† to compute time-dependent

*Calame, G. P., and Federighi, F. D., A Variational Procedure for Determining Spatially Dependent Thermal Spectra, Nucl. Sci. Eng. 10, 190 (1961).

**Storrer, F., and Chaumont, J. M., "The Application of Space-Energy Synthesis to the Interpretation of Fast Multizone Critical Experiments," in Proc. Intern. Conf. Fast Critical Experiments and Analysis, ANL-7320 (1967). Stacey, W. M., Jr., Modal Approximations: Theory and an Application to Reactor Physics, MIT Press, Cambridge, Massachusetts (1967); also Fast Reactor Computational Models, Nucl. Sci. Eng. 28, 443 (1967).

†Henry, A. F., Few-Group Approximations Based on a Variational Principle, Nucl. Sci. Eng. 27, 493 (1967). Stacey, W. M., Jr., General Multigroup and Spectral Synthesis Equations, Nucl. Sci. Eng. 40, 73 (1970).

††Stacey, W. M., Jr., Spectral Synthesis Applied to Fast-Reactor Dynamics, to be published in Nucl. Sci. Eng. 41 (1970); also "Spectral Synthesis Methods in Fast-Reactor Dynamics," Symp. Dynamics of Nuclear Systems, Tucson (1970).

spectra in a uniform fast reactor. Several calculations of space- and time-dependent spectra in multiregion fast-reactor models have recently been performed.

Spectral synthesis equations were derived by substituting expansions for the flux and current in known trial spectra ψ_n and ρ_n ,

$$\phi(x, E, t) = \sum_{n=1}^N \phi_n(x, t) \psi_n(E), \quad (1)$$

and

$$J(x, E, t) = \sum_{n=1}^N J_n(x, t) \rho_n(E), \quad (2)$$

into the P_1 equations, weighting, and integrating over energy. The equations are then combined to eliminate the J_n , resulting in

$$\begin{aligned} \sum_{n=1}^N \left[-\nabla \cdot D^{n'n}(x, t) \nabla \phi_n(x, t) + \Sigma^{n'n}(x, t) \phi_n(x, t) \right. \\ \left. - (1 - \beta) \chi^{n'} F^n(x, t) \phi_n(x, t) + (1/v)^{n'n} \dot{\phi}_n(x, t) \right] \\ - \sum_{m=1}^M \lambda_m \chi_m^{n'} C_m(x, t) = 0, \quad n' = 1, \dots, N. \end{aligned} \quad (3)$$

These equations have the same generic form as the multigroup diffusion equations, with the important exception that for the latter $D^{n'n} = D^{nn} \delta_{n'n}$ and $\Sigma^{n'n} = 0$, $n' < n$, for no upscatter. The associated precursor equations are

$$\beta_m \sum_{n=1}^N F^n(x, t) \phi_n(x, t) - \lambda_m C_m(x, t) = \dot{C}_m(x, t), \quad m = 1, \dots, M. \quad (4)$$

The coefficients in Eqs. 3 and 4 are integrals of cross sections or fission spectra with weighting function n' and/or trial spectrum n , taken over all energy.

The RAUMZEIT code* has been modified to solve Eqs. 3 and 4. [The modification consisted of generalization of the code to accept $(1/v)^{n'n} n' \neq n$.] Several transients in which spatial and spectral

*Adams, C. H., and Stacey, W. M., Jr., RAUMZEIT--A Program to Solve Coupled Time Dependent Neutron Diffusion Equations in One Space Dimension, KAPL-M-6728 (1967).

shifts were important have been calculated for multiregion fast-reactor models. The trial and weighting functions were 26-group fluxes and adjoints. For comparison, the transients were also calculated with the QX1 code, which solves the 1D multigroup kinetics equations by the improved quasi-static method.*

One of these transients was based on a uniform slab core 350 cm thick with a 50-cm blanket on each end. The transient was initiated by linearly decreasing the boron concentration in the right 150 cm of the core, and simultaneously increasing the boron concentration in the

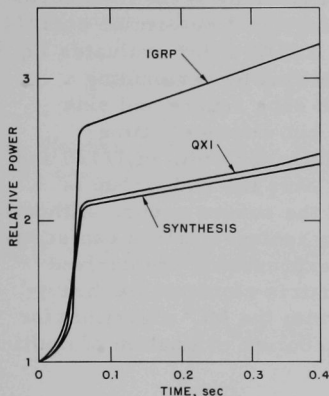


Fig. III.A.2. Asymmetric Perturbation in Slab Reactor Model

left 150 cm of the core at the same rate, for 0.06 sec. Two trial spectra were taken as fundamental-mode spectra corresponding to the core composition, but with more or less boron than was in the core initially or at any time during the transient. A third trial spectrum was a fundamental-mode spectrum characteristic of the blanket with a source characteristic of the core fundamental-mode current. Weighting functions were adjoints for the same conditions.

The total power predicted by the spectral synthesis calculation is in good agreement with the QX1 result, as shown in Fig. III.A.2. For comparison, a one-group spatially dependent calculation, with constants collapsed over the initial core spectrum, is shown to illustrate the importance of spectral shifts upon the calculation. A measure of the importance of spatial plus spectral effects is provided by the fact that the point-kinetics solution for this transient is a constant power.

In general, spectral synthesis provides an effective and relatively simple model for treating spectral shifts in fast-reactor transient calculations.

(ii) Reactor Computations and Code Development

Last Reported: ANL-7705, pp. 133-138 (June 1970).

(a) Semianalytic Expressions for Evaluating Scattering Matrix Elements (B. J. Toppel and H. Henryson)

An approximate method for calculating heavy-element elastic scattering transfer matrices for use in multigroup reactor codes

*Ott, K. O., and Meneley, D. A., Accuracy of the Quasistatic Treatment of Spatial Reactor Kinetics, Nucl. Sci. Eng. 36, 402 (1969).

has been developed. Several computer codes*,** are available to numerically approximate the defining equation

$$\sigma_s^{\ell}(j \rightarrow k) = \frac{2\ell + 1}{1 - \alpha} \frac{\int_j du \int_k du' \sigma_s(u) P_{\ell}(\mu_L(u \rightarrow u')) \phi_{\ell}(u) e^{-(u' - u)} \sum_{n=0}^N (2n + 1) f_n(u) P_n(\mu_c(u \rightarrow u'))}{\int_j du \phi_{\ell}(u)} \quad (1)$$

All terms in Eq. 1 have their standard meanings, and the integration limits of the source (j) and sink (k) groups, which depend on the group lethargy widths and the mass of the scatterer, have been given by several authors.* The numerical approximations made in evaluating Eq. 1 determine both the speed and accuracy of the calculation. The ETOG code* evaluates Eq. 1 with group-lethargy widths of 1/4 and a constant flux by performing a Simpson's-s-rule integration using 60 intervals in each source and sink integral. This calculation is essentially exact, but extremely time-consuming. In the MC² code,** using a group-lethargy width of 1/120 and constant flux, an analytical integration of Eq. 1 over the sink group is coupled with a simple average over the ends of the source group. Although quite fast, this method is not accurate for heavy isotopes, which can scatter only a few groups. In this work, semianalytic expressions are derived which may be used to evaluate the scattering matrix elements for heavy-element scattering. When used in conjunction with the MC² algorithm for light elements, this method provides fast and accurate evaluation of multi-group elastic scattering matrices.

Let the notation $\langle \rangle$ designate a suitable average over the source group, so that Eq. 1 may be written

$$\sigma_s^{\ell}(j \rightarrow k) = \frac{\sum_{n=0}^N \langle \sigma_n(u) \phi_{\ell}(u) \rangle_j A_n^{\ell}(j \rightarrow k)}{\Delta u \langle \phi_{\ell}(u) \rangle_j} \quad (2)$$

and

$$A_n^{\ell}(j \rightarrow k) \equiv (2\ell + 1) \frac{2n + 1}{1 - \alpha} \int_j du \int_k du' P_{\ell}(\mu_L) P_n(\mu_c) e^{-(u' - u)}, \quad (3)$$

where

$\Delta u \equiv$ group lethargy width,

$\alpha \equiv (A - 1)^2 / (A + 1)^2$,

*Kusner, D. E., Dannels, R. A., and Kellman, S., ETOG-1, A FORTRAN IV Program to Process Data from the ENDF/B File to the MUFT, GAM and ANISN Formats, WCAP3845-1 (ENDF 114) (Dec 1969).

**Toppel, B. J., Rago, A. L., and O'Shea, D. M., MC²--A Code to Calculate Multigroup Cross Sections, ANL-7318 (June 1967).

and

$$\sigma_n(u) \equiv \sigma_s(u)f_n(u).$$

The matrix elements $A_n^\ell(j \rightarrow k)$ may be related to a function similar to the T function investigated by Amster*

$$T_{\ell n}^m = \frac{(-)^m}{m!} \frac{2n+1}{2} \int_0^{\ell n(1/\alpha)} dU U^m P_\ell(\mu_L(U)) P_n(\mu_c(U)) \left(-\frac{d\mu_c}{dU} \right). \quad (4)$$

As an example of the derivation, consider the element $A_n^\ell(j \rightarrow j+3)$ if the group width and scattering mass are related through the inequality

$$\frac{1}{3} \ell n(1/\alpha) \leq \Delta u < \frac{1}{2} \ell n(1/\alpha), \quad (5)$$

so that the element may scatter a neutron through three energy groups. In this case, Eq. 3 has the form

$$A_n^\ell(j \rightarrow j+3) = (2\ell+1) \frac{2n+1}{2} \int_{u_{j+2}-\ell n(1/\alpha)}^{u_j} du \int_{u_{j+2}}^{u+\ell n(1/\alpha)} du' P_\ell(\mu_L) P_n(\mu_c) \frac{2e^{-(u'-u)}}{1-\alpha}. \quad (6)$$

Changing variables to $U = u' - u$ and reversing the order of integration, we have

$$\begin{aligned} A_n^\ell(j \rightarrow j+3) &= (2\ell+1) \frac{2n+1}{2} \int_{u_{j+2}-\ell n(1/\alpha)}^{u_j} du \int_{u_{j+2}-u}^{u_j} dU \\ &\quad P_\ell(\mu_L) P_n(\mu_c) \left(-\frac{d\mu_c}{dU} \right) \\ &= (2\ell+1) \frac{2n+1}{2} \int_{2\Delta u}^{\ell n(1/\alpha)} dU \int_{u_{j+2}-U}^{u_j} du P_\ell(\mu_L) P_n(\mu_c) \left(-\frac{d\mu_c}{dU} \right) \end{aligned} \quad (7)$$

and performing the inner integral, we have

$$\begin{aligned} A_n^\ell(j \rightarrow j+3) &= (2\ell+1) \{ 2\Delta u [\bar{T}_{\ell n}^0(\alpha, 2\Delta u) - \bar{T}_{\ell n}^0(\alpha, \ell n(1/\alpha))] \\ &\quad + [\bar{T}_{\ell n}^1(\alpha, 2\Delta u) - \bar{T}_{\ell n}^1(\alpha, \ell n(1/\alpha))] \}, \end{aligned} \quad (8)$$

*Amster, H., Heavy Moderator Approximations in Neutron Transport Theory, J. Appl. Phys. 29, 4, 623-627 (April 1958).

where

$$\bar{T}_{\ell n}^m(\alpha, \beta) \equiv \frac{(-)^m}{m!} \frac{2n+1}{2} \int_0^\beta dU U^m P_\ell(\mu_L) P_n(\mu_C) \left(-\frac{d\mu_C}{dU} \right). \quad (9)$$

From Eqs. 4 and 9,

$$\bar{T}_{\ell n}^m(\alpha, \ell n(1/\alpha)) = T_{\ell n}^m(\alpha)$$

Table III.A.1 presents expressions for the matrix elements $A_n^\ell(j \rightarrow k)$ for several group width-mass relations. Note that Eq. 5 is applicable to all elements of mass $A > 181$ for the MC² group width $\Delta u = 1/120$.

TABLE III.A.1. Heavy Mass Matrix Elements $A_n^\ell(j \rightarrow k)$

k	Group Width/Mass, $q \equiv \ell n(1/\alpha)$	$\frac{1}{2\ell+1} A_n^\ell(j \rightarrow k)$
<u>$\frac{1}{3}q \leq \Delta u < \frac{1}{2}q$</u>		
j		$\Delta u \bar{T}_{\ell n}^0(\alpha, \Delta u) + \bar{T}_{\ell n}^1(\alpha, \Delta u)$
j + 1		$2\Delta u [\bar{T}_{\ell n}^0(\alpha, 2\Delta u) - \bar{T}_{\ell n}^0(\alpha, \Delta u)] + \bar{T}_{\ell n}^1(\alpha, 2\Delta u) - 2\bar{T}_{\ell n}^1(\alpha, \Delta u)$
j + 2		$3\Delta u \bar{T}_{\ell n}^0(\alpha) + \bar{T}_{\ell n}^1(\alpha) - 2\bar{T}_{\ell n}^1(\alpha, 2\Delta u) + \bar{T}_{\ell n}^1(\alpha, \Delta u) -$ $\Delta u [4\bar{T}_{\ell n}^0(\alpha, 2\Delta u) - \bar{T}_{\ell n}^0(\alpha, \Delta u)]$
j + 3		$-2\Delta u \bar{T}_{\ell n}^0(\alpha) - \bar{T}_{\ell n}^1(\alpha) + 2\Delta u \bar{T}_{\ell n}^0(\alpha, 2\Delta u) + \bar{T}_{\ell n}^1(\alpha, 2\Delta u)$
<u>$\frac{1}{2}q \leq \Delta u < q$</u>		
j		$\Delta u \bar{T}_{\ell n}^0(\alpha, \Delta u) + \bar{T}_{\ell n}^1(\alpha, \Delta u)$
j + 1		$2\Delta u \bar{T}_{\ell n}^0(\alpha) + \bar{T}_{\ell n}^1(\alpha) - 2\Delta u \bar{T}_{\ell n}^0(\alpha, \Delta u) - 2\bar{T}_{\ell n}^1(\alpha, \Delta u)$
j + 2		$-\bar{T}_{\ell n}^1(\alpha) - \Delta u \bar{T}_{\ell n}^0(\alpha) + \Delta u \bar{T}_{\ell n}^0(\alpha, \Delta u) + \bar{T}_{\ell n}^1(\alpha, \Delta u)$
<u>$\Delta u \geq q$</u>		
j		$\Delta u \bar{T}_{\ell n}^0(\alpha) + \bar{T}_{\ell n}^1(\alpha)$
j + 1		$-\bar{T}_{\ell n}^1(\alpha)$

Although the function $\bar{T}_{\ell n}^m$ does not in general satisfy a heavy mass expansion, since it need be calculated only once for a given A and Δu , it may be calculated directly from a high-order quadrature of Eq. 9. Table III.A.2 compares the results of calculations using Eq. 2 and the matrix elements of Table III.A.1 with ETOG and MC² results. Once the matrix elements $A_n^\ell(j \rightarrow k)$ have been calculated, the calculation using Eq. 2 is significantly faster than a numerical integration of Eq. 1.

TABLE III.A.2. ^{239}Pu Elastic Scattering Matrix Elements

$$(\Delta u = 1/120)$$

$$(E_j = 6.116 \text{ MeV})$$

Method/k	$(\sigma_s^0/\sigma_s^1)_{j \rightarrow k}$			
	j	j + 1	j + 2	j + 3
ETOG	3.49/9.64	0.724/0.750	0.126/-0.240	$0.449 \times 10^{-4}/-0.134 \times 10^{-3}$
This work	3.52/9.72	0.714/0.733	0.127/-0.239	$0.624 \times 10^{-4}/-0.179 \times 10^{-3}$
MC ² *	3.14/7.02	2.44/4.38	0.228/-0.370	$0.598 \times 10^{-4}/-0.177 \times 10^{-3}$

*The MC² calculations used a hyperfine-group lethargy width of 1/240 and a corrected $\sigma_{j \rightarrow j+3}$ [averaged over ($u_{j+2} - q, u_j$), rather than the whole source group].

(b) One-dimensional Transport Calculations in the ARC System (B. J. Toppel and H. Henryson)

User testing of the ARC system standard path STP002, one-dimensional transport theory, has indicated two bugs leading to errors in the calculation of Σ_t , the macroscopic total cross section. Since the only neutronics module in the ARC system presently using Σ_t is SNARC in the anisotropic option, the bugs had no effect on the vast majority of problems run using the ARC system.

In the creation of an XS.ISO data set, MC² provided a default value of zero for the P_0 component of the self-scatter cross section σ_{aniso} for all materials not given a correct Legendre elastic scattering treatment. Although this default did not affect the neutron-balance (P_0) equation, it would affect the transport calculation by dint of its effect on the P_1 equation. The default has been changed in the production version of MC² to give $\sigma_{\text{aniso}} = \sigma_{\text{el}}^0(j \rightarrow j)$ and consequently, $\sigma_t = \sigma_{\text{tr}}$. A second bug was found in the homogenization module NUC001 (HOMOG). An indexing error occurred in the calculation of $\Sigma_t(j)$ if the composition in question had down-scatter from group j . These two errors led to differences of ~5% in k_{eff} in calculations of ZPR-6 Assembly 6 using the isotropic and anisotropic options of SNARC. After the HOMOG bug was corrected and module NUI006 was used to create a corrected version of XS.ISO, the isotropic and anisotropic eigenvalues differed by only 0.03%.

(c) Modifications Made to the Variably Dimensioned MC² Capability in the ARC System (C. G. Stenberg and B. J. Toppel)

There have been one correction and four modifications to the variably dimensioned MC² capability in the ARC system.

A correction was made to properly handle the thermal broad-group cross sections when these are added to the XS.ISO microscopic

multigroup cross section, data set. Before this correction was made the thermal broad-group cross sections were not properly added to the XS.ISO data set. The error occurred if and only if the user was selective in choosing to add only some of the isotopes from the total number in the problem.

The elastic self-scattering cross section for the thermal broad-energy group, $\sigma_{el \rightarrow j}$, has been modified from a value of zero to the value

$$\sigma_{el \rightarrow j} = \sigma_{trj} - \sigma_{cj} - \sigma_{fj} - \sigma_{n\alpha j} - \sigma_{npj},$$

where

σ_{trj} is the thermal transport cross section,

σ_{cj} is the thermal capture cross section,

σ_{fj} is the thermal fission cross section,

$\sigma_{n\alpha j}$ is the thermal n- α cross section,

and

σ_{npj} is the thermal n-p cross section.

As before this modification, if the thermal energy-group transport, capture, fission, n- α , and n-p cross sections are not input by the user, then the cross sections assigned to the thermal broad-energy group are the respective values calculated in the lowest-energy epithermal broad-energy group.

The anisotropic self-scattering cross section has been modified for an MC² problem run with the anisotropic neutronics option and a non-Legendre treatment for the isotope. For this case, each anisotropic self-scattering cross section has been modified so that it no longer has a value equal to zero for each epithermal broad-energy group, but has the value corresponding to that of the elastic self-scattering cross section for each broad-energy group. As was true before this modification, the thermal anisotropic self-scattering cross section is set equal to the thermal transport cross section.

Two modifications have been made in the epithermal cross-section module CSI001. For an ultrafine-group problem, the maximum problem energy (EMAX) may not lie below the top of the Legendre-coefficient data library (10 MeV in the present library). A consistency check of the user input data is made to ensure that EMAX is at least 10 MeV for an ultrafine problem, and if not the problem is terminated with an appropriate error message. A further check is made by this module when EMAX is greater than 10 MeV for an ultrafine-group problem. The value of EMAX is adjusted so that a fine (and hence an ultrafine) group boundary will occur

at exactly 10 MeV. This requirement is necessary due to the present internal structure of the code in the area in which the transfer and utilization of the Legendre-coefficient data are used.

(d) Calculation of Elastic Scattering Matrices for MC²-2
(B. J. Toppel and C. G. Stenberg)

In the MC² code,* ultrafine-group ($\Delta u = 1/120$) elastic scattering matrices are generated for materials whose elastic scattering angular dependence has been represented by a Legendre polynomial expansion. In particular, let the elastic scattering angular dependence for the material m at a neutron energy E_j be represented in the center of mass as

$$\sigma_s^m(\omega', E_j) = \sum_{\ell} B_{\ell j}^m P_{\ell}(\mu'), \quad (1)$$

where

$$\sigma_s^m(\omega', E_j) = \text{the material } m \text{ cross section for scattering into the solid angle } d\omega' \text{ in the center of mass,}$$

$$\mu' = \text{the cosine of the scattering angle in the center of mass,}$$

and

$$P_{\ell} = \text{the } \ell\text{th Legendre polynomial.}$$

The $B_{\ell j}^m$ are related to the customarily reported Legendre expansion coefficients $f_{\ell j}^m$ of the angular distribution of scattering in the center of mass by the expression

$$4\pi B_{\ell j}^m = (2\ell + 1) \sigma_s^m f_{\ell j}^m. \quad (2)$$

If we relate the initial and final energies in the laboratory system, E_j and E , respectively, to the center-of-mass scattering angle, and integrate over the azimuth angle, we obtain

$$\sigma_s^m(E_j \rightarrow E) dE = \frac{4\pi}{\alpha^m E_j} dE \sum_{\ell} B_{\ell j}^m P_{\ell}(\mu'), \quad (3)$$

where α^m , for the mass A^m of nucleus m , is given by

*Toppel, B. J., Rago, A. L., and O'Shea, D. M., MC², A Code to Calculate Multigroup Cross Sections, ANL-7318 (June 1967).

$$\alpha^m = \frac{4A^m}{(A^m + 1)^2} \quad (4)$$

and relates the minimum energy, E_{\min}^m , to the initial energy by

$$E_{\min}^m = (1 - \alpha^m) E_j. \quad (5)$$

The elastic transfer cross section from initial energy E_j into group k , $\sigma_s^m(E_j \rightarrow k)$, may be obtained by relating μ' with E_j , E , and A^m , and then integrating Eq. 3 over final energy E ranging from E_k to E_{k-1} , the lower and upper energy limits, respectively, of group k .

The elastic transfer from group j to group k is obtained by averaging the corresponding $\sigma_s^m(E \rightarrow k)$ with E at each end of group j . Thus,

$$\sigma_{elj \rightarrow k}^m = \frac{\sigma_s^m(E_j \rightarrow k) + \sigma_s^m(E_{j-1} \rightarrow k)}{2}. \quad (6)$$

The use of Eq. 6 tacitly assumes that the $\sigma_s^m(E \rightarrow k)$ varies linearly across the source group j . This assumption is clearly not correct for all receptor groups k and for all degrees of anisotropy.

To provide a more rigorous treatment for the new code, MC²-2, we are studying the problem of calculating elastic scattering

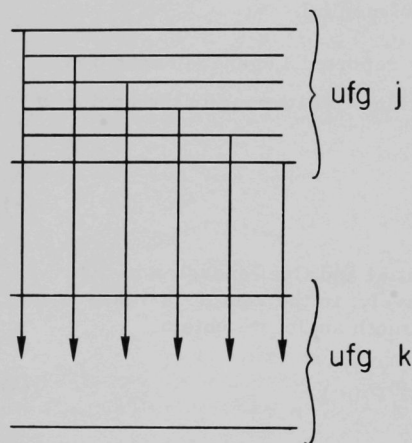


Fig. III.A.3. Scattering from Hyperfine Groups within Ultrafine Group j into Ultrafine Group k

matrices with particular emphasis on replacing the simple approach given in Eq. 6 while at the same time minimizing running time.

The general approach outlined above is being followed, but the $\sigma_s^m(E_j \rightarrow k)$ are being evaluated at hyperfine-group (hfg) intervals within the ultrafine-group (ufg) j , and then $\sigma_{elj \rightarrow k}^m$ is obtained by a trapezoidal integration over the hyperfine groups contained within the source ufg j . Figure III.A.3 schematically indicates the method used. The accuracy of the method has been tested using the ETOG code,* which uses a very fine-mesh Simpson's-rule integration over the source and receptor groups and may be considered to be exact.

*Kusner, D. E., and Dannels, R. A., ETOG-1, A FORTRAN IV Program to Process Data from the ENDF/B File to the MUFT, GAM, and ANISN Formats, WCAP-3845-1, ENDF 114 (Dec 1969).

Results are being obtained for various masses and at various energies to display the influences of anisotropy and mass on the kinematics of the scattering. The main parameter of interest is the number of hfg's per ufg. In the original MC² code, there is one hfg per ufg.

By way of example of the variation of the scattering probability across the source group, Figs. III.A.4-III.A.9 show scattering from the top of various hfg's i within a given ufg, to various ufg's $j + n$. The top of hfg 1 corresponds to the upper energy boundary of the ufg. Two source groups j have been selected for sodium, iron, and ²³⁹Pu to indicate the effect of anisotropy. The straight dashed lines indicate the assumed shape using Eq. 6. The existing MC² algorithm becomes progressively worse as the mass number increases and as the scattering exhibits more anisotropy at the higher energies. In all cases, scattering to the lowest ufg exhibits the most radical errors, since not all portions of the source groups can scatter to the lowest ufg. The error in the present MC² algorithm is represented by the difference in the area under the solid and dashed lines for a given group, assuming the solid line results involving 20 hfg/ufg represent the correct answer.

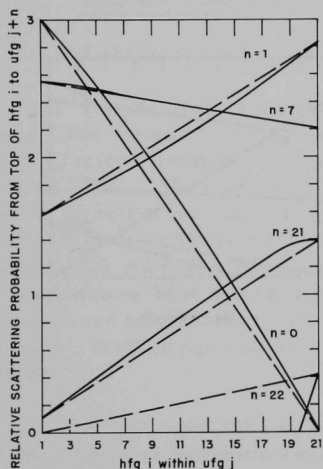


Fig. III.A.4. Sodium: Source (ufg j) Energy Limits of 6.116-6.065 MeV (maximum of 22 ufg's scattered)

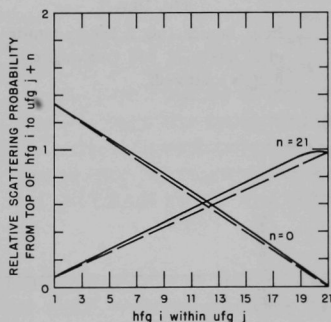


Fig. III.A.5. Sodium: Source (ufg j) Energy Limits of 0.502-0.498 MeV (maximum of 22 ufg's scattered)

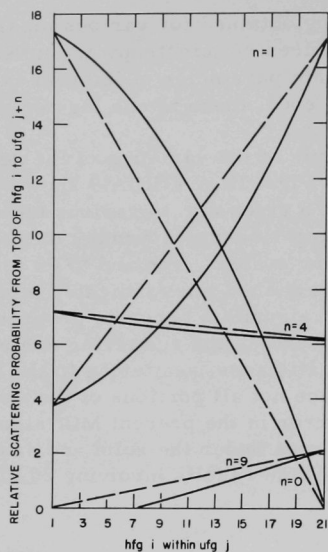


Fig. III.A.6

Iron: Source (ufg i) Energy Limits
of 6.116-6.065 MeV (maximum of
9 ufg's scattered)

Fig. III.A.7

Iron: Source (ufg i) Energy Limits
of 50.33-49.92 keV (maximum of
9 ufg's scattered)

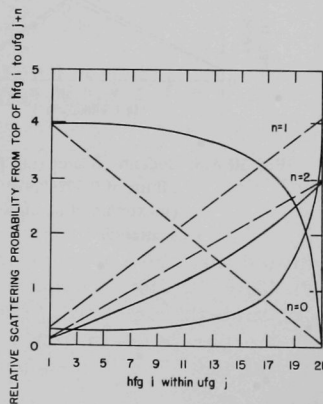
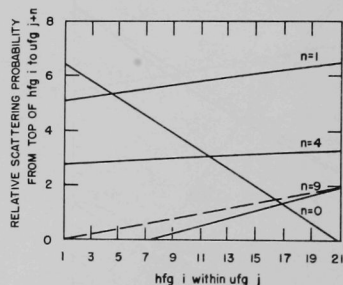


Fig. III.A.8

^{239}Pu : Source (ufg i) Energy Limits
of 2.052-2.035 keV (maximum of
3 ufg's scattered)

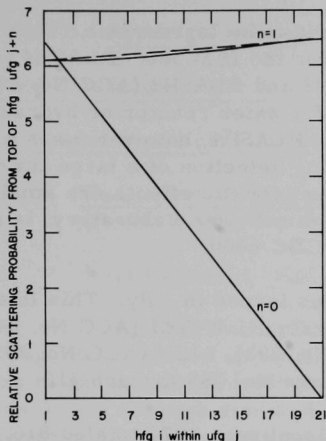


Fig. III.A.9

^{239}Pu : Source (ufg i) Energy Limits
of 6.116-6.065 MeV (maximum of
3 ufg's scattered)

2. Nuclear Data--Research and Development

a. Reactor Code Center (M. Butler)

Last Reported: ANL-7705, pp. 141-142 (June 1970).

During July, six program packages were incorporated in the Argonne Code Center library. Two of these were received from the General Electric Company Nuclear Systems Programs operation at Cincinnati, Ohio. They are GROUSE (ACC No. 420), a program which computes effective multigroup cross sections as a function of position in the reactor core or the absorber region of a fuel or control element, and MICHRD (ACC No. 421), which computes the Vickers Pyramid number for a specimen from filar micrometer eyepiece readings and calculates the microhardness increment fraction when comparing irradiated and control specimens. Both programs are written in FORTRAN IV for the GE 635 computer.

A replacement package for the x-y version of TWOTRAN (ACC No. 358), the two-dimensional design code, was supplied by Los Alamos Scientific Laboratory. This UNIVAC 1108 version includes a negative-flux fix-up. Argonne Code Center Note 71-1 was issued to all recipients of the original program informing them of the availability of this version.

Gulf General Atomic submitted the DYNAM program (ACC No. 440) written for the UNIVAC 1108. This FORTRAN dynamic-analysis program was developed for the study of once-through boiling-flow oscillations. The Atomics International HAA-3 program describing aerosol behavior has been assimilated as ACC No. 443. The time-dependent

particle-number distribution is assumed to be log-normal. This library package was written in FORTRAN IV for the IBM 360. FLASH4 (ACC No. 448), like its predecessors FLASH2 and FLASH3 (ACC No. 295), is used to study the transient response of a water reactor or hydraulic system to severe variable-pressure operation. FLASH4, however, uses a fully implicit integration technique permitting selection of a large time step for slowly varying transients where the acoustic effects are small. FLASH4, as supplied by the Bettis Atomic Power Laboratory, is a FORTRAN IV package written for the CDC 6600.

ANL-7411 Supplement 4 was issued in July. This latest supplement contains revised abstracts for FLANGE1 (ACC No. 247), GASKET (ACC No. 263), GGC4 (ACC No. 298), LION (ACC No. 299), and 2DB (ACC No. 325), and 26 new abstracts No. 385 through 410.

Package distribution for fiscal year 1970 totaled 816, 160 of these going to university installations.

B. Reactor Fuels and Materials Development

1. Fuels and Claddings--Research and Development

a. Behavior of Reactor Materials

- (i) Fuel-element Behavior: Theory, Modeling, and Analysis
(R. W. Weeks and V. Z. Jankus)

Last Reported: ANL-7688, pp. 166-167 (April-May 1970).

The LIFE-I code, although elaborate in many respects, contains rough descriptions of some processes and requires fitting several parameters to experimental data. In particular, fuel swelling due to fission gas depends on the average size and release rate of gas bubbles in each fuel region. These parameters are being adjusted by fitting the calculations to data obtained from tests on General Electric elements in Subassembly XG05.

Results of the preliminary calculations for the XG05-F2H fuel element were presented at the RDT Fuel Element Modeling Working Group Meeting held April 8-9, 1970. In addition to the results calculated from the actual EBR-II operating history, the calculated results for several steady-power "average" runs were presented. At that time, the observation was made that the results were sensitive to the averaging process used for the reactor operating history; however, quantitative agreement with observed results had not yet been achieved.

Through an iterative adjustment of some of the materials parameters, the calculations using the actual $2\frac{1}{2}$ -year EBR-II operating history were made to agree with experimental observations for the XG05-F2H fuel element. The calculations were unsuccessful for some time, since they tended to predict excessive strain and gas release. Satisfactory agreement with experiment was finally attained as the result of a suggestion by R. Poeppel. He suggested that, in the undisturbed zone of oxide fuel, the fission-gas bubbles are small and may be considered to occupy the minimum volume given by van der Waals (see Progress Report for January 1970, ANL-7661, pp. 100-101),

$$V = 2.389 \text{ in.}^3/\text{mole.}$$

In the equiaxed zone, it has been assumed that the average pressure due to the surface tension of the bubbles is $P_g = 1000$ psi, and fission gas is treated as ideal.

In Table III.B.1, experimental data are compared with calculated results, based on various assumed steady-state reactor operating histories, including the actual reactor history for the same burnup and

fluence. The results indicate that a single steady-power calculation cannot be expected to predict reliably all the measurable quantities that could be obtained from a postirradiation examination. In particular, predictions of the amount of gas released depend in a complex manner on the reactor operational history.

TABLE III.B.1. LIFE-I Results for Fuel Element XG05-F2H

Parameters	Experimental Values	Full History (911 days) ^a	Computer Predictions		
			Steady Peak Power (284.5 days), 14.4 kW/ft	Steady Average Power (369 days), 11.1 kW/ft	Steady Average Power (911 days), 4.5 kW/ft
Total fluence	0.38×10^{23}	0.380×10^{23}	0.379×10^{23}	0.379×10^{23}	0.379×10^{23}
Cladding swelling strain, %	~0.70	0.69	0.69	0.70	0.52
Cladding creep strain, %	~0.54	0.65	1.35	0.45	0.00003
$\Delta D/D$ final, %	~1.24	1.24	1.85	1.14	0.52
Outside radius of central void, in.	-	0.011	0.011	0.006	0.001
Outside radius of columnar zone, in.	-	0.062	0.062	0.011	0.002
Outside radius of equiaxed zone, in.	-	0.096	0.097	0.089	0.003
Fission gas generated, moles	$\sim 6.07 \times 10^{-3}$	5.9×10^{-3}	5.9×10^{-3}	5.9×10^{-3}	5.9×10^{-3}
Gas released, %	~68	69	38	30	39
Plenum pressure (700°F)	-	415	241	200	251
Cladding hoop stress at last power step, psi	-	7,988	27,321	35,307	1,788
Fuel-length increase, %	-	1.9	2.6	2.3	1.2
Cladding-length increase, %	-	1.5	1.8	1.4	1.0

^aFull history included 542 days at zero power.

b. Chemistry of Irradiated Fuel Materials (C. E. Crouthamel and C. E. Johnson)

(i) Postirradiation Studies of Reactor Fuels and Cladding

Last Reported: ANL-7688, pp. 176-178 (April-May 1970).

Recent effort has been directed toward electron-microprobe analysis of a cross section of pellet fuel of UO_2 -20 wt % PuO_2 ; this fuel specimen (F2R), which was obtained from the General Electric Laboratory at Vallecitos, was clad with Type 347 stainless steel and had been irradiated to 6.9 at. % burnup at 16 kW/ft. A brief examination of the fuel-cladding interface showed an interaction between fuel and cladding similar to that observed in other stainless steel-clad oxide fuels. The depth of cladding penetration averaged $\sim 15 \mu\text{m}$. Cesium was observed at the fuel-cladding interface, along with lesser amounts of barium, iodine, and aluminum. (The latter was probably introduced as an impurity during fuel preparation.) An enhancement of nickel was also observed along the inner grain boundaries of the cladding.

Analyses have been made to determine the radial distribution of uranium and plutonium in the fuel. Results available show that the

plutonium concentration is uniform from the cladding wall to a point ~ 0.2 mm from the central void, where an increase in concentration of ~ 2 wt % is observed. Absolute values for both the plutonium and uranium concentrations will be calculated by means of the computer program MAGIC (Microprobe Analysis, General Intensity Correction). The relatively small redistribution of plutonium in F2R differs considerably from the marked redistribution of heavy metals observed in HOV-15 and TVOV-1. (See Progress Report for February 1970, ANL-7669, p. 109.) The differences in distribution may be the result of density differences in the fuels: F2R is a high-density pellet fuel, whereas HOV-15 and TVOV-1 are vibrapacked fuels having low smear densities.

A large number of metal inclusions were found in F2R, but only a few have been examined. The two largest ($\sim 300\text{-}\mu\text{m}^2$ area) inclusions in the body of the fuel were examined in detail, and both were found to be homogeneous alloys. One of these inclusions contained 91% Mo, 5% Tc, 3% Ru, and 1% Rh, and the other contained 65% Pd, 27% Sn, 6% Sb, and 2% Te. Inclusions in the peripheral areas of the fuel consisted principally of molybdenum.

Another interesting feature observed in the F2R fuel was the presence of a heterogeneous, metallic-appearing material in several small radial cracks near the periphery of the fuel. This material was essentially pure molybdenum interspersed with smaller zones of a palladium-cadmium alloy. Analysis of the latter material at a point 0.19 mm from the cladding revealed a composition of 69.2% Pd and 30.7% Cd.

c. Thermodynamics of Fuel Materials (A. D. Tevebaugh and P. E. Blackburn)

(i) Total Vapor Pressures and Carbon Potentials in the Ternary U-C-Pu System

Last Reported: ANL-7669, pp. 110-112 (Feb 1970).

The carbon potentials and total pressures of the U-Pu-C system are being investigated. Total pressure of actinide metal species as well as carbon activity are being measured by a transpiration technique. Activity measurements over a wide range of temperature and with well-defined composition are needed to establish reliable thermodynamic quantities and to define phase-boundary composition. In particular, carbon-activity data are important in predicting possible carbon embrittlement of cladding by carbide fuel, the chemical state of fission products, and effects of additives on the properties of fast-reactor fuels.

The study of the vaporization behavior of the uranium-carbon system is continuing. Current emphasis has been placed on the effects of

oxygen contamination in uranium carbide on the system's uranium, carbon and oxygen potentials. These studies are important in establishing allowable levels of oxygen impurity in carbide fuels. Little is known about the stability and phase relations of the uranium-carbon-oxygen system. The oxycarbide phase has only been investigated in the presence of other phases such as U, UO_2 , U_2C_3 , and UC_2 .

Considerable effort has been made to purify the carrier gases CO, argon, and helium to minimize contamination from CO_2 , H_2O , and oxygen. To avoid the formation of $\text{UO}_2(\text{s})$ when investigating the single-phase UC_xO_y region, the oxygen partial pressure must be lower than that needed for the formation of $\text{UO}_2(\text{s})$. Therefore, very high CO/CO_2 ratios are required. With a gettering system consisting of a combination of hot copper and a Molecular Sieve, we were able to obtain a CO-He carrier gas mixture containing less than 0.1 ppm CO_2 .

Oxygen partial pressure, carbon activity, and total pressure of uranium-bearing species were measured at 2255 and 2355°K with a carrier gas having a CO partial pressure of ~10 Torr (balance helium). The uranium charge used in our studies consisted of a spherical -8 +12 mesh powder with the following composition: ~4.55 wt % carbon ($\text{C}/\text{U} = 0.96$), ~150 ppm oxygen, ~350 ppm nitrogen, and <200 ppm metallic impurities. The results are summarized in Table III.B.2. In the early runs carried out at relatively low carrier-gas flow rates, the CO/CO_2 ratio of the exiting gas was approximately an order of magnitude lower than that of the input gas. Recent experiments at high carrier-gas flowrates have minimized the discrepancy between input and output CO/CO_2 ratios. Metallographic examination of the residues did not show the presence of $\text{UO}_2(\text{s})$ in the matrix or on the surface of the particles in any of the experiments.

TABLE III.B.2. Tentative Values of Carbon Activity and Oxygen Partial Pressure for U-C-O System

	Run 95-1	Run 95-2	Run 100-1
Temperature, °K	2255	2255	2355
Time of run, hr	5.3	12	5.5
Carrier gas	CO-He	CO-He	CO-He
Flow rate, ml/min	180	180	1100
Partial pressure CO in carrier gas, Torr	~10	~10	~10
CO/CO_2 , input gas	1.3×10^5	1.3×10^5	3.2×10^4
CO/CO_2 , output gas	1.2×10^4	1.3×10^4	2.2×10^4
$-\log p(\text{O}_2)$ (based on input)	14.25	14.24	12.52
$-\log p(\text{O}_2)$ (based on output)	12.18	12.28	12.20
Carbon activity (based on input)	0.011	0.011	2.0×10^{-3}
Carbon activity (based on output)	0.0011	0.0012	1.4×10^{-3}
Composition	$\text{UC}_{0.99}\text{O}_{0.03}$	$\text{UC}_{1.00}\text{O}_{0.03}$	$\text{UC}_{1.00}\text{O}_{0.04}$
Nitrogen content, ppm	99	-	710
Metallographic examination	UO_2 not detected	UO_2 not detected	UO_2 not detected

From these data, we calculate carbon activities to be between 10^{-2} and 10^{-3} at 2255°K, and approximately 2×10^{-3} at 2355°K. For comparison, the carbon-activity values, based on our measurements with H_2 - CH_4 mixtures over "oxygen-free" UC_x compositions ranging from $C/U = 0.99$ to $C/U = 1.00$, yielded values of a_C ranging from 0.09 to 0.15, respectively, at 2255°K, and ~ 0.15 at 2355°K. The effect of a small addition of oxygen, e.g., 1.5-2.0 at. %, results in a significant reduction in the activity of carbon. This can have important implications in the potential transfer of carbon from fuel to cladding materials.

The total pressure of uranium-bearing species at 1773, 2155, 2255, and 2355°K is shown in Fig. III.B.1. The total pressure of

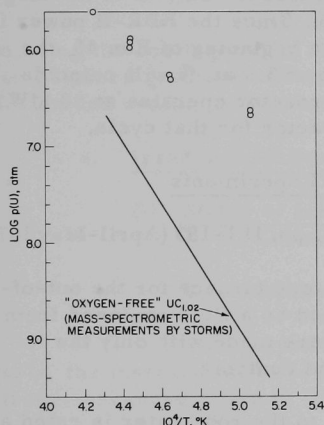


Fig. III.B.1

Preliminary Values for Total Pressure of Uranium-bearing Species over Uranium Oxy-carbides Containing 1.5-2.0 at. % Oxygen

uranium-bearing species over uranium oxy-carbide composition is considerably higher than those obtained with "oxygen-free" material.* These higher pressures may reflect in part the enhancement in uranium activity as a consequence of the significant reduction of carbon activity in the oxy-carbide, as well as the vaporization of an oxygen-containing uranium species from the oxy-carbide composition.

The free energy of formation of the oxy-carbide compositions given in Table III.B.2 was roughly estimated from oxygen- and carbon-activity values derived from our measurements. In the absence of species information, the uranium activity was roughly estimated based on the total pressure or uranium-bearing species, the assumption that the vapor is uranium gas, and the sublimation pressure of pure uranium. From the expression $\Delta G_f^\circ = R'T \log N_U \sum a_i$, tentative values of $\Delta G_f^\circ \approx -30.1$ and -38.8 kcal/mol were obtained at 2255 and 2355°K, respectively. The free energy of formation of "oxygen-free" $UC_{1.00}$ calculated from our carbon-activity measurements and Storms' adjusted vapor pressure measurements* was $\Delta G_f^\circ \approx -24.8$ kcal/mol at 2255 and 2355°K.

*Storms, E. K., The Refractory Carbides, Academic Press, New York, N. Y. (1967), Ch. XI, p. 205.

d. Oxide Fuel Studies

(i) Fuel-element Performance (L. A. Neimark, W. F. Murphy, and H. V. Rhude)

(a) Irradiation of Group O-3 Fuel Elements

Last Reported: ANL-7705, p. 144 (June 1970).

Through two-thirds of EBR-II Run 44, the 18 mixed-oxide fuel elements of Group O-3 have accumulated 7400 MWd exposure in Subassembly X072. This exposure is 78% (2.7 at. %) of the first target burnup of 3.5 at. %. Approximately 9700 MWd exposure or 97% of the target will have been accumulated at the end of Run 45. Since the EBR-II power is scheduled to increase from 50 to 62.5 MW at the beginning of Run 46, the practical achievement of the first target burnup of 3.5 at. % will coincide with the conclusion of Run 45. However, if the reactor operates at 50 MW during Run 46, Group O-3 will remain in the reactor for that cycle.

(b) Out-of-reactor Simulation Experiments

Last Reported: ANL-7688, pp. 181-183 (April-May 1970).

The Centorr high-temperature furnace for the out-of-reactor simulation experiments has been checked by a field engineer from Centorr and is now in operation. Initial runs were made with only the central-rod heater to check the power output and controls.

Although the power supply to the rod heater is rated at 10 kW, the maximum power achieved was 1.5 kW for a 0.040-in.-dia tungsten heating element and 2.5 kW for a 0.060-in.-dia tungsten heating element. To achieve higher power ratings, shorter heating elements will have to be used, which will require some modifications of the electrode holders.

A test fuel element (6 in. long, 0.377-in. diameter), with lavite pellets instead of urania pellets, was heated in the furnace to check the proposed test procedure. With a central temperature of 2200°C, the outer cladding surface reached a temperature of 1085°C, and the end plugs on the fuel element melted and reacted with the tungsten heating element, which burned out the element on one heating cycle. This high a cladding temperature at this fuel temperature is unacceptable for the planned tests, and additional cooling will be required.

At 1085°C, the fuel-element cladding showed considerable distortion during the one heating cycle. The diameter after heating varied from 0.367 to 0.382 in. compared with 0.377 in. before heating, which produced an out-of-round cross section and a "bambooing" effect along the

length of the element. The wall thickness of the Type 304 stainless steel jacket was 0.012 in., and the initial annulus between pellets and jacket was 0.001 in.

Several tests were run at heating rates of 100 to 1000°C/min with bare urania pellets to check the cracking behavior of the urania in the Centorr furnace. The results were the same as achieved previously for single pellets in the mockup furnace. However, when a stack of nine pellets was heated, some of the middle pellets did not crack--even at the higher heating rate. Also, the pellets did not achieve the restructuring and pore migration observed in the mockup furnace. This is probably because of the reduced temperature gradient in the Centorr furnace.

Additional cooling capacity is being added to the furnace to bring the cooling jacket closer to the fuel element and thus increase the temperature gradient. Other modifications are also being made in both design and cooling of the end plugs of the fuel element.

e. Irradiation Effects in Creep of Oxide Fuels

(i) Status of Instrumented Creep Capsule (A. A. Solomon and R. H. Gebner)

Last Reported: ANL-7669, pp. 114-115 (Feb 1970).

Based upon a number of assembly operations and proof tests, the instrumented creep capsule (ICC) used to study the radiation and fission-enhanced creep of UO₂ helical springs has been significantly altered.

(a) Brazing of Thermocouples, Self-powered Neutron Detectors and the Linear Variable Differential Transformer. In the original design of the brazing header, brazing tubes were provided for torch brazing, but insufficient space had been allowed for this operation; therefore, an induction technique was adopted. Then the inductive coupling to the tubes was found to be very poor, which resulted in nonlocalized heating; moreover, header clearances were too large. A new header was designed following the methods developed by D. Walker.* Acceptable vacuum-tight brazes resulted by brazing in flowing hydrogen.

(b) Welding and NaK Filling of Practice Capsules. On May 18, 1970, trial welding and NaK filling of two capsules were performed at Vallecitos Nuclear Center (VNC). Techniques of vertical welding were developed and performed. X-ray examination of the vertical closure welds indicated nearly 100% penetration.

*Memo to A. Smaardyk from D. Walker, March 6, 1970.

A procedure was instituted and an apparatus was built for NaK filling at $\sim 200^{\circ}\text{C}$ in vacuum to achieve good wetting of the UO_2 helix. Bubbles appeared in the NaK fill tubes, which indicated a need for out-gassing of the NaK supply. Fortunately, the bubbles that appeared were vented through fill tubes so that good wetting was achieved within the capsule.

It was determined that purification of the argon cover gas was necessary to prevent contamination of the NaK. As will be discussed, low oxygen potential is also necessary to prevent oxidation of the UO_2 . The attack of UO_2 by NaK in air is shown in Fig. III.B.2, where the few unreacted NaK droplets clinging to the UO_2 spring formed deep indentations in the spring in 15 min.

Handling the capsule containing a loaded UO_2 spring appeared satisfactory; no breakage occurred during welding and NaK filling. The second trial capsule assembly is shown in Fig. III.B.3.

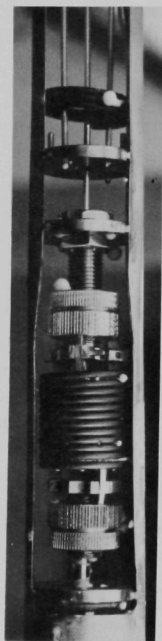


Fig. III.B.2
Instrumented Creep Capsule
Drained of NaK Showing
Attack of NaK on UO_2 in
Air

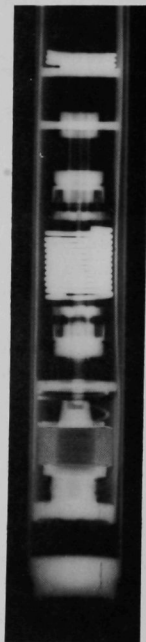


Fig. III.B.3
Assembled Instrumented
Creep Capsule before NaK
Filling



Fig. III.B.4

NaK-filled Trial Capsule
Showing Thermocouple
Heater and Suspended UO_2
Helical Spring

(c) Capsule Temperature Gradients. To obtain more realistic capsule temperature profiles, one of the trial capsules that was NaK-filled at VNC was modified to simulate the fissioning UO_2 spring using a helically wound heater with the same geometry as a UO_2 spring. This was a relatively simple modification, since one of the sheathed Chromel-Alumel thermocouples was used as a heater. An X-ray showing the NaK-filled capsule, heater, and various measuring thermocouples is shown in Fig. III.B.4. The measuring thermocouples were spaced to indicate the actual heater temperatures, the temperatures at some distance away from the heater, and the axial temperatures due to convection currents. An immersed UO_2 spring suspended from the heater is also shown in Fig. III.B.4.

The results of the experiment are shown in Fig. III.B.5. When these data are extrapolated to the highest fission power rating for the capsule (~ 1800 W), and corrections are made for differences in coolant water temperature, the resultant maximum UO_2 spring temperature is surprisingly low (157°C). This compares with a calculated temperature of 220°C , if only conductive heat loss is considered. Thus, convection of the NaK plays an important role in the heat-transfer mechanism. When calculations are made for the temperature gradients within the UO_2 spring, assuming uniform heat generation from a cylindrical rod, the maximum centerline temperature of the UO_2 spring

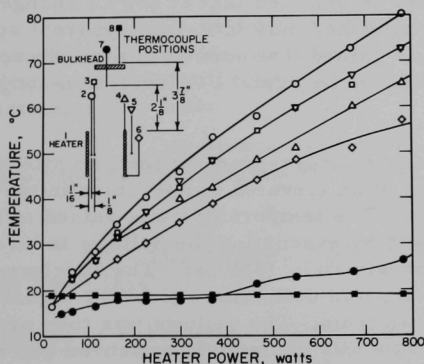


Fig. III.B.5

Temperature Gradients in the
Trial NaK-filled Capsule as a
Function of Heater Power

is only $\sim 187^{\circ}\text{C}$. These calculations and measurements indicate that the first ICC UO_2 spring will operate at very low temperatures.

(d) Effects of NaK on the UO_2 Helical Springs. After the temperature-gradient test, the small capsule shown in Fig. III.B.4 was heated for 4 days at 300°C . When the UO_2 spring was exposed, the brownish surface color indicated that a good deal of oxidation had occurred on the surfaces of the spring. This oxidation is consistent with thermodynamic data, and indicates that stoichiometric UO_2 is oxidized in preference to sodium (Na_2O has a lower free energy of formation than K_2O), whereas $\text{UO}_{2.001}$ is reduced by sodium at all temperatures $< 1200^{\circ}\text{C}$. This suggests a further justification for using high-purity or low-oxygen-potential NaK and argon cover gas.

(e) Thermal Creep Capsule. A third complete trial capsule was assembled to test the various functional components of the capsule, viz., bellows operation, load application, strain measurement system, and sensitivity of the capsule to temperature changes. To perform these tests, the complete capsule assembly was isolated in an inert-flowing-argon atmosphere to prevent oxidation at the relatively high temperatures anticipated. A depleted UO_2 spring was mounted in the capsule, and the capsule was first evacuated to 10^{-5} Torr and back-filled with argon to atmospheric pressure. A load of ~ 260 g was applied to the spring, which corresponds to an outer fiber shear stress of ~ 1500 psi. The bellows was actuated a number of times to test for proper operation.

The capsule was heated in a long furnace (76 cm) to simulate the temperature gradients and temperature changes that would be encountered in the reactor. The first test was conducted to examine the effect of changes in capsule temperature on the sensitivity of the specimen-length measuring system. It was determined that at 400°C , changes in capsule temperature of $\sim 100^{\circ}\text{C}$ produced only 0.02-mm apparent specimen deflection. Thus, confidence was gained that normal changes in reactor power would not produce an error in the actual UO_2 specimen-length measurement.

After the temperature-gradient test, an attempt was made to creep-test a UO_2 spring at an elevated temperature in the capsule and to test the bellows operation. The temperature was raised to 800°C , and the load was slowly increased by evacuating the bellows to an equivalent outer-fiber shear stress of approximately 1500 psi. The specimen began deforming properly, but after ~ 2.5 mm deflection the LVDT signal indicated sticking was occurring in the load train. The bellows was then pressurized to relieve the load, and the capsule was cooled. The pushrod had buckled and was binding with the guides. In spite of this difficulty, it was concluded that the UO_2 spring crept properly and coaxially, that the bellows system worked properly both during unloading and loading, and that the strain-measuring system worked satisfactorily.

(f) Capsule Redesign. The above tests as well as thermal creep tests of UO_2 helices suggested that rather extensive modifications in capsule design, assembly, and testing were necessary. The present capsule configuration is shown in Fig. III.B.6. In addition to the redesign of the brazing header assembly, the following modifications were made:

(1) The bellows travel was lengthened to 2.54 cm to increase the effective strains obtainable and to deform the springs into the steady-state regime.

(2) The bellows system was modified to operate under pressure with a restoring spring so that a leak in the bellows system would not destroy the specimen.

(3) The UO_2 spring support system was changed to allow for the unavoidable grip rotation that would have broken the UO_2 spring.

(4) The cage assembly was redesigned to facilitate assembly.

(5) The grip design was modified to prevent a grip from falling out of the spring during thermal creep tests. Also, the pivot point was moved into the grip plane to allow for grip rotation and prevent breakage of the UO_2 specimen.

(6) The grips were changed to zirconium following the suggestion of H. Stevens (ETD) to provide a more uniform flux distribution around the specimen.

(7) The bulkheads were modified to facilitate assembly and provide better NaK convection flow and cooling.

(8) The pushrod was made into a tubular configuration to reduce friction and prevent buckling.

(9) Self-powered neutron detectors were incorporated in the capsule to provide a continuous absolute measure of flux level during the irradiation so that the appropriate adjustments could be made to maintain a particular flux level.

(10) Special connectors, pressure indicators, and flow-metering systems were designed for proper bellows operation.

(11) A method of loading the pushrod was developed.

(12) Bellows guides were incorporated to allow the bellows to move freely.

2. Techniques of Fabrication and Testing--Research and Development

a. Nondestructive Testing Research and Development (H. Berger)

(i) Neutron Radiography (J. P. Barton)

Last Reported: ANL-7705, pp. 146-148 (June 1970).

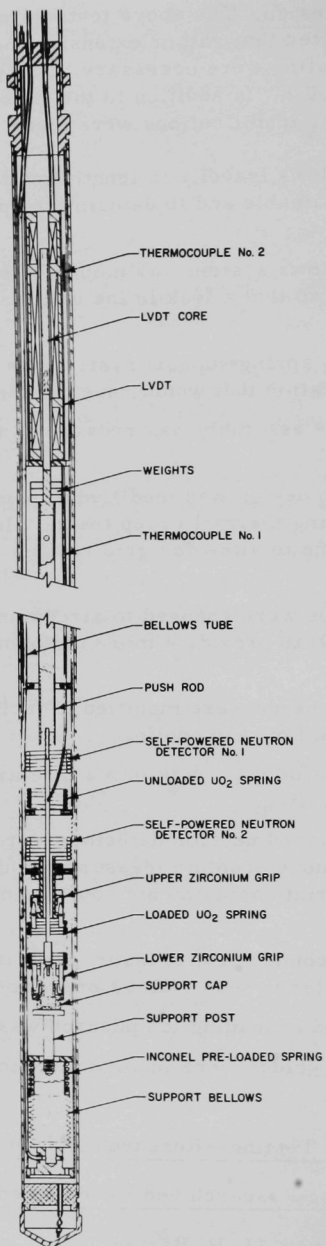


Fig. III.B.6

Instrumented Creep Capsule

In reactor-fuel inspection, as in other neutron-radiography applications, the quality of radiography can vary appreciably. Recent tests of fuel samples, using different neutron-radiography techniques, have revealed quite different penetration and contrast. Also, precise dimensional measurements of fuel samples obtained by using three neutron-radiography facilities have yielded different results. Many variables must be controlled, and, in some circumstances, the use of an object IQI can be recommended to check the consistency of the tests.

In collaboration with several neutron-radiography groups, a proposed object IQI has been designed. The design consists of three similar test strips set on the emergent beam side of steps of material to be radiographed, as shown in Fig. III.B.7. The IQI measures an area of 2.5 by 2.8 cm, and the thicknesses of the three steps are T , $\frac{1}{2}T$, and zero, where T is the thickness of the specimen being neutron radiographed.

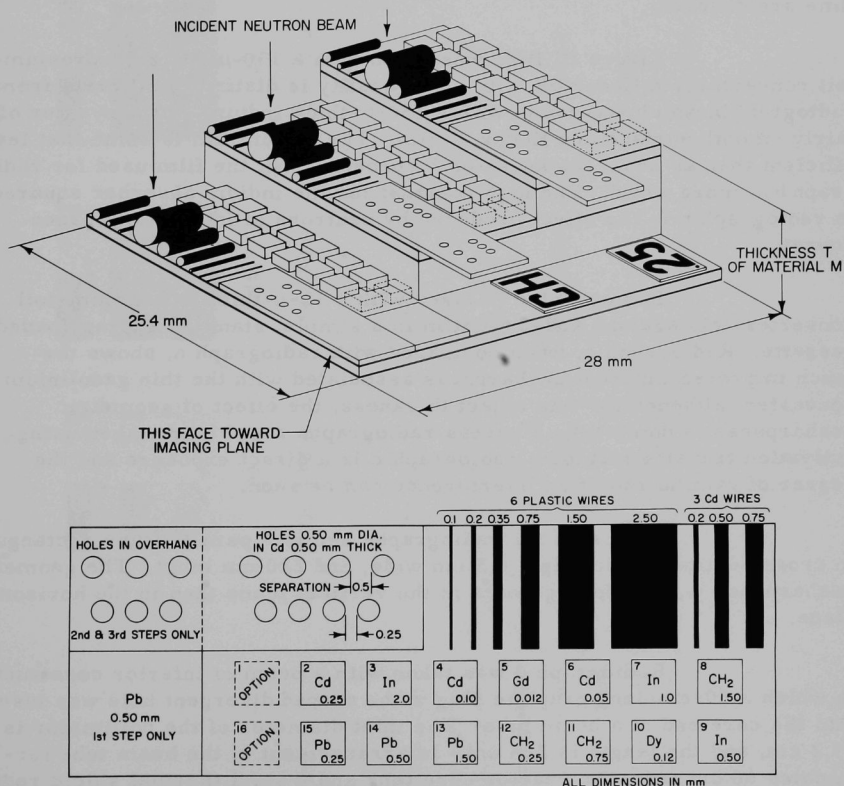


Fig. III.B.7. Design for Object Image Quality Indicator

The test strips include sets of holes in cadmium, sets of wires of cadmium and plastic, and sets of absorber thicknesses of selected materials Cd, In, Gd, CH_2 , Dy, or Pb. Two spaces are provided for optional absorber materials, which would normally be selected thicknesses of the special fuel material to be inspected.

The small IQI could be placed in the corner adjacent to the object in every neutron-radiographic exposure. It should help reveal unexpected changes in neutron penetration, scattering effects, film quality, etc.

Neutron radiographs of the object IQI taken under five different conditions are shown in Fig. III.B.8. The prints cannot reveal the latitude of detail available in the negative radiograph, and are included only as a demonstration of geometry. In Fig. III.B.8a-c, the radiographs have the same neutron-beam arrangement, but the converter foil, film, and exposure time are different.

Figure III.B.8a was taken with a $130\text{-}\mu$ -thick dysprosium-foil converter and Kodak SR film. The quality is distinctly different from radiograph b, which was taken with a $250\text{-}\mu$ -thick indium-foil converter of fairly smooth surface and Kodak T film. The indium foil is somewhat less efficient than an equal thickness of dysprosium, but the film used for radiograph b is more rapid. The high contrast for the indium absorber squares in radiograph b is the effect produced by neutrons of indium resonance energy.

Radiograph c is taken with a $13\text{-}\mu$ -thick gadolinium-foil converter held against Kodak SR film in a simple, standard spring-loaded cassette. Radiograph c, when compared with radiograph a, shows the much improved inherent unsharpness associated with the thin gadolinium converter, although for this object thickness, the effect of geometric unsharpness is dominant. Whereas radiographs a and b are taken using activation transfer methods, radiograph c is a direct exposure and the degree of gamma radiation interference can be seen.

The beam for radiographs a-c is a parallel tube rectangular in cross section (10 cm high, 6.3 cm wide, and 220 cm long). The geometric unsharpness is, therefore, greater in the vertical plane than in the horizontal plane.

Radiograph d was taken with a beam of inferior construction in which a 50-cm-long graphite plug with a shaped divergent hole was inserted into the core end of a beam tube. The inlet diameter of the collimator is 15.2 cm, and the length is 224 cm. In arrangement c, the beam tube terminates 60 cm from the reactor core tank and a steel thermal shield reduces gamma interference; in arrangement d, the beam tube penetrates closer to the core and has no gamma shield. This latter factor, together with the use of the short graphite plug for geometry definition, leads to a poorer thermal-neutron spectrum and a poorer neutron-gamma ratio for d.

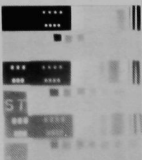
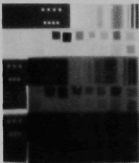
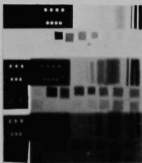

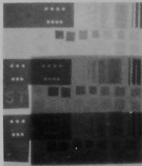
					
	(a)	(b)	(c)	(d)	(e)
Converter	Dy 130 μ	In 250 μ	Gd 13 μ	Gd 13 μ	Gd 13 μ
Film	SR	T	SR	SR	SR
Collimator aperture, cm	10 x 6.3	10 x 6.3	10 x 6.3	15.2 (dia)	2.5
Collimator length, cm	220	220	220	224	224
Reactor power, kW	200	200	200	20	200
Exposure method	Transfer	Transfer	Direct	Direct	Direct
Exposure time, min	20	3	3 $\frac{3}{4}$	3	5 $\frac{1}{2}$

Fig. III.B.8. Neutron-radiograph Image Quality Indicator

The detrimental factors are largely overcome by using arrangement e in which a 2.5-cm-dia graphite plug is substituted for the 15.2-cm inlet aperture. For many applications, the evident higher geometric resolution and higher latitude or penetration of exposure e would be the best choice among the five examples.

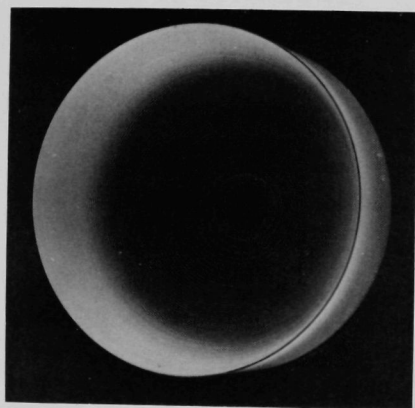
Consequently, for routine or special neutron-radiographic examination of fuel elements or irradiation capsules, the use of an object IQI is recommended. The object IQI may be the design proposed, or an improved design, but clear advantages accrue by having a recognized standard for comparison.

(ii) Laser Studies and Holography (N. Fernelius)

Last Reported: ANL-7688, pp. 185-187 (April-May 1970).

An investigation of ultrasonic imaging techniques has been initiated. According to an approximate formula,* the ratio of diffracted light-to-incident light in a Bragg cell is linearly proportional to the half-apex angle of the incident cone of sound. This implies that sound should be focused to a point or line. Since the transducer in our equipment produces a nearly planar sound wavefront at 2 MHz, it was easier to construct an acoustic lens than to order and mount a spherical transducer.

Some recent papers** have contained designs for acoustic lenses based on the concepts of Fresnel zone plates and lenses in optics.



These lenses have the approximate shape of a circular stadium. After a slight modification of the formula given by Tarnoczy,** a FORTRAN-IV computer program was written to calculate the necessary radii of the acoustic lens. The lens material is Lucite and is designed to operate in water at a frequency of 2 MHz. The focal length is 10.2 cm. Some 70 zones of step-height (0.135 cm) were necessary to obtain the 10-cm diameter that completely covered the flat transducer. The lens was produced on a computer-controlled lathe. The result is shown in Fig. III.B.9.

Fig. III.B.9. Lucite Acoustic Lens for 2-MHz Sound in Water. Focal length is 10.2 cm.

In operation in the water tank, the most pronounced focusing seemed to appear when the lens was placed

*Korpel, A., Optical Imaging of Ultrasonic Fields by Acoustic Bragg Diffraction, Drukkerij Bronder, Rotterdam (1969), p. 159.

**Tarnoczy, T., Ultrasonics 3, 115 (1965); Golis, M. J., IEEE Trans. on Sonics and Ultrasonics SU-15, 105 (1968).

flat against the surface of the transducer. A disadvantage of this design is that the height of the lens at the edges is about 7 cm, which does not allow much room for a sample between the lens and the focal point.

3. Engineering Properties of Reactor Materials--Research and Development

a. Fabrication of Well-characterized UO_2 Test Specimens (R. O. Meyer, J. T. A. Roberts, and J. C. Voglewede)

Not previously reported.

Sintered UO_2 test specimens with well-controlled density, grain size, stoichiometry, and homogeneity are required for both the high-temperature mechanical-properties measurements and the temperature-gradient migration studies in the Fuels and Claddings Program. A cooperative effort is under way to achieve the various material properties needed for test specimens. The progress made in producing high-density material and in eliminating a microstructural defect from the sintered material will be described.

Previous fabrication techniques have produced material that is about 97% of theoretical density by pressing $1/2 \mu$ particle-size UO_2 powder in a steel die at a pressure of 0.69 kbar (10,000 psi), with no binders. This preformed compact is hydrostatically pressed at 1.72 kbar (25,000 psi) and then sintered in flowing hydrogen at 1700°C for 4 hr or more, depending on the grain size desired.

The effect of hydrostatic pressure on sample density has been investigated by extending the previously available pressure range.* Keeping all the previous parameters except hydrostatic pressure the same, a series of specimens has been fabricated to show the effect of the hydrostatic pressure on final density. Pressures of 8.1 kbar (118,000 psi) and 8.6 kbar (125,000 psi) were used, and the resulting density values are listed in Table III.B.3. The increase in density of 0.5% theoretical achieved by the application of very high pressures corresponds to a decrease in porosity of over 20%, which is quite significant.

Fully dense UO_2 is needed for the temperature-gradient migration work. Single crystals of UO_2 are available, but not in large quantities. Since large specimens (1-cm diameter by 1-cm long) are required even though the region of interest within the specimen is small, it should be possible to use composite samples made of single-crystal pieces (1-mm dimension) embedded in sintered compacts. An attempt was made to fabricate composites by placing single-crystal chips** in the powder and cold-pressing and sintering in the normal way. The resultant material was unsatisfactory and had the appearance of a cauliflower. The powder compacts shrink

*Pressures above 3.4 kbar (50,000 psi) were produced with the cooperation of J. N. Mundy.

** UO_2 single crystals were provided, under a materials and information exchange program, by Harlem J. Anderson, Battelle Memorial Institute, Pacific Northwest Laboratory.

about 20% during sintering, and this shrinkage around the single-crystal pieces caused the sample to fracture badly. A similar mixture of powder and single-crystal chips was sent to a commercial hot-pressing company.* Two samples were hot-pressed at a temperature near 1810°C, one at a pressure of 138 bars (2000 psi) and the other at 414 bars (6000 psi). Sound specimens resulted, with chips well bonded in the material. Although not fully appraised, it appears that the method will provide a convenient means of preparing specimens with fully dense regions.

TABLE III.B.3. Final Sintered Density as a Function of Pressure of Cold-pressing

Hydrostatic Pressure, kbar	Average Density, % TD	Density Variation (average deviation), % TD	Number of Specimens Measured
0.7	97.29	0.03	3
1.7	97.56	0.04	3
3.4	97.67	0.02	2
8.1	98.28	-	1
8.6	98.11	0.06	5

Hot-pressing is also a possible method that can be used to produce high-density sintered material. Initial attempts by Cerac have given densities up to 96.5% of theoretical, but the density varied by almost 2% of theoretical across the 6.3-cm-dia sample. This method will be explored further, when the installation of a hot press is completed at ANL.

Finally, defects, or "freckles," have been widespread throughout the cold-pressed and sintered UO_2 . These freckles, when closely examined with the scanning electron microscope, are regions of low density with dimensions as large as 100 μ . Such microstructural defects could have a profound effect on the mechanical properties of the oxide, especially when measurements are made on high-density material. Freckles are now eliminated by using powder that has been defloculated.** (Defloculation is a chemical process incorporated during powder preparation to prevent particle agglomeration.) Elimination of these low-density regions is significant enough to affect the density measurements. All the samples in Table III.B.3 were made from defloculated powder. Twelve samples made from powder that was not defloculated yielded an average density of 97.05% of theoretical, with an average deviation of 0.37% of theoretical density when pressed at 1.7 kbar (25,000 psi). This is 0.5% of theoretical density lower

*Cerac Hot-Pressing, Inc., Menomonee Falls, Wisconsin.

**A defloculation technique was developed for use in the fabrication of helical UO_2 specimens by J. T. Dusek.

than the corresponding samples in Table III.B.2, and the density is less consistent from sample to sample than with the deflocculated powder. Thus, the combination of deflocculated powder and very high pressure has yielded a 1% theoretical density increase in the sintered sample.

b. High-temperature Mechanical Properties of Ceramic Fuels

(i) Out-of-reactor Creep of UO₂ Helices (A. A. Solomon and R. H. Gebner)

Not previously reported.

The correlation of in-reactor and out-of-reactor deformation of depleted UO₂ helical springs has led to a number of measurements of the apparent activation energy for creep (Q_C) of slip-cast UO₂ helices at relatively low temperatures. The measurements are important since they include measurements of Q_C down to 1000°C, which is in the normal operating temperature range for the outer regions of an oxide fuel pin.

The instantaneous temperature change technique was used to determine Q_C . (See Progress Report for February 1970, ANL-7669, pp. 114-115.) Positive and negative temperature changes of ~10° were made, and individual specimens were used for a range of temperatures at a particular stress. The tests were conducted at 10⁻⁵ Torr, and gravimetric determinations of the oxygen-to-metal (O/M) ratio indicated no change in stoichiometry during the test. The starting material was stoichiometric because of prior hydrogen sintering.

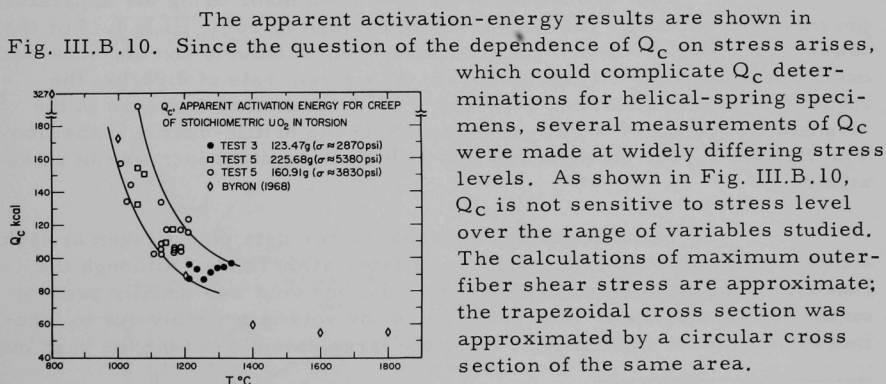


Fig. III.B.10. Apparent Activation Energy for Creep of Stoichiometric UO₂ Slip-cast Helical Springs

The values of Q_C measured at ~1350°C agreed quite well with published data. However, the most

striking feature of the lower temperature deformation was the rapid increase in apparent activation energy as the temperature was reduced to 1000°C. Normally Q_C decreases with temperature, which is consistent with deformation processes acting in parallel. The anomalous increase in Q_C for metals has often been associated with various second-order phase changes, e.g., the Curie transformation and various ordering processes. This suggests that an impurity-type of ordering in UO_2 may be responsible for the anomalous increase in Q_C . Additional measurements of Q_C will be made using extruded UO_2 springs in flowing hydrogen to determine the origin of the increasing Q_C at lower temperatures.

(ii) Plastic Yielding and Fracture of Fuel Oxides
(J. T. A. Roberts and B. J. Wrona)

Last Reported: ANL-7679, pp. 129-130 (March 1970).

Mixed-oxide test specimens of sintered UO_2 -20 wt % PuO_2 have been fabricated in Bldg. 350. The dimensions of the test bars were changed to 0.6 cm wide by 0.35 cm high by 4.5 cm long. This thinner bar helps to economize on material. The primary purpose of the modification, however, was to obviate the necessary correction for the modulus-of-rupture formula to obtain true cross-bending strengths when the ratio of span-to-bar depth is 10:1.* Below this ratio, the strengths are too high. For the bar used in recent UO_2 work,** the ratio was approximately 5.0, but the dimensions of the latest bars yielded a ratio of ~9; therefore, no correction will be necessary.

Four-point bend tests have been made using the apparatus previously described. The data are summarized in Table III.B.4. For the lower strain rate (0.04/hr), the transition from brittle-to-ductile behavior occurred below 1400°C (Fig. III.B.11). At a strain rate of 0.08/hr, the transition occurred between 1400 and 1500°C. A smooth increase in the strength of UO_2 -20 wt % PuO_2 occurred up to the brittle-ductile transition T_C . Beyond T_C , the strength fell off, with a concomitant increase in plastic strain.

The discrepancy between the two data points taken at each temperature was due to the presence of fabrication flaws. Although the tension surface was generally free of voids, one void was usually present on the fracture surface. The presence of the void is probably due to inhomogeneous binder distribution, since the large particles of binder burn out

*Milligan, L. H., Note on Modulus of Rupture of Cylindrical Ceramic Rods When Tested on a Short Span, J. Am. Ceramic Soc. **36**(5), 159-160 (1953); Duckwork, W. H., Precise Tensile Properties of Ceramics, *ibid.* **34**(1), 1-9 (1951).

**Canon, R. F., Roberts, J. T. A., and Beals, R. J., High Temperature Deformation of UO_2 , to be submitted to J. Am. Ceramic Soc.

during sintering and leave a hole. The presence of a hole will result in a drastic reduction of brittle strength, on the basis of the Griffith criterion for fracture.*

TABLE III.B.4. $\text{UO}_2\text{-PuO}_2$ Mechanical Property Data

Immersion Density, % TD	Sample Number	Test Temperature, °C	Modulus of Rupture, M_R , kg/cm ²	Elastic Strain, ϵ_e	Plastic Strain, ϵ_p
0.04/hr Strain Rate--Batches V1 and V2					
95	V1-2	RT ^a	517.7	0.00037	
95	V1-3	RT ^a	485.2	0.00038	
95	V2-1	RT ^a	544	0.00034	
95	V1-4	500	476.5	0.00051	
95	V1-5	500	436.0	0.00032	
95	V2-2	500	310	0.000476	
95	V1-6	1000	1182.9	0.000596	
95	V1-7	1000	1196.5	0.00061	
95	V2-3	1000	1155	0.001	
95	V2-4	1400	1657	0.0022	0.00496
95	V2-5	1500	Unbroken	0.000185	0.0165
0.08/hr Strain Rate--Batch V3					
96	V3-1	500	684.7	0.00061	
96	V3-2	500	585.2	0.00056	
96	V3-3	1000	831.1	0.00059	
96	V3-4	1000	1039.4	0.00053	
96	V3-6	1250	1292.3	0.0010	
96	V3-7	1250	866.4	0.00077	
96	V3-8	1400	922.83	0.00129	
96	V3-9	1400	1460.8	0.0016	
96	V3-10	1500	1104.3	0.00039	0.00152
96	V3-11	1500	1380.0	0.00076	0.00179
96	V3-12	1600	Unbroken	ND ^b	0.034
96	V3-13	1600	Unbroken	ND ^b	0.019

^aRT = room temperature.

^bND = not detectable.

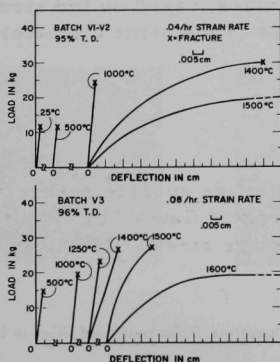


Fig. III.B.11

Load-deflection Curves for $\text{UO}_2\text{-20 wt } \%$ PuO_2 bars Strained at 0.04/hr and 0.08/hr

*Griffith, A. A., The Phenomenon of Rupture and Flow in Solids, Trans. Royal Soc. (London), Series A 221(4), 163-198 (1921).

Attempts are being made to fabricate specimens without large flaws. Since this may not be possible, many tests will be necessary at each temperature to obtain a statistically significant strength-versus-temperature relationship.

(iii) Fractography of UO_2 (J. T. A. Roberts and J. E. Sanecki)

Last Reported: ANL-7669, pp. 120-122 (Feb 1970).

The examination of fracture surfaces of UO_2 specimens broken in four-point bending* is continuing. Certain new features have been revealed by systematically scanning the entire fracture surface with the scanning electron microscope. Figure III.B.12 shows representative areas of a fracture surface obtained at a temperature of 500°C and a strain rate of 9.2/hr. The appearance is typical of a brittle transgranular fracture. Numerous cleavage steps are evident, some of which are indicated on the high-magnification micrographs.

In this and other surfaces examined, areas of dense porosity or "freckles" were evident (located near the tension surface in Fig. III.B.12), which had not been fully identified. Their occurrence was accepted as part of the fabrication process. Figure III.B.13 shows a typical area on a polished, etched specimen. The porosity is intergranular and is concentrated in areas that can be as large as $100\ \mu$ in diameter. Freckles probably constitute the major flaws in the UO_2 and can account for at least two experimental observations,* namely, the low brittle strength and the absence of an effect on the strength due to grain size.

Similar flaws, but only $\sim 50\ \mu$ in diameter, were observed by Evans and Davidge** in UO_2 tested at Harwell. They calculated fracture stresses that were similar to measured values, based on the stress necessary to extend a sharp "penny-shaped" flaw of the same diameter. The stress can be given by the relation†

$$\sigma = \left(\frac{2E\gamma_i}{\pi c} \right)^{1/2},$$

where E is Young's Modulus, γ_i is the effective surface energy for fracture initiation, and c is the dimension of the largest flaw. The result of substituting $c = 100\ \mu$ into the equation is a fracture stress $\sim 30\%$ lower than Evans

*Canon, R. F., Roberts, J. T. A., and Beals, R. J., High Temperature Deformation of UO_2 , to be submitted to J. Am. Ceram. Soc.

**Evans, A. G., and Davidge, R. W., The Strength and Fracture of Stoichiometric Polycrystalline UO_2 , J. Nucl. Mater. 33(3), 249-260 (1969).

†Sack, R. A., Extension of Griffith Theory of Rupture to Three Dimensions, Proc. Royal Soc. 58, 729-736 (1946).

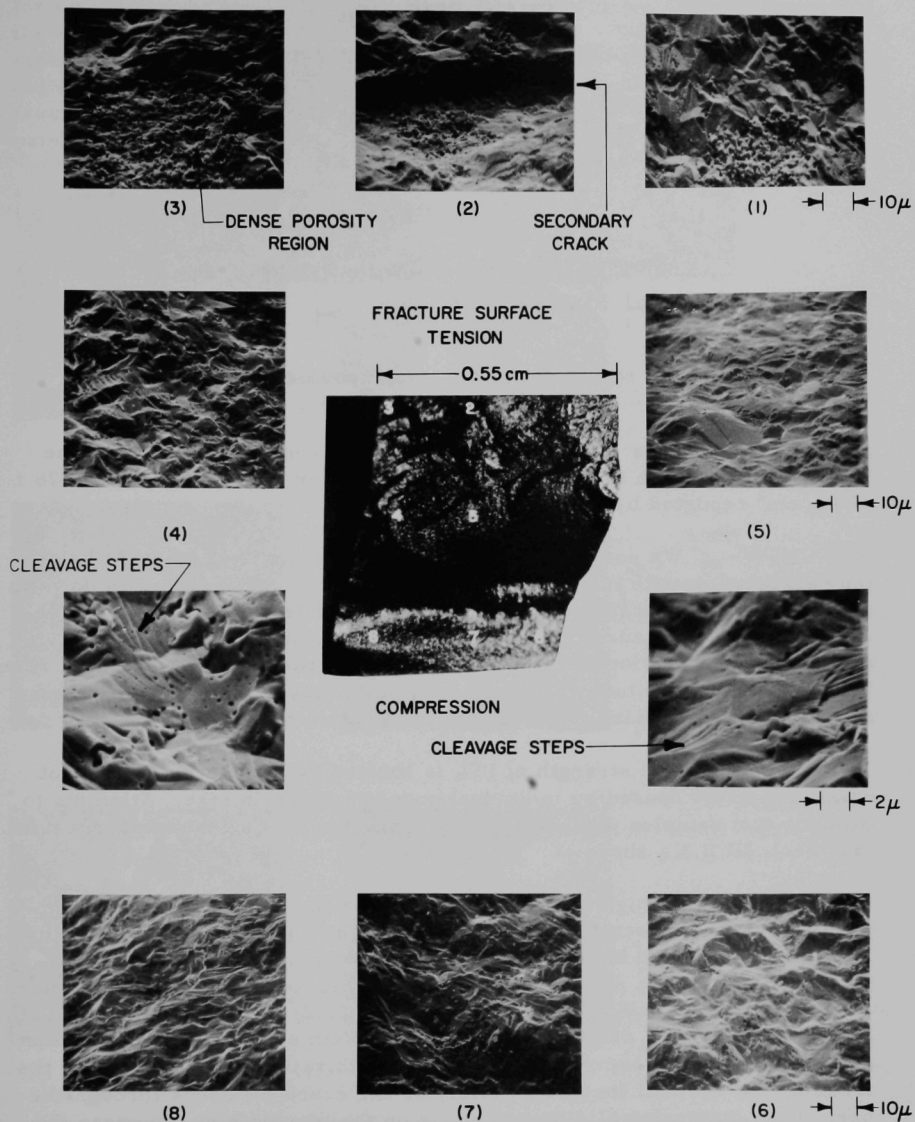


Fig. III.B.12. Scanning-electron Fractographs of a UO_2 Sample (grain size, 8μ ; 97% TD) Fractured at 500°C and a Strain Rate of 9.2/hr

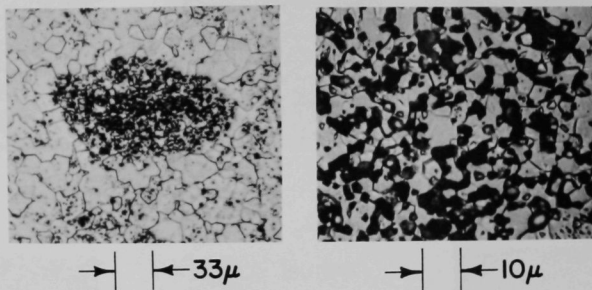
GRAIN SIZE, 15μ 

Fig. III.B.13. "Freckle" on Polished, Etched UO_2
Sample. Grain size is 15μ .

and Davidge's values. They measured strengths of $\sim 1400 \text{ kg/cm}^2$ in the brittle region, which is approximately 30% higher than the value of $1176 \pm 47 \text{ kg/cm}^2$ reported by Canon *et al.**

We conclude, therefore, that the mode of fracture below the brittle-to-ductile transition T_c is the extension of preexisting flaws in the material. The fracture appears to originate from a flaw lying on or close to the tensile surface. The irregular fracture surface might be caused by the direction of fracture joining the cracks emanating from other large flaws close to the projected crack path; thus, the fracture surface should contain a maximum number of fabrication flaws.

The strength of UO_2 is limited by fabrication flaws that mask any effect caused by individual porosity or grain size. Attempts to produce test samples without dense porosity regions have been successful. (See Sect. III.B.3.a above.)

At high temperatures, beyond the second transition temperature, T_t^* (characteristically similar to the equicohesive temperature in metals), the grain boundaries become increasingly weak, and grain-boundary sliding can precede fracture, which is, of course, intergranular. A typical fracture surface ($T = 1800^\circ\text{C}$, $\dot{\epsilon} = 0.92/\text{hr}$) is shown in Fig. III.B.14. Many features, e.g., triple-point voids and grain separation, indicate that some sliding has occurred. The crack growth rate will be slowest on the tension side and will increase rapidly as the crack proceeds through the bar. Thus, extensive sliding can occur on the tension side, whereas the compression side of the sample is subjected to a tensile-stress component

*Canon, R. F., Roberts, J. T. A., and Beals, R. J., High Temperature Deformation of UO_2 , to be submitted to J. Am. Ceram. Soc.

for only a short time. This behavior could account for the appearance of the intergranular fracture shown in Fig. III.B.14. The grains on the tensile side of the fracture surface have a rounded, eroded appearance, which is not exhibited by the grains on the compression side. It is as though the fracture was originally ductile but finally developed a brittle intergranular nature as it built up speed.

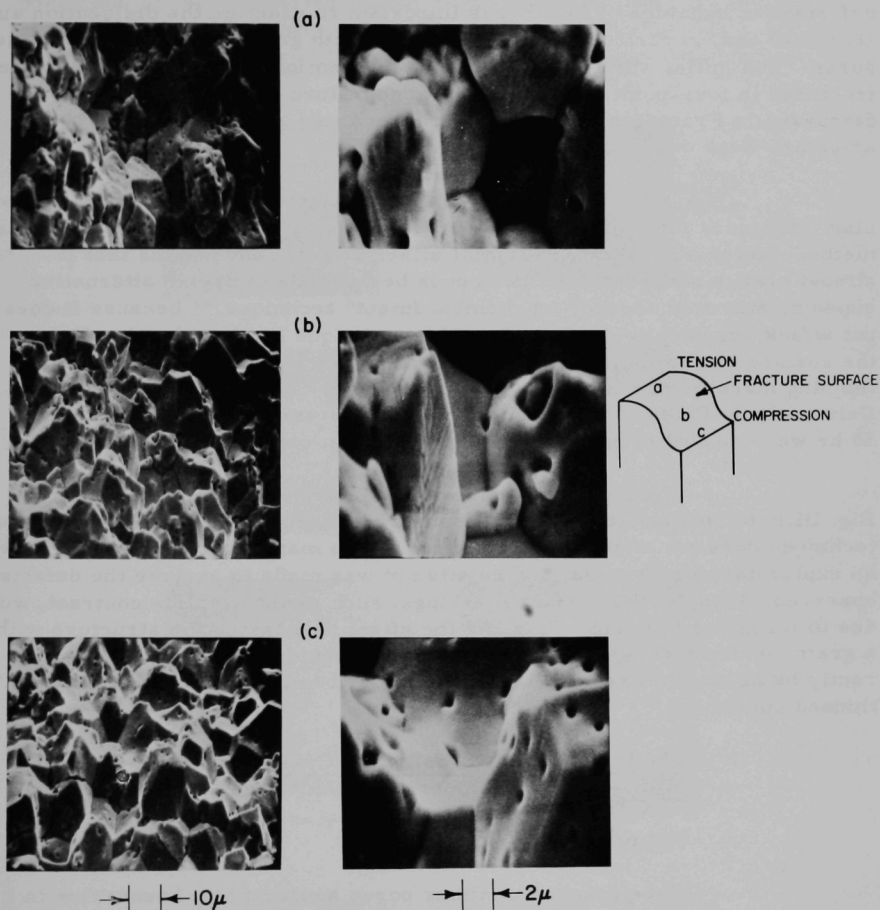


Fig. III.B.14. Scanning-electron Fractographs of a UO_2 Sample (grain size 8 μ ; 97% TD) Fractured at 1800°C and a Strain Rate of 0.92/hr

- (iv) Electron Microscopy of UO_2 (J. T. A. Roberts, L. C. Michels, and A. A. Solomon)

Not previously reported.

To provide a quantitative explanation for the high-temperature deformation behavior of UO_2 ,* it is important to examine the dislocation substructure and, in particular, the interaction with grain boundaries and sinter pores. The initial work will be confined to examining samples that have been fractured in four-point bending in the temperature range 1400-1800°C. As discussed in Fractography of UO_2 [paragraph (iii) above], the grain boundaries are weak and sliding may occur.

L. Michels and G. Dragel have modified the chemical thinning techniques for the preparation of UO_2 foils. One drawback of a chemical method, however, is the preferential attack at grain boundaries that is almost always observed. An attempt is being made to use an alternative experimental method, the "ion-bombardment" technique,** because it does not attack any part preferentially. This technique involves bombarding the surface of a thin disk with argon ions. Since we do not possess an ion thinning machine, the initial tests were made at Case Western Reserve University by Professor A. H. Heuer. The process is slow (for example, 50 hr were needed to prepare the first foil), but can be automated.

The typical transmission-electron micrographs shown in Fig. III.B.15 emphasize the grain-boundary structures. The ion-bombardment technique does not attack the boundaries, since many were evident. This was an exploratory experiment, and no attempt was made to analyze the defects observed. Many of the surface markings, such as the steplike contrast, were due to irregular thinning. This had the effect of masking the structure within a grain and is therefore a drawback of this technique. Attempts are currently being made to resolve this difficulty and to produce more uniformly thinned specimens.

- (v) The Influence of Porosity and Grain Size on the Strength of UO_2 (J. T. A. Roberts, Y. Ueda, and B. J. Wrona)

Not previously reported.

The presence of sinter pores and/or grain boundaries in a ceramic material has a profound effect on both brittle and ductile strength.

*Canon, R. F., Roberts, J. T. A., and Beals, R. J., High Temperature Deformation of UO_2 , to be submitted to J. Am. Ceram. Soc.; Roberts, J. T. A., The Nature of the Activation Volume-Stress Dependence in the High Temperature Plasticity of UO_2 , submitted to J. Nucl. Mater.

Hirthe, W. M., Melville, A. T., and Wackmann, P. H., Rev. Sci. Instr. **38(2), 223-227 (1967); Abrahams, M. S., Buiocchi, C. J., and Coutts, M. D., *ibid.*, **39**(12), 1944-1945 (1968).

A decrease in strength is generally the result of an increase in porosity or grain size. Also, an increase in porosity increases the ductility, but, under some circumstances, a specimen with a fine grain size is more ductile than a specimen with a large grain size. Grain-size effects have received the most attention, since work can be done on fully dense ceramics such as MgO or Al_2O_3 . This precludes any interaction between sinter pores and grain boundaries, which might markedly alter the deformation characteristics. Porosity effects have received less attention, and, in particular, the influence of different pore distributions has not been studied.

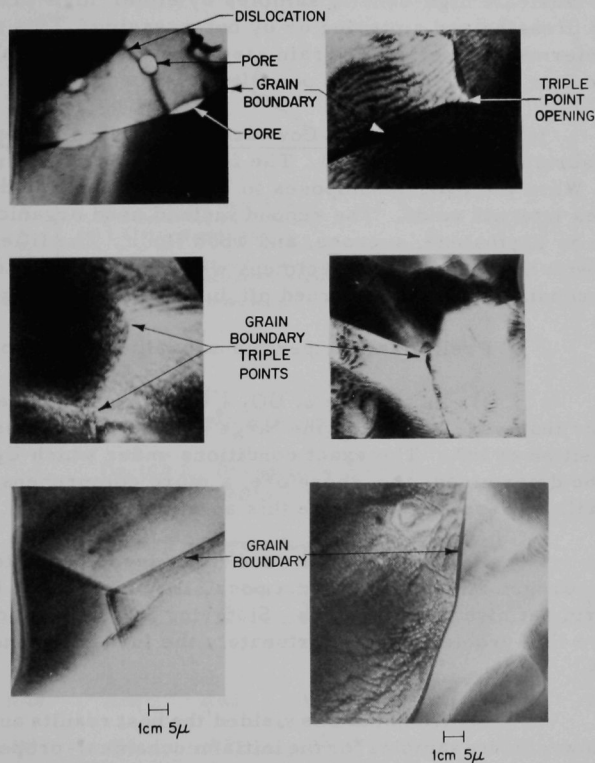


Fig. III.B.15. Transmission-electron Micrographs of a Deformed UO_2 Sample Thinned by Using Ion Bombardment

Nuclear fuel oxides contain both defects. It would be useful if the effects of porosity and grain size could be optimized to produce a fuel that would neither crack extensively during cycling, nor swell much during the steady-state operation of the reactor. With this as an objective, the influence of these defects on the high-temperature strength of UO_2 (and eventually $\text{UO}_2\text{-PuO}_2$) will be systematically examined.

The main problem is fabrication. Generally, an increase in grain size results in an increase in density, and vice versa. Also, recent investigations [see Fractography of UO_2 in paragraph (iii) above] have shown that the brittle strength of UO_2 is limited by fabrication flaws, in this case, regions of dense porosity. Fortunately, a technique has been developed by J. Dusek and A. Solomon that results in a more homogeneous microstructure. This technique provides the basis for the fabrication of the material used in the present program. The first problem was to fabricate controlled low-density samples. Concomitantly, procedures have been instituted to fabricate high-density samples by either high-pressure (100,000 psi) pressing and sintering or by hot-pressing. This material will be used to determine the effect of grain size on strength, and also will provide baseline data for the effects of porosity.

(a) Fabrication of Low-density UO_2 Test Samples. Two methods of fabrication were studied. The first method used a mixture of $\text{UO}_2 + \text{U}_3\text{O}_8$. When the U_3O_8 decomposes to UO_2 , the resulting decrease in volume leaves internal voids. The second method used organic filler materials, such as naphthalene, sucrose, and wood flour. The filler materials were mixed with UO_2 before the specimens were shaped by cold-pressing. The organic substance was then burned off during the sintering process.

Preliminary experiments yielded the following results:

1) A mixture of $\text{UO}_2 + \text{U}_3\text{O}_8$ produced specimens containing cracks that were caused by the large volume change associated with the decomposition of UO_2 . The exact conditions under which U_3O_8 decomposes must be determined, and, therefore, a more comprehensive development stage will be necessary to make this an effective method.

2) Sucrose and wood flour decomposed to carbon when heated in a hydrogen atmosphere, and a possibility exists that UC forms during sintering at high temperatures. Sintering in a CO_2 atmosphere would remove this problem, but unfortunately the furnace cannot be operated with this gas.

3) Naphthalene yielded the best results and will be used to fabricate low-density samples for the initial mechanical-property measurements. Naphthalene powder (<100 mesh) was mixed with UO_2 powder by dry ball milling, and the mixture was fabricated by cold-pressing to either pellets or bars at 12,000 or 25,000 psi. The naphthalene must be burned off early in the sintering process. A thermogravimetric analysis of naphthalene showed that it vaporizes at 75-80°C. Consequently, after UO_2 plus naphthalene green bodies were preheated at 75°C for 5 hr in a hydrogen-atmosphere furnace, the temperature was increased to 1700°C, maintained for 16 hr, and finally cooled to room temperature in one day.

The samples were observed metallographically, and density measurements were obtained. The sample density depends on naphthalene content, as shown in Fig. III.B.16. The graph can now be used as a basis for fabricating test specimens that have densities of 80, 85, 88, and 92% of theoretical which are required for mechanical-property measurements. Some results of the metallographic examination are shown in Table III.B.5. Both grain size and pore size were dependent on naphthalene content, and to a lesser extent on the fabrication pressure.

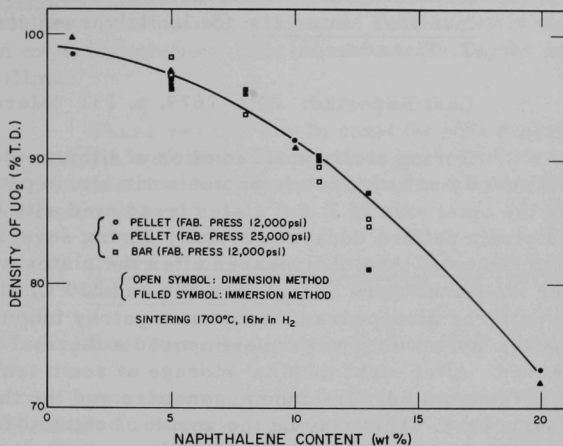


Fig. III.B.16. Dependence of Final Specimen Density on Naphthalene Content

TABLE III.B.5. Metallographic Observation of Low-density Samples

Composition	Sample Numbers							
	N-11	N-12	N-51	N-52	N-101	N-102	N-201	N-202
Naphthalene content, wt %	1	1	5	5	10	10	20	20
Fabrication pressure, psi	12,000	25,000	12,000	25,000	12,000	25,000	12,000	25,000
Sintered density, ^a % TD	98.4	99.0	96.1	97.2	91.6	91.0	73.0	72.0
Average grain size, μ	17	17	13	16	10	11	8	9
Average pore size, μ	1.0 ± 0.4^b	1.2 ± 0.6	1.7 ± 1.2	1.6 ± 0.8	1.8 ± 1.2	1.8 ± 1.0	2.7 ± 2.1	2.8 ± 2.1

^aObtained by immersion method.

^bStandard deviation.

C. Engineering Development--Research and Development

1. Instrumentation and Control

a. Boiling Detector (T. T. Anderson)

(i) Acoustic Method

(a) Irradiation and Resistance Tests of Piezoelectric and Insulator Materials (S. L. Halverson and T. T. Anderson)

Last Reported: ANL-7679, p. 131 (March 1970).

During electron irradiation of lithium niobate in July 1969, a bilaterally antisymmetric photoelastic strain pattern was observed along the optic axis of Z-cut plates irradiated with half the plate shielded. This strain pattern decayed partially during several days' storage at room temperature, then disappeared after the plates were annealed at 140°C. After the plates were annealed to 170 and 220°C, all irradiation-induced strain patterns disappeared; however, a patchy inhomogeneity (not present originally), upon which was superimposed a thermal-stress pattern, was observed. After eight months' storage at room temperature, the specimens were reexamined. The inhomogeneities and the thermal-stress pattern had disappeared. This may be the result of electro-optic effects associated with alterations in charge distribution.

These studies suggest that similar results for non-uniform laser illumination may not be entirely the result of photoexcitation, but also may involve thermal and mechanical stress gradients leading to primary and secondary electro-optic phenomena.

(b) Development of High-temperature Detector (A. P. Gavin, T. T. Anderson, and K. Reimann)

Last Reported: ANL-7705, pp. 152-153 (June 1970).

The stainless steel acoustic sensor has been redesigned, and a new unit is being fabricated. In the new unit, overall diameter is reduced and support rings are eliminated to improve acoustic response. As before, clamping action between crystals and diaphragms will be maintained by a partial vacuum.

Development of a bonded sensor requires that the crystal and the sensing diaphragm be joined metallurgically. A high-temperature waveguide for ultrasonic waves also may require a metallurgical bond. Accordingly, two brazing tests have been performed in the

Materials Science Division. Briefly, X-cut crystals of lithium niobate (1-cm diameter by 0.1 cm thick) with rf-sputtered nickel-over-chromium films on one side, were vacuum-brazed with 72% Ag-18% Cu alloy (decarbonized CUSIL) to a 0.5-in.-dia nickel rod at 780°C brazing temperature. Before sputtering, one crystal was optically polished; the other was smooth-ground at 300 mesh.

After cooling, examination revealed both crystals were cracked perpendicular to the face along a major diameter. Secondary cracks were visible in the polished crystal. Both crystals were darkened, evidently from oxygen depletion. The crystals were easily detached from the sputtered films.

These results are in contrast with a previous brazing of Z-cut lithium niobate with fired electrodes, during which adhesion of the electrodes was maintained to both the nickel rod and to the electrical lead; there was no evidence of cracking.

(c) Tests of High-temperature Detectors in Water, Furnace, and Sodium (T. T. Anderson)

Last Reported: ANL-7669, p. 125 (Feb 1970).

Acoustic calibrations have been performed on the stainless steel-encased sensor and brass-encased sensor at the Underwater Sound Reference Division (USRD) of Naval Research Laboratory. The stainless steel sensor (previously tested at Argonne to 1200°F in air) had no acoustic sensitivity. Loss of sensitivity was traced to a cleaning operation performed with glass beads at Argonne. Evidently, the glass beads impinged on the sensor diaphragms and warped them out of contact with the lithium niobate assembly.

The brass sensor had a smooth response at low frequencies, with a major resonance at 8 kHz. Lower resonances were observed to 125 kHz. The staff at USRD made a number of recommendations for improvement of the design.

(d) Design of Prototype Boiling-detection System (P. Wang)

Not previously reported.

Waveguides for transmitting acoustic emissions from boiling are under investigation as an alternative approach to the use of high-temperature acoustic sensors. A propagation spectrum of acoustic waves has been calculated from the mechanics equations for determining natural frequencies of the rod.

A one-dimensional propagation of waves in terms of the mechanical impedance is also being investigated. A computer program has been written for impedance; it includes transmission through a rod of variable cross section and transmission into a medium from the end of a circular rod.

2. Engineering Mechanics (G. S. Rosenberg)

a. Structural Dynamics Studies--Structure-Fluid Dynamics (M. W. Wambsganss, Jr.)

(i) Near-field and Far-field Flow Noise

Last Reported: ANL-7705, p. 159 (June 1970).

Pressure-time histories from a second series of flowtests designed to study the near-field component of flow noise as a source of structural excitation are being analyzed. These tests were performed over a range of water velocities (10-60 ft/sec) in the small test loop.

The low-frequency behavior of the mean-square noise spectra is obtained by working with pressure differentials from a pair of diametrically opposite miniature transducers flush-mounted on a tubular test element in the loop. This technique serves to nullify the contribution from the far-field (acoustic) noise.* Figure III.C.1 shows a typical set of mean-square spectra corresponding to various mean axial flow velocities. The pressure peak exhibited by the curves occurs at the natural frequency of the instrumented test element; it is caused by a slight bending strain in the element, which is sensed by the transducers and doubled in the subtraction process. In general, the curves are relatively flat out to a cutoff frequency, with the intensity and cutoff frequency increasing with mean flow velocity.

As with data from previous flowtests reported in ANL-7685* and ANL-7705, a Strouhal-number representation of frequency satisfactorily normalized the spectra with respect to frequency, while the intensity scaled with the square of the mean flow velocity. The normalized spectra are shown in Fig. III.C.2.

The rationale for scaling with the square of the flow velocity is as follows: The conventional method for normalizing the mean-square spectra, i.e., assuming that the rms-pressure coefficient is constant, and scaling with the cube of the flow velocity, tended to overcorrect spectra

*Wambsganss, M. W., and Zaleski, P. L, Measurement, Interpretation, and Characterization of Near-field Flow Noise, Flow-Induced Vibrations Conference Proceedings, ANL-7685 (to be published).

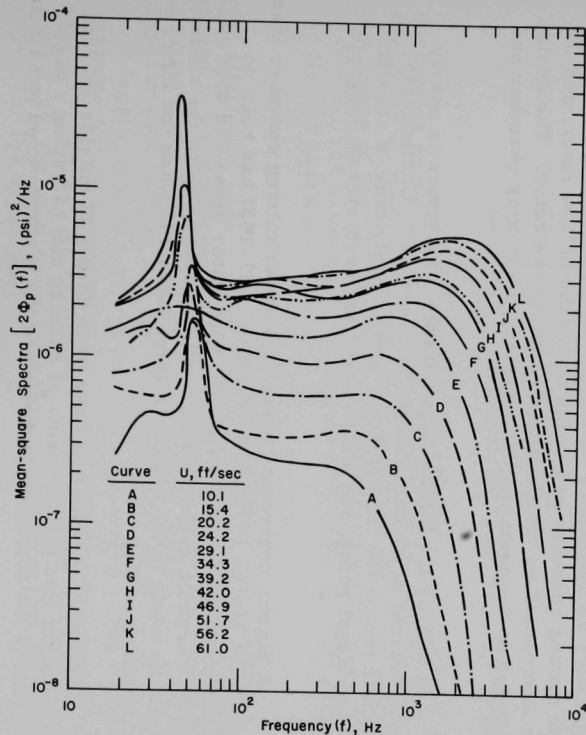


Fig. III.C.1. Family of Near-field Mean-square Spectra
 Sketched from Experimental Plots

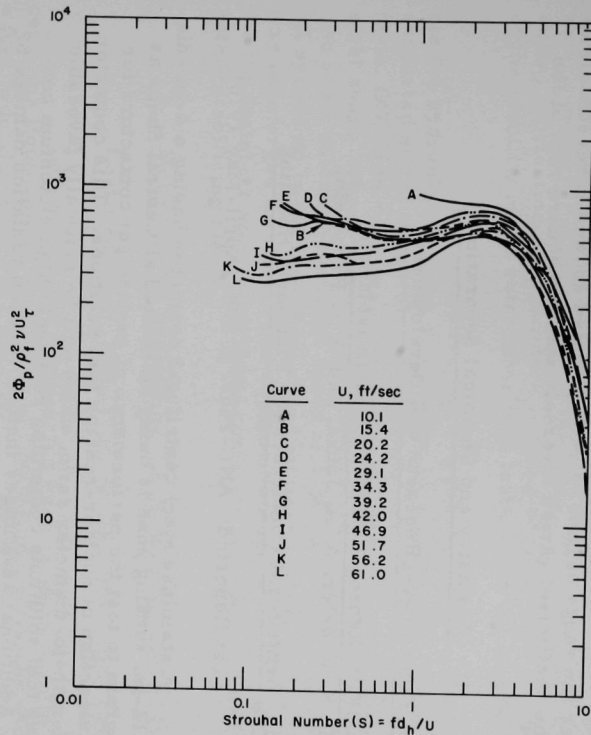


Fig. III.C.2. Normalized Near-field Mean-square Spectra;
 ρ_f = fluid density, v = fluid velocity, U =
 friction velocity, d_h = hydraulic diameter

associated with the lower flow velocities. A closer look at the rms-pressure coefficient over the range of flow velocities tested showed it reasonable to assume that the coefficient varied inversely with the square root of the velocity.

D. Chemistry and Chemical Separations

1. Fuel Cycle Technology--Research and Development

a. LMFBR Reprocessing: Plutonium Isolation (D. S. Webster, A. A. Jonke, and G. J. Bernstein)

(i) Centrifugal Contactors for Plutonium Handling

Last Reported: ANL-7688, p. 208 (April-May 1970).

A stainless steel centrifugal contactor having a 4-in.-dia rotor with a 12-in. settling zone is being fabricated at Central Shops as part of a program to test the performance of centrifugal contactors for the solvent extraction of nuclear-reactor fuel solutions. This contactor has a large length-to-diameter ratio, which will be critically favorable for processing fuel solutions containing relatively high plutonium concentrations. Additional advantages include reduced radiation damage to the solvent and increased ease of operation. The contactor has the same general configuration as contactors developed and operated by Savannah River; i.e., the mixing chamber is located below the hollow rotor, and the mixing paddle is mounted on the shaft that supports the rotor. The design allows modification of the contactor by replacing the mixing chamber and paddle.

A facility for testing experimental contactors is nearly completed, and checkout of its components is under way. Components include an electric motor for the contactor and a supply tank, a constant-head tank, a centrifugal pump, and a flowmeter for each stream (organic and aqueous).

A plastic contactor having an annular mixing chamber (see Progress Report for March 1970, ANL-7679, pp. 137-138) has been designed. The performance of the plastic unit with water alone and with two-phase aqueous and organic systems will provide guidance as to the kinds of tests that should be made in the stainless steel contactor when the latter is operated with annular mixing.

Informal discussions have been held with outside sources to gain further insight into the problems of running and balancing a high-speed rotor. Among the topics discussed were the methods used to calculate

the critical speed of a rotor and the allowable runout (deviation from true axial symmetry) at the bottom of the rotor. The rotor will be balanced during fabrication. A procedure is being developed for stepwise testing of the stability of the rotor after it is installed in the test facility.

In our application, a test assembly has been used to evaluate the hydraulic damping of vibration by a cylindrical sleeve at the unsupported end of the rotor. A relatively heavy brass stabilizer ring (3-in. OD, $1\frac{1}{2}$ in. high) was attached to the end of a $1\frac{1}{2}$ -in.-dia, $11\frac{1}{2}$ -in.-long steel shaft. When rotated in air, the assembly developed excessive vibration at its calculated critical speed of 2100 rpm, but rotated smoothly at all speeds up to the maximum speed attainable (3300 rpm) when the ring was submerged in water. The design of the mixing paddle being fabricated for the stainless steel centrifugal contactor is being modified to incorporate a stabilizing sleeve.

b. Molten Metal Decladding (D. S. Webster and R. D. Pierce)

Last Reported: ANL-7705, pp. 161-163 (June 1970).

Laboratory and engineering work is being done to develop concepts for liquid-metal decladding of LMFBR fuel elements with and without a fuel reduction step. The concepts are expected to be applicable also to the removal of Zircaloy cladding from light-water-reactor fuels.

(i) Engineering Development

Last Reported: ANL-7705, pp. 162-163 (June 1970).

(a) Gas-release experiments. As the first phase of the decladding process, cropped fuel subassemblies will be lowered into the decladder so that the fuel elements penetrate the cover salt and the bottom few inches of the fuel elements are immersed in the zinc. The system is at 800°C. The cladding at the bottom of the fuel elements dissolves, and the fission gases are vented.

Initial experiments have been completed to simulate the effect of a sudden release of gas under pressure, as would be experienced in a decladding operation. Zinc and salt were contained in a graphite crucible with an Amersil crucible as a secondary. In each of two experiments, a Type 304 stainless steel tube (0.25-in. OD, 10-mil wall, 5-in. length) having a steel capillary tube sealed to one of its ends with a Swagelok fitting was pressurized to 6.8 atm by feeding argon through the capillary. Three UO₂ pellets (0.21-in. diameter, 0.25-in. length) were inserted into the tube in one of the runs; in the other run, the tube was empty except for the argon gas.

The individual tubes were immersed 1 in. into a molten-zinc bath below a 1/4-in. salt cover at 800°C. Calculations indicate that the pressure within the tubes increased to about 15 atm after immersion of the tubes. Gas release from the tubes was observed after 2.75 and 2.5 min. Examination of the tubes after the experiments showed that 1 in. of the stainless steel tube had been dissolved with no apparent expansion of the tube adjacent to the molten zinc-salt interface. The Amersil secondary crucible contained about 40 g (0.7% of charge) of zinc and salt that had been ejected from the graphite crucible during the gas release. Although the freeboard in the graphite crucible was 3 in., metal and salt had splashed to a height of about 5 in.

(ii) Process Demonstration Experiments

Last Reported: ANL-7705, p. 163 (June 1970).

(a) Semiworks Experiment. Work to develop engineering-scale decladding equipment included an experiment (see Progress Report for April-May 1970, ANL-7688, p. 211) using a basket with a cylindrical, tantalum shroud. The basket, containing 950 g of Type 304 stainless steel tubing and 500 g of UO_2 pellets, was immersed in 65.5 kg of zinc and 3.0 kg of cover salt at 800°C for 2.5 hr; the melt was agitated at 300 rpm with a 3.5-in.-dia impeller. Additional analytical results for that experiment indicate that no UO_2 was lost in the zinc decladding solution and that 89% of the iron was dispersed in the zinc solution, 11% of the iron being retained as sludge in the basket with the pellets.

(b) Irradiated-fuel Experiments. Detailed operating procedures are being written for a planned series of four decladding experiments with individual irradiated fuel elements (see Progress Report for March 1970, ANL-7679, p. 139). Each stainless steel-clad fuel element contains about 80 g of pressed and sintered pellets having a composition of UO_2 -20% PuO_2 . The fuel elements were irradiated in EBR-II to an approximate burnup of 3%, and have been cooled for more than one year. The estimated activity in each pin is about 200 Ci. All proposed chemical and mechanical steps are being verified in experiments with unirradiated material.

(iii) Behavior of Volatile Fission Products

Last Reported: ANL-7688, pp. 211-212 (April-May 1970).

In the present concept of decladding by use of liquid metal, some iodine (that present in elemental form) in the annular and plenum regions of irradiated fuel elements will be liberated when the cladding is dissolved in liquid zinc at 800°C. Three experiments were conducted to investigate the zinc-iodine reaction by bubbling argon, containing labeled

iodine, through a pool of molten zinc. For each experiment, a standard consisting of an aliquot of the tracer solution was counted, along with aliquots of materials taken from the reaction train at the end of the experiment, to allow calculation of the amount of iodine that had reacted with the zinc.

In two experiments, iodine (0.1 to 0.2 at. % in argon) was released at rates of 65 or 150 ml/min below the surface of molten zinc (at 800°C). Bubbles were released 17 and 10 cm below the surface of the zinc (covered with about a 2-cm layer of LiCl-KCl); 99.999+ % of the iodine reacted with the zinc and accumulated in the cover salt, indicating that the decontamination factor was at least 10^5 . In the third experiment, bubbles (0.2 at. % iodine in argon) were introduced 3 cm below the zinc surface at 150 and 300 ml/min; 99.996% and 99.985%, respectively, of the iodine reacted and was recovered in the salt, indicating that complete reaction was not achieved with the 3-cm-deep pool tested in this experiment.

c. LMFBR Fuel Materials Preparation--U/Pu Nitrates to Oxides
(A. A. Jonke and N. M. Levitz)

Last Reported: ANL-7705, pp. 163-165 (June 1970).

Continuous denitration of uranium-plutonium nitrate solutions or plutonium nitrate solutions to produce powdered fuel oxides suitable for the fabrication of fuel shapes is to be demonstrated in fluid-bed equipment. Current processes for converting LWR fuel to oxide consist of a number of steps, including precipitation, filtration, and calcination. Problems of nuclear criticality and self-radiation from plutonium in solution (resulting in gas formation) are encountered in processing LMFBR fuels. This provides an incentive for developing continuous fluid-bed denitration, which promises the advantages of a large capacity, a relatively low plutonium holdup, and rapid conversion to solids.

(i) Pilot-plant Program. A fluid-bed pilot plant (see Progress Report for December 1969, ANL-7655, p. 118) has been constructed to study the effects of variables in the continuous denitration of uranium-plutonium solutions. The zone of the denitrator where the nitrate solution is denitrated in a fluidized bed of oxide consists of a 4-in.-dia pipe with a cone-shaped gas distributor at the base. In the present equipment setup, the spray nozzle for atomizing the nitrate feed solution is 9 in. above the cone. The air and solution streams mix as they enter the denitrator. A pipe for oxide product overflow into the product receiver is positioned 12 in. above the cone and on the side opposite the nozzle. Two porous, metal filters, located in the upper chamber of the denitrator, are blown back alternately at 20-min intervals for durations of 0.5 sec.

Four preliminary denitration experiments (U-1 through U-4) with uranyl nitrate solutions have been completed to demonstrate denitrator operation. In each run, the starting bed (~7 kg) was UO_3 containing 800 ppm sulfate and having a bulk density of 4.2 g/cc and a mean particle diameter (MPD) of 162 μm . In all four runs, denitration was carried out at 300°C.

The operating procedure was as follows: The equipment was leak-checked. Then a low rate of airflow was started through the process equipment train, and the denitrator was heated. Prior to addition of the starting bed, the airflow rate was increased so that the bed material would be fluidized, and airflows were started through the product discharge line into the denitrator and through the liquid and air chambers of the spray nozzle to prevent the starting-bed material from leaving the denitrator through the product line or nozzle. Heating of the bed was continued, and first water and then uranyl nitrate solution were substituted for the air passing through the liquid chamber of the spray nozzle.

In each experiment, the starting and final beds were sampled and their particle-size distribution determined. Also, oxide overflowing to the product receiver was removed at half-hour intervals and weighed, and the particle-size distribution of these product samples was measured.

Values of important operating conditions are summarized in Table III.D.1. The uranium nitrate molarity and the solution feed rate were increased in turn until a solution feed rate of 100 ml/min for 2.4M uranyl nitrate solution was achieved in U-4. This corresponds to a production rate of 100 lb $\text{UO}_3/(\text{ft}^2)(\text{hr})$, the design rate.

TABLE III.D.1. Operating Conditions, Denitration Runs

	U-1	U-2	U-3	U-4
Uranyl nitrate molarity	1.0	1.0	1.0	2.4
Uranyl nitrate solution feed rate, ml/min	50	100	75-100	60-100
Fluidizing air velocity, ft/sec	1.0	1.0	1.5	1.5

The durations of U-1, -2, -3, and -4 were 3, 2/3, 10, and 14 hr. A 14-hr run is considered very satisfactory at this early stage of equipment operation.

A major unsolved problem is control of product particle size and particle agglomeration. The second run was ended because a plug

formed in the bed, and the third run was ended because of a plug in the product overflow pipe. Also undesirable was the production of a large quantity of -200 mesh UO_3 near the end of U-4.

The final beds from U-1, -3, and -4 contained 10, 11, and 17% of large particles (+20 mesh and agglomerated pieces). The large pieces might have formed by agglomeration at the nozzle or on the interior walls of the denitrator. (No particles were found on the denitrator wall upon inspection at the end of these runs.) When the final beds were removed, difficulty was experienced in removing UO_3 agglomerates through the bottom drain opening of the denitrator.

The present objective is to control the particle size of the product oxide by adjusting operating conditions.

d. LMFBR Fuel Fabrication--Analytical Development and Continuous Processing (A. A. Jonke and M. J. Steindler)

Last Reported: ANL-7688, pp. 214-215 (April-May 1970).

Analytical techniques are being studied for measuring the preirradiation properties of reactor fuel that are strongly related to fuel performance in reactors.

(i) U/Pu Ratio in Fuel. Determination of the U/Pu ratio is a part of any conceivable fabrication procedure for UO_2 -Pu O_2 fuel. For example, the specification for FFTF is that a core zone must have an average plutonium content of $20.0 \pm 0.1\%$. This imposes a precision of $\pm 0.5\%$ (relative standard deviation without bias).

X-ray fluorescence analysis is being evaluated in this work as an in-line analytical method. At other sites, X-ray fluorescence analysis of (U,Pu) nitrate solutions (both inactive solutions* and process streams** containing radioactivity) has been performed. The relative standard deviation, taking the background count into account, for solutions containing up to 10 mg U/ml and 3.5 mg Pu/ml was observed to approach $\pm 0.6\%$. To attain the desired precision of analysis of solid oxide (powder or pellets), matrix effects due to high absorption coefficients, crystallite size, scattering by voids and surface roughness, and enhancement (secondary fluorescence) must be proved to be insignificant or measurable.

Th O_2 -U O_2 is being used as a stand-in for UO_2 -Pu O_2 because the relationship of the atomic numbers for thorium and uranium is identical

*Ertel, D., Simultaneous Determination of Uranium and Plutonium by X-ray Fluorescence, J. Radioanal. Chem. 2, 205-209 (1969).

**Wickmann, H. P., DeCarolis, M., Mongon, A., and Eschrich, H., NP-16417 (EIR-123) (1966).

to the relationship for uranium and plutonium (ANL-7655, p. 119); i.e., the relationships of the absorption coefficients, absorption edges, X-ray emission spectra, and fluorescence yields for the members of one pair are similar to these relationships for the members of the other pair. Pure UO_2 is being prepared from NBS standard U_3O_8 for subsequent mixing with ThO_2 . The mixture will be used in studying the influence on fluorescence intensity of variables related to solids analysis.

Instrumental choices and sample presentation procedures must be defined. Because the greatest loss of fluorescence intensity due to instrument effects is attributable to the fraction lost in collimation, a series of experiments was performed with a Norelco spectrometer* and different collimators. Ratemeter scans were obtained for various combinations of collimators having spacings of 5, 20, and 125 mils, using a sample of 20% UO_2 -80% ThO_2 . A LiF diffraction crystal was used along with an X-ray tube (with tungsten target) operated at 45 kVp and 11 mA with a 3/8-in. mask. The goal was to increase precision within a fixed assay time by increasing the counting rate of each fluorescence peak.

Using collimators with 20-mil spacing resulted in a ten-fold increase in count rate over that obtained with 5-mil collimator spacing. As anticipated, there was some decrease in peak resolution (the peak widths at half-height increased threefold). However, this peak resolution was adequate for analysis. Some increase in background occurred, but this was not statistically significant. A threefold improvement in precision was therefore obtained with the 20-mil collimator spacing. The latter spacing will be used for future experiments. The X-ray tube will be operated at 59 kVp and 41 mA, which should give count rates for uranium of about 10^4 cps and should provide adequate precision at counting times of about 20 sec.

2. General Chemistry and Chemical Engineering--Research and Development

a. Thermophysical Properties (A. D. Tevebaugh and P. E. Blackburn)

(i) Partial Pressures of Vapor Species in the U-Pu-O System and in the U-Pu-O System Containing Fission Products

Last Reported: ANL-7679, pp. 142-145 (March 1970).

Mass-spectrometric studies of the volatilization behavior of the uranium-plutonium-oxygen LMFBR fuel are being performed to determine (1) the composition of the vapor phase in equilibrium with the condensed phase(s), (2) the partial pressures of the vapor species as a

*The Norelco X-ray spectrometer uses a collimator between the sample and the crystal and another collimator between the crystal and the detector.

function of temperature and oxygen concentration, and (3) the thermodynamic properties of the vapor species. These data are required to establish whether migration occurs within the fuel by vapor transport, and to determine metal and oxygen activities of the fuel. These activities are important in determining the nature of fission products (i.e., their presence as oxides, alloys, or elements), particularly those corrosive to cladding or those contributing to fuel swelling. The data will be used to establish methods for controlling cladding attack and some aspects of fuel swelling. The program will first concentrate on the pure fuel, i.e., $(U_{0.8}Pu_{0.2})O_{2-x}$, corresponding to zero irradiation. Simulated irradiated fuel containing fission products will then be studied.

Studies of the volatilization behavior of the mixed oxide $(U_{0.8}Pu_{0.2})O_{2-x}$ in the range from 1905 to 2411°K and for $1.92 \leq O/M \leq 2.00$ have been completed. The experimental data were previously reported in ANL-7679 and in the Progress Report for December 1969, ANL-7655, pp. 120-123. Briefly, the results demonstrated that uranium is preferentially vaporized when the O/M ratio is greater than ~1.93; at an O/M ratio of ~1.92, the U/Pu ratios in the solid and vapor phases are about equal. The total vapor pressure (at constant temperature, 2241°K) decreased by almost a factor of 10 as the O/M ratio of the solid decreased from 2.00 to 1.92. The partial enthalpies of vaporization did not significantly vary as a function of the O/M ratio. The values are 123.43 ± 1.69 , 139.41 ± 1.81 , 146.25 ± 1.67 , and 158.47 ± 1.98 kcal/mol for $PuO(g)$, $PuO_2(g)$, $UO_2(g)$, and $UO_3(g)$, respectively. Also, the partial pressures of $PuO(g)$, $PuO_2(g)$, $UO_2(g)$, and $UO_3(g)$ were determined at 2241°K, and when these data are combined with the partial enthalpies, the partial pressures of the vapor species can be calculated as a function of both temperature and O/M ratio. The partial pressures at the solid composition O/M = 1.96 were used to calculate the following equations for the temperature range 1905-2411°K:

$$PuO(g): \log P(\text{atm}) = \frac{-26,970 \pm 370}{T} + 6.000 \pm 0.190; \quad (1)$$

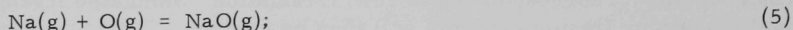
$$PuO_2(g): \log P(\text{atm}) = \frac{-30,470 \pm 400}{T} + 7.060 \pm 0.210; \quad (2)$$

$$UO_2(g): \log P(\text{atm}) = \frac{-31,960 \pm 360}{T} + 9.140 \pm 0.190; \quad (3)$$

$$UO_3(g): \log P(\text{atm}) = \frac{-34,630 \pm 430}{T} + 9.280 \pm 0.220. \quad (4)$$

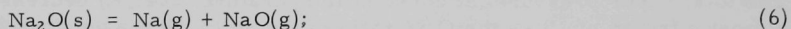
A paper entitled "A Mass Spectrometric Investigation of the Volatilization Behavior of $(U_{0.8}Pu_{0.2})O_{2-x}$ " will be published in Plutonium 1970: Proceedings of the Fourth International Conference on Plutonium and Other Actinides, October 1970.

Further studies of the uranium-plutonium-oxygen system have been temporarily discontinued, and efforts are currently being directed toward studies of the sodium-fuel reaction. In particular, the studies are being directed toward the determination of the oxygen and sodium partial pressures (activities) of the sodium-mixed oxide reaction products [e.g., Na_3UO_4 , Na_3PuO_4 , or $\text{Na}_3(\text{U,Pu})\text{O}_4$]. Preliminary experiments with $\text{Na}_2\text{O-UO}_2$ indicate that the vapor species are $\text{Na}(\text{g})$, $\text{Na}_2(\text{g})$, $\text{NaO}(\text{g})$, $\text{Na}_2\text{O}(\text{g})$, and $\text{O}(\text{g})$. Thus, from the dissociation of such compounds as Na_3UO_4 and Na_3PuO_4 , the oxygen partial pressure can be determined via the equilibrium reaction



$$4.576T \log P(\text{O}) = \Delta F_f^\circ(\text{NaO}) - \Delta F_f^\circ(\text{Na}) - \Delta F_f^\circ(\text{O}) \\ + 4.576T[\log P(\text{NaO}) - \log P(\text{Na})]. \quad (5a)$$

The partial pressures of $\text{Na}(\text{g})$ and $\text{NaO}(\text{g})$ can be determined mass-spectrometrically, and the free-energy data for $\text{Na}(\text{g})$ and $\text{O}(\text{g})$ are well known. However, the data for $\text{NaO}(\text{g})$ have not been well established, but may be obtained through the reaction



$$\Delta G_f^\circ(\text{NaO}) = -4.576T[\log P(\text{Na}) + \log P(\text{NaO})] + \Delta G_f^\circ(\text{Na}_2\text{O}) - \Delta G_f^\circ(\text{Na}). \quad (6a)$$

The dissociation of sodium tungstate (Na_2WO_4) provides an alternative method for obtaining $\Delta G_f^\circ(\text{NaO})$ which may be used as a check on the data obtained from Eq. 6. Reliable data for $\text{NaO}(\text{g})$ then permit the determination of oxygen partial pressures via Eq. 5a for any of the sodium compounds formed in the sodium-mixed oxide reaction (phase-diagram studies performed in another portion of this program will identify the sodium-mixed oxide reaction products). Knowledge of the oxygen partial pressures of the sodium compounds and the mixed oxides (as a function of O/M ratio and temperature) will then enable us to predict reliably the conditions of nonreactivity for the sodium-mixed oxide fuel.

PUBLICATIONS

A New Concept for Liquid Metal-Steam Generators Utilizing Thermal Convection Tubes

D. M. France and Michael Petrick

Nucl. Eng. Design 12(2), 269-276 (May 1970)

Theories of Swelling and Gas Retention in Ceramic Fuels

B. R. T. Frost

Nucl. Appl. Technol. 9(2), 128-140 (August 1970)

Some Considerations of the Behavior of Fission Gas Bubbles in Mixed-Oxide Fuels

C. Y. Li, S. R. Pati, R. B. Poeppel, R. O. Scattergood, and R. W. Weeks
Nucl. Appl. Technol. 9(2), 188-194 (August 1970)

Analysis of Fission Product Ingots Formed in Uranium-Plutonium Oxide Irradiated in EBR-II

D. R. O'Boyle, F. L. Brown, and A. E. Dwight
J. Nucl. Mater. 35(3), 257-266 (1970)

IV. NUCLEAR SAFETY RESEARCH AND DEVELOPMENT

A. LMFBR Safety--Research and Development1. Coolant Dynamics (H. K. Fauske)a. Sodium Superheat (R. E. Henry, R. E. Holtz, and R. M. Singer)

Last Reported: ANL-7669, p. 138 (Feb 1970).

(i) Incipient-boiling Tests with EBR-II Sodium. The principal objectives of this work are (1) to extend the previous sodium-superheat work by using sodium from the EBR-II reactor as the test fluid and (2) to obtain data using magnetic pressurization techniques so that the sodium-superheat modeling technique can be further refined. Another objective of this work is to approach boiling both by adding heat and by depressurization to determine if the approach to boiling influences the incipient-boiling superheat.

All the previous sodium-superheat tests have used laboratory-type sodium as the test fluid and have used heating techniques to obtain superheated sodium. However, since the effects of sodium purity and irradiation upon incipient-boiling sodium superheats are not clearly established, it is desirable to obtain sodium-superheat data with sodium from a reactor to establish whether the sodium-superheat modeling techniques* may be applied to reactor sodium. Also, it is necessary to determine if the approach to boiling influences the incipient-boiling superheats; hence, sodium-superheat data are needed where the approach to boiling is by depressurization.

The agreement between data** and the sodium superheat model* is rather poor at lower pressures ($P < 5$ psia). This disagreement may have been caused by not knowing the partial pressure of inert gas in the surface cavities, and assuming it to be zero. Using electromagnetic pressurization techniques enables the partial pressure of inert gas in the surface cavities to be made equal to zero, and the utility of the sodium superheat model at low pressures can be established.

A new sodium-superheat test vessel is being constructed. Heat will be supplied to the sodium by resistance-type heating wire wrapped around the lower region of the test vessel. The system pressure may be supplied by the E-M pump or by using an argon cover gas. Thermocouples will be located in the tube wall, in the liquid sodium, and in the gas and/or

*Holtz, R. E., The Effect of the Pressure-Temperature History upon Incipient-boiling Superheats, ANL-7184 (June 1966).

**Holtz, R. E., and Singer, R. M., On the Superheating of Sodium at Low Heat Fluxes, ANL-7383 (Nov 1967); Holtz, R. E., and Singer, R. M., A Study of the Incipient Boiling of Sodium, ANL-7608 (Oct 1969).

vapor blanket, so the necessary temperature measurements can be obtained. The pressure in the liquid sodium will be measured by employing a piezoelectric-type pressure transducer, and the pressure in the gas and/or vapor space will be measured by either a Bourdon-type pressure gauge or a U-Tube manometer. Instrumentation for these tests include several two-pen recorders, an oscillograph, and a number of voltage- and current-measuring devices.

b. Liquid-Vapor Dynamics (M. A. Grolmes and H. K. Fauske)

Last Reported: ANL-7669, p. 139 (Feb 1970).

(i) Liquid-film Thickness and Breakup. Experiments have been carried out with Freon refrigerant 11 and 113 in precision-bore glass tubes with 5- and 8-mm inside diameters. The liquid was uniformly superheated (10-90°F) by slow depressurization. Vapor nucleation in the superheated liquid was triggered by a filament wire at the base of the tube as indicated in Fig. IV.A.1. The displacements of the liquid and the vapor bubble were photographed at ≈ 2000 frames per second. The velocity of the liquid free surface and the velocity of the vapor bubble were determined from the displacement data. Since the liquid film drainage is small, the vapor volume fraction α is equal to the ratio of the liquid free surface to vapor bubble velocity. This information and the corresponding liquid fraction (1 - α) and liquid film thickness data are also shown in Fig. IV.A.1. The results shown in Fig. IV.A.1 are typical of the data obtained thus far. For each event, the liquid fraction tends to decrease toward an asymptotic value. It also appears that for most events a value for the liquid fraction

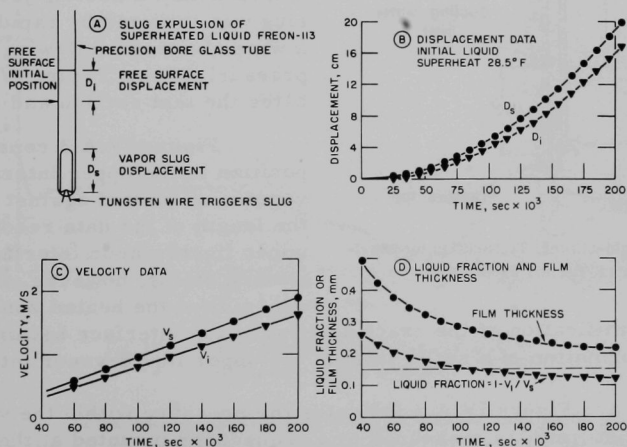


Fig. IV.A.1. Illustration of Film-thickness Measurements for Slug Expulsion

$(1 - \alpha)$ of approximately 0.15 can be used to estimate the film thickness for large fraction of the expulsion event. It can be alternately stated that this result indicates that the ratio of the liquid to vapor bubble velocity approaches a value of ≈ 0.85 . This is quite similar to the ratio of the average to maximum velocity in the liquid alone for fully developed turbulent flow in a circular tube. It appears that the bubble velocity and film thickness may be determined to a large extent by the centerline velocity in the liquid slug. This has also been noted for the different case of steady multibubble two-phase slug flow* for low viscosity liquids in turbulent flow. These studies are continuing. It is anticipated that these results will be directly applicable to liquid metal slug ejection phenomena.

c. Sodium Simulations (M. A. Grolmes and H. K. Fauske)

Last Reported: ANL-7655, pp. 128-131 (Dec 1969).

(i) Transient Flow Regime Studies, Expulsion and Reentry in Single Pin Geometries. Experimental data, ranging in initial superheats from 10 to 50°F, were obtained for the slug expulsion and reentry of

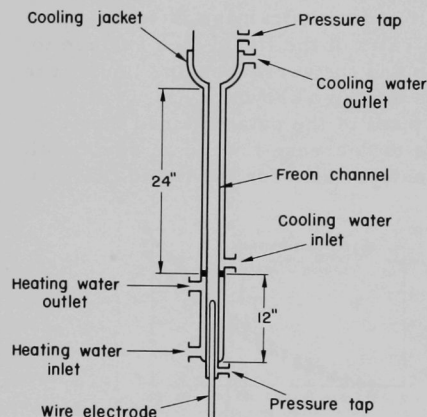


Fig. IV.A.2. Single-channel Test Section for Expulsion and Reentry Experiments

Freon-113. The expulsions were performed in single-channel glass test sections, 7.0- and 4.4-mm ID, consisting of a constant-diameter tube and a variable-diameter plenum. The plenum and upper portion of the test section were provided with a cooling jacket; the bottom was enclosed within a heating jacket. The slug was initiated by rapidly heating a wire electrode following a slow depressurization. Figure IV.A.2 indicates the test section and electrode.

Figure IV.A.3 represents the position of the upper interface of the vapor slug plotted against time. For the length of the data recorded, the upper liquid-vapor interface remained stable; however, as the slug approached the heated zone during

reentry, identification of the exact position of the interface became difficult due to the formation of a heavy mist at the upper liquid-vapor interface.

Figure IV.A.4 indicates the pressure within the vapor space plotted against time, as measured by a transducer mounted at the bottom of

*Griffith, P., Slug Flow in Vertical Pipes, M.I.T. Special Summer Program. Griffith, P., and Gouse, S. W., Jr., ed. (July 1964).

the test section. The large pressure spike corresponds to a total collapse of the vapor space; however, this pressure spike may or may not occur, depending upon both the position of bubble nucleation and initial superheat.

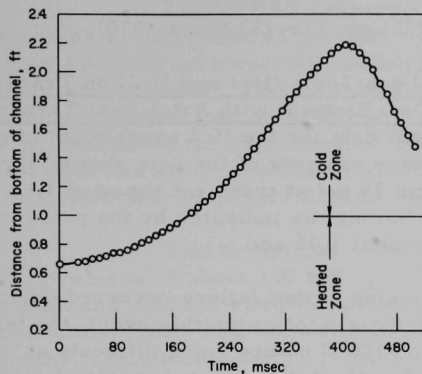


Fig. IV.A.3
Vapor Slug Displacement for Run 61770-4
(Freon-113; initial superheat = 28°F)

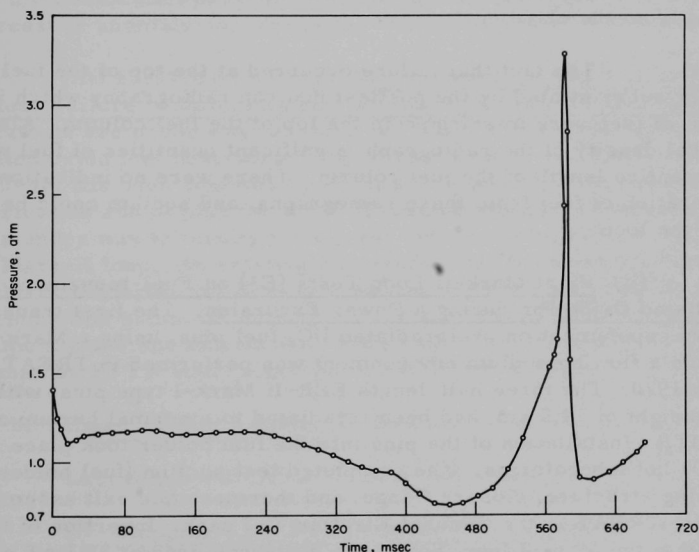


Fig. IV.A.4. Base Pressure for Expulsion Run 61770-4
(Freon-113; initial superheat = 28°F)

The model described in ANL-7655 has been modified to account for the slug growth in the cold portion of the test section. Initial results appear to predict the growth and collapse.

2. Fuel Dynamics Studies in TREAT (C. E. Dickerman)

a. Transient In-pile Tests with Ceramic Fuel (C. E. Dickerman)

Last Reported: ANL-7705, pp. 178-181 (June 1970).

(i) First Two Mark-II Loop Tests (H-1 and H-2) on Transient Failure Threshold of Mixed Oxide Fuel Element with Axial Heat Transport by Flowing Sodium. The transient test data for the H-2 experiment have been received from Idaho. Preliminary analysis of the data showed three major pressure pulses of 116, 55, and 75 psi at transient times of 1.5, 1.6, and 1.7 sec, respectively. Incipient boiling, as indicated by the prefailure pressure and flowmeter data, occurred at 1.45 sec.

Currently, the conclusion is that failure occurred during the first pressure pulse (116 psi). Immediately following this event, the test-section thermocouple rose rapidly to 1100°C before going off scale at 1400°C. Apparently this thermocouple, which was located axially 1 in. below the top of the fuel column, measured the temperature of the hot fuel released from the cladding.

The fact that failure occurred at the top of the fuel column is further substantiated by the posttest neutron radiography which indicated that 3 in. of fuel were missing from the top of the fuel column. Also, from the optical density of the radiograph, significant quantities of fuel were lost over the entire length of the fuel column. There were no indications of agglomeration of fuel from these radiographs, and sodium could be pumped through the loop.

(ii) First Mark-II Loop Tests (E3) on Fuel-movement Failure of Irradiated Oxide Pin during a Power Excursion. The first transient meltdown experiment on preirradiated UO_2 fuel pins, using a Mark-II loop to provide a flowing sodium environment was performed in TREAT on June 19, 1970. The three half-length EBR-II Mark-I type pins, with a fuel column height of 14.5 cm, had been irradiated to a normal burnup of 6 at. % in the MTR. Installation of the pins into the fuel holder took place in the Bldg. 301 hot laboratories. The completed test section (fuel holder, positioning structure, closure flange, and thermocouple exit assembly) was shipped to TREAT in the General Electric T-2 cask. Insertion of the test section into the Mark-I loop (Serial No. B-1) was done at TREAT as a semiremote operation using the TREAT fuel handling coffin. Experience gained in this operation will be extremely useful should similar operations be contemplated for future experiments which use preirradiated pins.

Pretest neutron radiographs of the loop and pretransient neutron hodoscope data were taken following test section installation. The

radiographs provided assurance that the test section was properly seated in the loop and that no damage had been sustained during shipment.

The TREAT core was reloaded to the configuration corresponding to that of the calibration run. Using the prototype Mark-II loop with no outfitting as a nuclear mockup, a control rod calibration for the loading was obtained. This calibration showed that the maximum reactivity available with this loading would be necessary in order to provide sufficient energy release in the experiment. Heat balance data obtained during the calibration has allowed refinement of the calibration factor for the experiment to $1.66 \text{ J/g} \cdot (\text{MW} \cdot \text{sec})$ TREAT energy release.

Two transients were run. The first, having a reactor energy release of about 160 MW-sec, was intended to provide instrument checkout and data for comparison with SAS-1A calculations of the coolant temperature rise. The second transient, which resulted in failure of the fuel pins, realized an energy release of about 1250 MW-sec and a peak power level of about 7000 MW. The instrumentation indicated excursions in both inlet and outlet pressure and flow and in outlet temperature. The first pressure anomaly occurred near the time of peak power level.

(iii) First Mark-II Loop Experiments (L1 and L2) on Fuel-movement Failure of Unirradiated Fuel during a Loss-of-flow Accident. Preparations are under way for the first TREAT loop experiment on unirradiated oxide fuel behavior during a loss-of-flow accident. The fuel pin, PNL-17-30, has been supplied by PNL; it is a prototypical sample from the fabrication run of pins for the EBR-II instrumented subassembly PNL-17. Work is under way to modify the top and bottom fittings of the pin for use with a Mark-II loop. An existing test section has been assigned, and the fourth Mark II (Serial No. B-2) has been assembled, including its annular linear-induction pump, in preparation for sodium filling and prooftesting. Experiment plans and calculations are being based on accident calculations performed by FFTF staff (reported in BNWL-cc-2500).

b. Experimental Support (C. E. Dickerman)

Last Reported: ANL-7705, p. 180 (June 1970).

(i) Shipping-cask Procurement Documentation. Work on the cask specification has been completed. The document has been reviewed, approved, and released. The prospective fabricator, National Lead Company, has been asked to submit a bid based on the specification by July 23, 1970. The fabricator has prepared shop drawings, based on the specification drawings, which are being reviewed by ANL. The cask-evaluation document, including the appendixes, is complete except for clerical work incorporating minor changes and corrections. The entire cask

package, including the specification, evaluation document, quality-assurance program, and quality-control plan, are to be available by the week of July 27, 1970.

c. Analytical Support (C. E. Dickerman)

Last Reported: ANL-7679, pp. 155-156 (March 1970).

(i) Automated Handling of Hodoscope Data. Transient 1281 (checkout 1) data have been processed and analyzed in part. Scanning of the data film by CHLOE did not start at the proper marker on the 16-mm film, so that the actual scanned portion began about 0.2 sec after the peak power of the transient. CHLOE has since been dismantled and will soon be replaced by a better film-scanning system, ALICE. When ALICE is available, the film scanning will be redone.

Even with the limitations presented, we are able to establish certain additional operating characteristics of the hodoscope. To get the full benefit of the existing data with regard to the dynamic features of the fuel behavior, we have to make a motion study of the output because of the wealth and complexity of the data. Capability for such a motion study has been designed into the new display system being developed in the Electronics Division.

We are now aware of a nonlinear saturation of the hodoscope system during the high-power portion of the transient. On the basis of this information, derived mostly from transient 1283, we have arranged to change the operating parameters of the hodoscope to improve detector performance without sacrifice in efficiency--where possible. In addition, further work on transient response is under way.

Because the actual scanning of the film from transient 1281 began after the peak transient, it is probable that the available 1281 data is free of the nonlinearity, although we do not have enough transients analyzed to state this with confidence.

After automatic scanning by CHLOE, the data are rendered in two forms: a printed output with all count rates, and a 35-mm film output with the data transformed into a computer-produced rendition of the fuel pattern. The 35-mm output puts the data into two arrangements: On the left, the intensity is proportional to the count rate; to the right, an x-y plot is made of the count-rate profiles.

Taken at face value, the data altogether suggest density variations in fuel throughout the period that the transient was followed, namely for 2 sec after the peak power. The fuel pin was essentially intact throughout the observable portion of the transient and did not undergo any

bending beyond a limit probably of about 0.05 in. There is fuel at the bottom of the pin, and throughout the transient there are density fluctuations of fuel within the pin container. At the point at which hodoscope data begins, the fuel has an apparent length of over 14 in. Since the initial length of the pin was about 11 in., it is evident that the full expansion of the pin within its container had already taken place. It is hoped that in later scanning with ALICE the time that this movement or expansion occurred can be ascertained.

A remarkable feature of the hodoscope is now emerging from the limited data already analyzed: This is the extended (and unexpected) sensitivity of the device long after the transient level has subsided. Original design of the hodoscope was based on adequate efficiency to catch events which may frequently take place when the power has dropped by about 10% of the peak. What we are now seeing rather consistently are two surprising features. In transient 1281, for example, we have adequate count rate to clearly define the fuel pin almost 2 sec after the peak. The apparent count rate is about 10^{-3} or 10^{-4} of the peak power level at this late time.

The other surprising feature, now partially explainable, is the improved dynamic-signal background resolution (a factor of two or three better than the equilibrium spatial resolution). This seems to be due to the residual gamma sensitivity of the fast-neutron detector working in a favorable way. (See monthly progress report for March 1970, ANL-7679, p. 155.)

Thus, the data from transient 1281 show sensitivity going out to 2 sec after the peak (this is as far as CHLOE scanned) with good dynamic resolution still present. In this case, the last frame scanned has an average of four counts per detector focused on the fuel pin while adjacent background averages about one count per detector. This is a favorable 3:1 signal-to-background ratio and at this stage represents adequate count statistics to define useful features of the fuel pin. One should recall that the best static resolution achieved with the Mark-II sodium loop is in the vicinity of 3:1 signal-to-background ratio. It is beyond the scope of this report to discuss the hodoscope's general space- and time-resolution characteristics because of their correlated complexity, but it is reasonable to state that the design values have been verified in the data analyzed to date.

In summary, the hodoscope instrumentation in certain valuable functional areas is exceeding performance specifications; in terms of saturation at high power levels, performance has not been linear, but that is subject to improvements already instituted. The current problem area is in processing the wealth of data accumulated during the last year.

(ii) Analysis of Transient In-pile Experiments. Because TREAT is a thermal reactor, prototypical mixed-oxide fuel pins (including highly enriched pins of the type typically used for EBR-II irradiations) have large

internal neutron-flux depressions when exposed to the unperturbed TREAT neutron spectrum. For convenience, the effects of such flux depressions can be discussed on the base of the two following cases:

1) Short power pulse (duration less than or in the order of the pin thermal time constant for radial heat flow). In principle, this case can lead to surface oxide temperature peaking and low central transient fuel temperatures. Two approaches are being used to minimize this problem: (a) low-enrichment oxide pins (13% enriched, in the case of shots E-1, E-2, and E-3); and (b) thermal neutron-flux filter with highly enriched pins (shots H-1 and H-2).

2) Long, or "flattop" power pulse (duration significantly longer than the pin thermal time constant, as a simulation of steady-state-like power conditions). This case is not, in principle, really as severe as the first above. If we compare the steady-state radial temperature distributions for two limits--a pin with radially flat power profile and a pin with a radial power profile typical of that for a fully enriched FFTF-type pin in TREAT--for the same total power as a function of axial position, the following conclusions apply: (a) The coolant and cladding temperature distributions are the same, because the total powers as a function of axial position are the same; (b) the radial oxide temperature distributions are quite similar near the edge of the fuel, but the fuel temperatures of the flux-depression case drop significantly below the uniform radial power case near the fuel center; and (c) the conductivity integral, $-\int k \, dt$ from centerline to fuel surface for the flux depression case, where k is thermal conductivity and T is temperature, is about two-thirds the integral for the uniform radial power case.

Only Case 1 above will be considered in the following. The SAS1A code has been modified for transient heat-transfer calculations with nonuniform radial power generation in the fuel.

The effect of three different radial fuel power profiles on the unirradiated-fuel-pin failure experiment (H-2) with the Mark-II sodium loop has been studied. Specifications of the prototypical FFTF fuel pin (PNL-17 series) are given in Table IV.A.1. Fuel-temperature profiles, cladding and coolant temperatures, and fuel-pin elastic-plastic deformation were calculated for three radial power distributions in the test pin (see Fig. IV.A.5). A flat power profile (Curve A in Fig. IV.A.5) is a typical radial power distribution in a fast reactor, excluding, of course, fuel restructuring and burnup. Curves B and C are SNARG-2D S_2 calculated power distributions in the test pin when subjected to a power transient in TREAT reactor with and without the H-2 neutron shield, respectively. Curve B is typical for all loop shots run thus far and is not limited to H-1 and H-2. Each power-distribution curve is normalized to a volume-averaged calibration factor of 3.30 J/(MW-sec-g oxide).

TABLE IV.A.1. Prototypical FFTF Fuel Pin--PNL-17-42

<u>Fuel</u>	
Composition	75% UO ₂ , 25% PuO ₂ unirradiated
Enrichment	65% enriched U 89% enriched Pu
Pellet density	10.13 g/cm ³ (94.5% T.D.)
Smear density	9.54 g/cm ³ (89% T.D.)
Pellets, ID	0.0 cm
OD	0.493 cm
Length	34.44 cm
Fuel-clad diametral gap	0.015 cm
<u>Cladding</u>	
Type	3.6 SS
Wall	0.038 cm

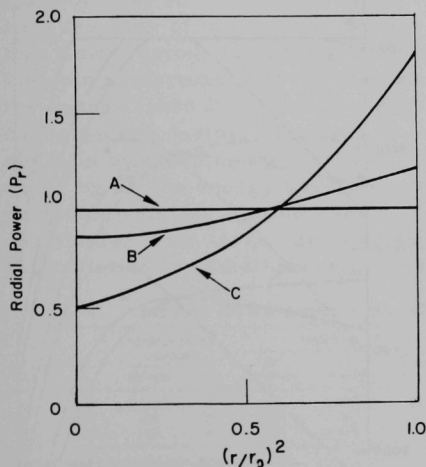
Fig. IV.A.5. Radial Power Distribution vs Square of Fuel Radius (r_0 = fuel outer radius)

Figure IV.A.6 shows the power transient and energy as a function of time used in the present analysis. This transient, slightly more powerful than the actual H-2 experiment transient, was equivalent to an integrated pin power of 463 MW-sec x 3.30 J/(MW-sec-g oxide) or 1528 J/g-oxide with peak transient pin power of 10.5 kW/cm. The full width at half-maximum for this transient was 0.26 sec.

Calculated fuel-temperature distributions at the midpoint of the fuel pin are plotted as a function of $(r/r_0)^2$ in Fig. IV.A.7 (r_0 is the fuel outer radius) for power generation curves of Fig. IV.A.5 at three different times (0.500, 0.525, and 0.550 sec). This ordinate scale is chosen rather

than r in order to facilitate volume comparisons. The quantity plotted is temperature + X, where X is a number given in the figure. This makes it possible to plot fuel-temperature profiles at different times in a single graph. A nonzero temperature gradient at $r = 0$ should not be alarming since temperatures are plotted as a function of the square of the radius. This point is mathematically illustrated by considering r^2 -dependence of fuel temperature for small r

$$T = T_0 - x + A(r/r_0)^2,$$

where T_0 is the centerline temperature and A is the constant. Then,

$$\frac{d(T+X)}{d(r/r_0)} = 2A\left(\frac{r}{r_0}\right)$$

and

$$\frac{d(T+X)}{d(r/r_0)^2} = A.$$

Clearly, at $r = 0$,

$$\frac{d(T+X)}{d(r/r_0)} = 0 \text{ and } \frac{d(T+X)}{d(r/r_0)^2} = A.$$

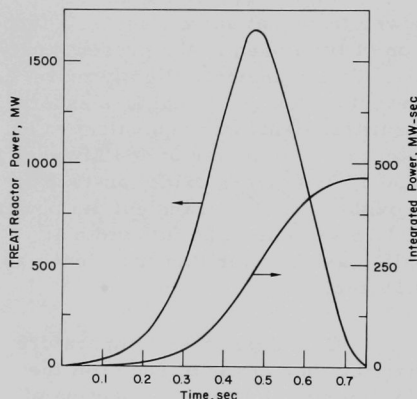


Fig. IV.A.6. Assumed TREAT Reactor Power and Integrated Power (H-2)

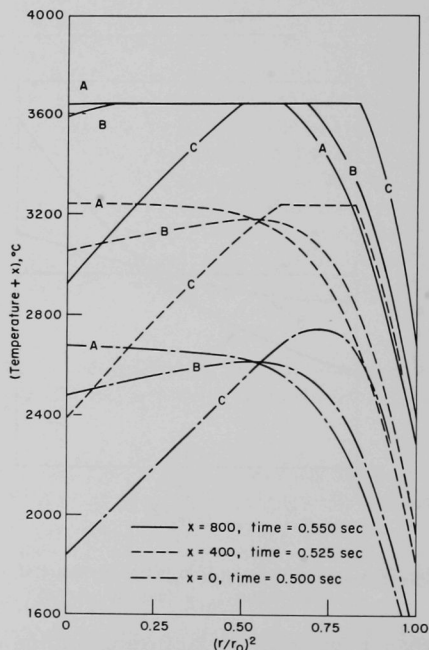


Fig. IV.A.7. Calculated Temperatures vs r^2 for Three Power Profiles

The general trend of fuel-temperature distribution for different power profiles is self-explanatory. For example, fuel surface temperatures are a lot higher for case C in which a larger amount of heat is

generated near the surface as compared to case A where the amount of heat generated is uniform throughout the pin. In addition, the similar arguments apply to the location of fuel which undergoes phase change during the transient. (See, e.g., curves at 0.525 and 0.550 sec in Fig. IV.A.7.) Needless to say, both the amount and location of fuel melting play a major role in fuel-pin performance leading to its rupture for both unirradiated and irradiated fuel elements. For preirradiated highly enriched fuel pins, the thermal-neutron shielded pin (case B) and unshielded pin (case C) could lead to a very different result, since in case C melting begins approximately in the equiaxed region which is thought to have retained about half the fission gases produced in that region.

No cladding and coolant temperatures are calculated from the heat flux at the fuel surface. Since the transient heat flux at the fuel surface increases appreciably from case A to C (because of the shorter oxide length for heat flow in case C), both cladding and liquid sodium temperatures would increase accordingly. Consequently, coolant in case C would begin to boil at an earlier time (i.e., with less total energy deposition) than for case A. This observation is substantiated by Table IV.A.2 which lists the time of initiation of boiling, the specimen energy deposition up to that time, various temperatures in the fuel and cladding, etc., characterizing fuel-pin performance at the midpoint of the fuel section. The percentage of the energy (1528 J/g of oxide) needed to initiate coolant boiling for three cases under consideration vary from 89 to 74%. If one assumes that a fuel pin fails by cladding meltthrough at a time when the energy deposition exceeds by 5% the energy required to initiate boiling, then fuel-pin failure is predicted with 94, 89, and 79% of total energy for cases A, B, and C, respectively. This large variation in the threshold failure energy is due to the variation in radial power generation in fuel pins.

TABLE IV.A.2. Effect of Neutron Shield on Fuel-pin Condition at Time of Coolant Boiling for Midpoint of Fuel Section^a

Case	Time, sec	Specimen Energy Deposition		Temperatures, °C			Outer Radii, cm		Mass Fraction of Molten Fuel, %	Fuel $\Delta V/V$, %	Plastic Strain, cm/cm
		J/g-oxide	%	Fuel ^b Centerline	Fuel Surface	Cladding Hot Spot	Fuel	Cladding			
A	0.6076	1355	89	2973	1555	1125	0.2646	0.3024	62	15.3	0.002
B	0.5865	1290	84	2840	1647	1136	0.2626	0.3007	39	13.6	0.016
C	0.5452	1130	74	2097	1875	1180	0.2589	0.2976	~25	10.4	c

^aInlet coolant temperature is taken to be 400°C.

^bMelting temperature of mixed-oxide fuel is taken to be 2840°C.

^cBecause of current SAS1A code limitations, this strain cannot be calculated.

Another quantity of interest is the mass fraction of molten fuel and the associated change in fuel volume from design temperature to the time of failure. Table IV.A.2 also lists these quantities up to the time of bulk coolant boiling. To make a meaningful comparison of fractional change in fuel volume for three cases, we list below the $\Delta V/V$ values for fuel under adiabatic assumption from the density table:

$$\frac{\Delta V}{V} \text{ (from 27°C to melting point) } = 17.5\%,$$

$$\frac{\Delta V}{V} \text{ (due to change in phase for the FFTF fuel)} = 5.5\%,$$

and

$$\frac{\Delta V}{V} \text{ (from } 27^{\circ}\text{C to complete melting)} = 23.0\%.$$

The plastic strain, or permanent deformation of the cladding, is calculated for cases A and B. Strain values calculated for case C are incorrect because of the limitations of the model and the logic of the SAS1A code.

Cladding is considered to be deformed plastically if the loop stress exceeds the cladding yield point. Although this situation may occur even without any fuel melting, a large contribution to the plastic deformation arises from the change of phase (see above). The logic of the current version of the SAS1A code assumes fuel-volume change from melting to progress outward, starting from center or the inner fuel surface. When a molten fuel ring is formed within a fuel pin without any molten fuel at the inner surface (as, for example, in case C), the code would not include the contribution to the cladding plastic strain which results from an increase in fuel volume at melting.

These calculations indicate that case B is significantly closer to case A than the unshielded case C. Cases A and B do show differences, but their significance is not clear pending more data on the true cladding deformation produced by transients of this type.

d. Hot Laboratory Examinations (L. A. Neimark and W. F. Murphy)

Last Reported: ANL-7705, p. 180 (June 1970).*

(i) Examination of Pins after TREAT Tests

(1) Examination of Unirradiated PFR Fuel Element from Test H-1. Eddy-current examinations have been performed on PFR fuel element 726 (Experiment H-1), after TREAT exposure 1298. There were eight axial traces, each covering a 45° arc on the circumference. Results from the traces will be used to select sections for destructive examinations of the pin.

(2) Examination of Unirradiated UO₂ Fuel Element from Test E-2. Examination of fuel element 2-R-1 from TREAT Experiment E-2 has started. This fuel element had failed during the TREAT transient, and

*Previously reported under Postirradiation Examination.

most of the enriched uranium fuel had been ejected. Macrophotographs have been made of the two remaining sections of the element, both with and without the wire wrap. Diameter measurements of the cladding were made where possible. The two parts of the element have been sectioned for metallographic examination.

3. Fuel-Coolant Interactions (R. W. Wright)

a. Particle Heat-transfer Studies (D. R. Armstrong)

Last Reported: ANL-7661, pp. 130-131 (Jan 1970).

(i) Experiments Immersing Single Sphere in Sodium. The falling sphere assembly has been modified to minimize the initial shock induced by impact of the falling sphere. The modification involved the use of an air cylinder having a hollow shaft to drive the sphere into the sodium pool, rather than a gravity controlled system.

The dry box has been sealed off, and a workable argon atmosphere has been attained. Preliminary runs with highly subcooled sodium (200°C) and a tantalum sphere heated to 2000°C indicated some difficulties. The severe thermal shock experienced by the sphere was responsible for breaking thermocouple connections to the surface, damaging the sphere surface grains, and in one case breaking the supporting tube. In a subsequent run, the sphere was annealed at 1200°C for 30 min. This seems to have eliminated the second and third difficulties. Heavier thermocouples are planned to be used in the future to overcome the first difficulty.

Two successful runs with good reproducibility have been achieved, one with no operational thermocouple. The pressure transducer traces, however, indicate a fair amount of boiling.

b. Model Development (D. H. Cho)

Last Reported: ANL-7688, pp. 240-245 (April-May 1970).

(i) Development of Computer-code Representation of Parametric Model of Pressure-generation for Accident Analysis. The formulation of the parametric model, previously discussed in ANL-7688, pp. 240-245, has been programmed for computer calculation using two different approximations for the energy-transfer process. Preliminary calculations have been made considering a 35-cm-long molten zone in an FFTF subassembly, and both acoustic and inertial constraints. The calculations represent a first step toward examining the effects of various limiting-rate processes.

Two different approximations were used for the heating of sodium in the fuel-coolant mixing zone. The first approximation considered quasi-steady-state heat transfer with the heat flux, q , given by

$$q = hA(T_f - T_{Na}),$$

where h is the effective heat-transfer coefficient, A is the heat-transfer surface area, and T_f and T_{Na} are the average fuel and sodium temperatures. The heat-transfer coefficient, h , was given in the approximation by

$$h = \frac{k_f}{R},$$

where k_f is the thermal conductivity of the fuel and R is the fuel particle radius. This approximation accounts for a finite rate of fragmentation and mixing. The second approximation considered instantaneous fragmentation and mixing followed by transient conduction from the fuel particles into the sodium. The integral method was used to solve the transient conduction problem. Initially, in this case,

$$q \propto \frac{1}{\sqrt{t}}.$$

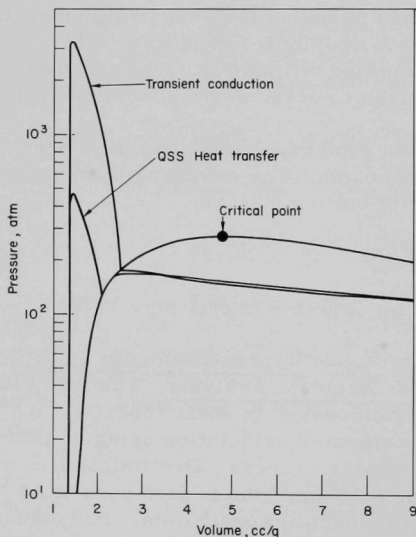


Fig. IV.A.8. Effect of Heating Rates on Pressure Generation due to Molten-fuel-Coolant Interaction

The calculations assumed a uniform dispersion of fuel particles of radius 117μ in the sodium, and used a fuel-to-sodium mass ratio of 8.3. The heat-transfer resistance in the sodium was neglected (even after vaporization of the sodium had started), so that the temperature of the heated sodium was uniform throughout the mixing zone. The initial temperatures used for the sodium and fuel were 1100 and 2900°K, respectively.

Figure IV.A.8 is a p - V plot of the results obtained when a one-dimensional acoustic constraint of infinite extent was assumed, both upward and downward. The equation of constraint is

$$P(t) - P_0 = \rho_0 C_0 \frac{dZ}{dt},$$

where $P(t)$ is the pressure in the mixing zone, P_0 is the initial pressure

throughout, ρ_0 and C_0 are the density and sonic velocity of the unheated sodium in the loading column, and $Z(t)$ is the position of the interface between the mixing zone and the loading column. Figure IV.A.8 shows that the peak pressures occur during the liquid-phase heating and expansion. The transient-conduction approximation gives an order-of-magnitude higher peak pressure and a larger amount of work than does the quasi-steady-state heat-transfer approximation, because of its higher initial heating rate. The peak pressure for the transient-conduction approximation was reduced by 6% when the presence of 1% (volume) inert gas in the

heated sodium was taken into account. The critical pressure shown in Fig. IV.A.8 is somewhat lower than Dillon *et al.*'s value (350 atm),* because the calculations used the sodium vapor pressure equation of Stone *et al.*** up to the critical point.

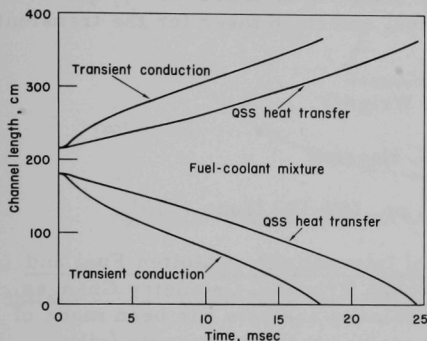


Fig. IV.A.9. Voiding Histories from Molten-fuel-Sodium Interactions

Figure IV.A.9 shows voiding histories resulting from molten-fuel-sodium interactions in a 35-cm-long molten zone of an FFTF subassembly. It is assumed that the coolant columns above and below the fuel-coolant mixing zone is incompressible and does not exchange heat or mass with the mixing zone. The heated

coolant in the mixing zone expands against the inertia of the unheated coolant columns (one-dimensional inertial constraint). A macroscopic momentum balance gives the equations of motion of the constraining coolant columns,

$$\frac{dU_2}{dt} = -g + \frac{P - P_{ex}}{\rho(Z_{ex} - Z_2)} - \frac{1}{2}U_2^2 \frac{f}{R_h},$$

and

$$\frac{dU_1}{dt} = g + \frac{P - P_{in}}{\rho Z_1} - \frac{1}{2}U_1^2 \frac{f}{R_h},$$

where P_{ex} is the exit plenum pressure, P_{in} is the inlet plenum pressure, P is the pressure in the fuel-coolant mixing zone, ρ is the density of the unheated coolant, Z_{ex} is the position of the exit plenum (measured from the inlet plenum), Z_2 is the position of the interface between the mixing zone and the upper coolant column, Z_1 is the position of the interface

*ANL-7025, p. 42.

**ANL-7323, p. 18.

between the mixing zone and the lower coolant column, U_2 is the ejection velocity of the upper coolant column, U_1 is the ejection velocity of the lower coolant column, g is the acceleration due to gravity, f is the friction factor, and R_h is the hydraulic radius of the coolant channel. The calculations used the following parameters based on FFTF conditions: $P_{ex} = 1,456$ atm, $P_{in} = 7.485$ atm, $Z_{ex} = 420$ cm, $Z_2(t = 0) = 215$ cm, $Z_1(t = 0) = 180$ cm, $f/R_h = 0.0542 \text{ cm}^{-1}$ (estimated). Other initial conditions were identical to those used for Fig. IV.A.8. Figure IV.A.9 gives the voiding histories for both approximations of quasi-steady-state heat transfer and transient conduction. The lower channel becomes completely voided in 25 msec for the quasi-steady-state heat-transfer approximation, and in 18 msec for the transient-conduction approximation.

4. Postaccident Heat Removal (R. W. Wright)

a. Engineering Analyses (J. C. Hesson)

Last Reported: ANL-7705, pp. 189-192 (June 1970).

(i) Mathematical Models of Interactions of Molten Fuel and Structural Materials, Including Meltthrough Process, Geometry Changes, and Movement of Molten Mass. A preliminary analysis has been made of the penetration of sacrificial barrier material such as concrete (silica aggregate) and depleted UO_2 blocks by the molten UO_2 fuel debris. The penetration rate of a barrier is determined by the rate of heat transfer from the pool to the barrier surface and the heat required to raise the temperature of the barrier material to the melting point and to melt it. Heat-transfer rates to the bottom of boiling and nonboiling pools are discussed in the Progress Report for April-May 1970, ANL-7688, pp. 244-249. [Note: In the equation for T_r on the bottom of page 248 of ANL-7688, the part of the equation in brackets should be multiplied by 10^3 ; and in the two equations on page 249, $(T_m - T_s)$ should be $(T_m - T_r)$.]

It is assumed that penetration of the barrier occurs uniformly in radial directions, resulting in a hemispherical pool as shown in Fig. IV.A.10. The temperature-inversion conditions at the bottom of the melt tend to limit the heat-transfer rate and are less effective on the vertical sidewalls, causing the pool to enlarge horizontally more rapidly than vertically. This could cause the pool to spread and reduce its depth, which is a desirable condition.

When the temperatures and heat transfer by convection in the pool are computed, the radius of the pool is used as the depth for calculating the maximum heat flux. When surface temperatures and heat flux from the surface of the pool are estimated, the surface area of the pool is used to compute average values.

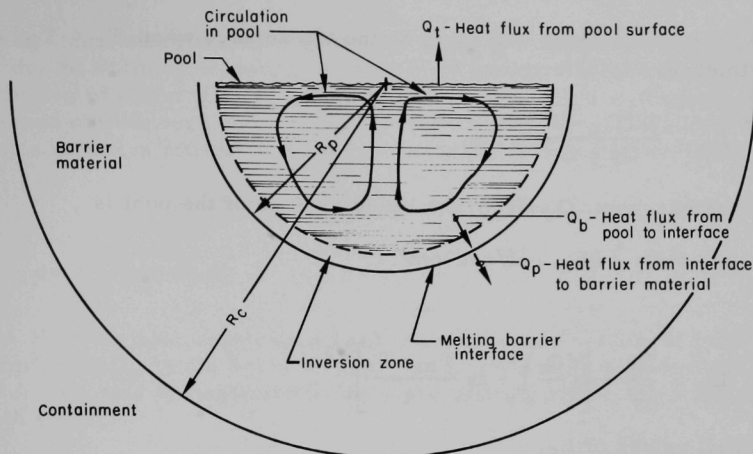


Fig. IV.A.10. Penetration of Barrier by Core Debris under Condition of No Cooling

The following equations are used in the penetration calculations. The top surface heat flux from the pool is expressed by

$$Q_r = Pf/S - 2Q_b, \text{ cal/sec-cm}^2,$$

where P is the reactor power (112×10^6 cal/sec for FFTF), f is the fraction decay heat at time t , and S is the surface area (πr^2) of a pool with radius r , in cm^2 . The bottom heat flux, Q_b , which is calculated later, is usually $\ll Q_t$, and $2Q_b$ can be neglected, at least for the first approximation.

The temperatures found at the top of the pool are expressed by

$$T_r \approx 1000 \left[(Q_r/1.37E) + \left(\frac{T_a + 273}{1000} \right)^4 \right]^{1/4} - 273,$$

where $E \approx \epsilon/(2 - \epsilon)$ for parallel surfaces, ϵ is emissivity, T_a is the ambient temperature in $^\circ\text{C}$, and T_r is the calculated radiation temperature in $^\circ\text{C}$ for heat loss by radiation. If heat is removed from the top surface by some method other than radiation, say by conduction to sodium, then T_r is computed from Q_t , the heat flux from the surface of the liquid pool. If T_s is the temperature of the liquid surface of the pool, T_b is the boiling temperature, and T_r is the temperature of the crust top surface, then

$$T_s = T_b \text{ if } T_r > T_b, ^\circ\text{C},$$

$$T_s = T_r \text{ if } T_m < T_r < T_b, ^\circ\text{C},$$

and

$$T_s = T_m \text{ if } T_r < T_m, ^\circ\text{C}.$$

A crust will form on the top surface when $T_r < T_m$ and the crust thickness is determined by

$$L_c = \frac{2k(T_m - T_r)}{Q_r + Q_t}, \text{ cm},$$

where the heat flux, Q_t , from the liquid surface of the pool is

$$Q_t = Q_r - qL_c, \text{ cal/sec-cm}^2.$$

Then,

$$L_c = \frac{Q_r}{q} - \left[\left(\frac{Q_r}{q} \right)^2 - 2k \frac{T_m - T_r}{q} \right]^{1/2}.$$

For small values of L_c ,

$$L_c = k(T_m - T_r)/Q_r, \text{ cm},$$

where k is the thermal conductivity of the crust (≈ 0.005 cal/sec-cm- $^{\circ}\text{C}$ for UO_2 debris), and q is the specific decay heat in the crust, cal/sec-cm 2 .

The temperatures in pool are expressed by

$$\begin{aligned} T_4 - T_s &= (Q_t/0.068)^{3/4} (\mu^2/\rho^2 g \beta k^3)^{1/4} \\ &= \left[q_0 f \left(\frac{r_0}{r} \right)^2 r_0 / 0.068 \right]^{3/4} (\mu^2/\rho g \beta k^3)^{1/4}, \end{aligned}$$

$$T_i = T_s + \frac{T_4 - T_s}{2} \text{ for nonboiling pool,}$$

and

$$T_i = T_b \text{ for boiling pool,}$$

where T_4 is the maximum temperature in the pool ($^{\circ}\text{C}$); T_i is the upper temperature of the inversion zone ($^{\circ}\text{C}$); μ , ρ , β , and k are viscosity (poise), density (g/cm 3), coefficient of thermal expansion (1/ $^{\circ}\text{C}$), and thermal conductivity of pool debris (cal/sec-cm 2 - $^{\circ}\text{C}$); and g is acceleration due to gravity (980 cm/sec 2). The heat-transfer rate from pool to bottom is found from the equation

$$Q_b = \sqrt{2k(T_i - T_m)(r_0, r)^3} q_0 f,$$

where q_0 is the reactor specific power, in cal/sec-cm 3 , and f is the fraction of decay power. This is based on uniform distribution of the fission-product decay-heat sources in the melt, including the inversion layer.

Actually, the concentration of heat sources in the inversion layer would be less, due to addition of melting barrier material to the pool. However, the assumption of uniform distribution is conservative, since it results in an increased meltthrough rate. A model for UO_2 -concrete interaction which includes diffusion effects in the inversion layer is being developed.

The rate of pool radius enlargement is expressed by

$$dr = \frac{Q_b - Q_p}{H} dt,$$

where H is the heat required to heat and melt a unit volume of barrier in cal/cm^3 , and Q_p is the heat flux from the melting zone into the bulk of the barrier. Q_p can be neglected in the early phases. When $Q_p = Q_b$, pool growth stops.

The penetration of the barrier involves a moving-boundary problem, exact solutions for which are quite complicated. To simplify the problem for this preliminary analysis, we assumed that all heat flux to the barrier was used at the interface to heat and melt the barrier. In addition, the heat flux into the barrier was calculated for a stationary interface, and when this heat flux was equal to the heat flux to the barrier, pool growth would stop. The expression for heat flux from a stationary interface into the barrier contains the time-dependent term,

$$Q_p = kT_m \left(\frac{1}{r} + \sqrt{\frac{C_p \rho}{\pi k t}} \right),$$

where t is the time from the start of the penetration. Since r varies, the assumption of constant r results in a calculated value of Q_p less than that which would actually occur at cessation of pool growth. The above two assumptions result in a slightly enlarged calculated pool radius. This introduces a negligible error, as compared to other uncertainties such as appear in the values of physical and thermodynamic properties and heat-transfer factors and parameters.

The FFTF was used as a reference case for calculations using concrete and depleted- UO_2 blocks as sacrificial barrier material. Examination of oxide phase diagrams indicate that UO_2 would have considerable solubility in a SiO_2 - CaO - Al_2O_3 - MgO - Fe_2O_3 melt, the principal ingredients of silica aggregate concrete which would be used at FFTF.* In general, carbonate aggregates would not be used, because of the release on heating of large volumes of CO_2 into the containment vessel. For both concrete and UO_2 barrier materials, two different assumptions are made: (1) All fission-product heat sources remained with and were uniformly

*Private communication from G. Jansen of PNL-Richland, Washington.

distributed in the melt; and (2) only half the fission-product heat sources remained in the melt, but those remaining were uniformly distributed.

For concrete penetration, we assumed that any steel in the melt either floated on top or sank to the bottom and did not alloy or mix with fission-product heat sources or interfere with heat transfer or concrete ingredient melting. For UO_2 penetrations, we assumed that any steel in the melt floated on top. In both cases, we assumed that heat loss from the top of the melt was by radiation with an emissivity coefficient of 0.5.

In applying the analyses to FFTF, we used the following parameters: reactor power $P = 112 \times 10^6$ cal/sec; core UO_2 volume = 29.7×10^4 cm³; core UO_2 weight = 297×10^4 g; and core average specific power per unit volume $q_0 = 378$ cal/sec-cm³. An ambient temperature for the barrier (concrete and UO_2) of 100°C was used.

In the case of concrete, we assumed that the UO_2 and concrete ingredients are miscible and that the melting point of the concrete-rich mixture is 1100°C.

Figure IV.A.11 shows results for the penetration of depleted UO_2 under conditions of 100 and 50% of the decay heat retained in the melt. Figure IV.A.12 shows results for the penetration of concrete for 100 and 50%

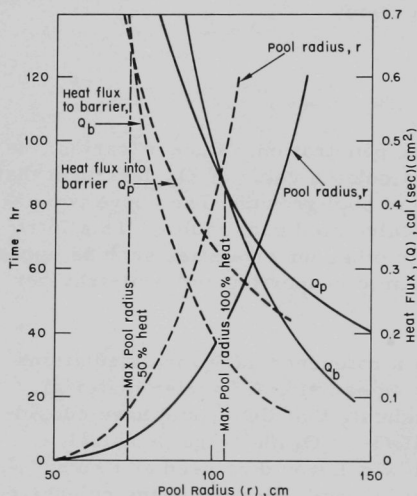


Fig. IV.A.11. Pool Radius for Depleted- UO_2 Barrier.
 — 100% of decay heat;
 --- 50% of decay heat.

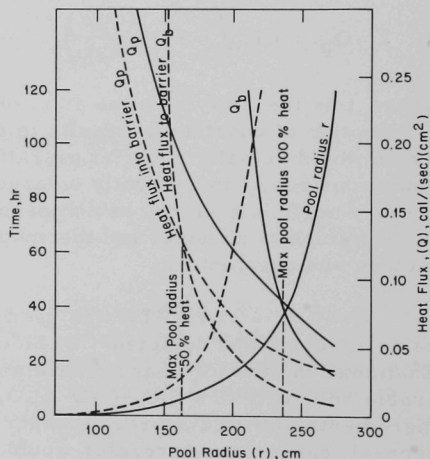


Fig. IV.A.12. Pool Radius for Concrete Barrier.
 — 100% of decay heat;
 --- 50% of decay heat.

of the decay heat retained in the melt. Here it is assumed that the basic melting temperature of the melt is 1100°C . Calculations made assuming that the temperature of the melt varied from 2800 to 1100°C , as the fraction of dissolved concrete increased, showed only a minor difference from the result for a fixed concrete melting temperature.

The wall of the secondary containment vessel may be located at some position in the barrier. The maximum temperature at this location is important, since it will be limited by the design of the vessel. The calculations showed that heating of the containment wall would be a problem, even though the molten material does not reach the wall. After 100 days, wall temperatures in excess of 500°C could occur at positions 10 ft into the barrier.

Further analytical and experimental work is needed to verify the convective heat transfer models for the pool as well as other facets of the problem.

B. Operations

1. TREAT Operations (J. F. Boland)

Last Reported: ANL-7705, pp. 180-181 (June 1970).

a. Reactor Operations

Experiment C4X was subjected to two calibration transients for GE. This experiment, which contains a fully enriched UO_2 fuel sample, is a lead experiment for future TREAT experiments on GE fuel materials that have been irradiated in EBR-II. After evaluation of data from the calibration transients, C4X will be subjected to a transient that will heat the fuel to the threshold of cladding failure.

Neutron radiographs were made of EBR-II driver fuel and of experimental capsules from Subassemblies X071, X027, and X012A. Neutron radiographs were also made of TREAT experiment GE-C4X, of a PBF fuel rod after irradiation in SPERT, and of samples for radiographic-technique development by the ANL Materials Science Division.

Two transient tests were conducted to evaluate the transient performance of the wide-range nuclear-instrument channels that are undergoing steady-state testing at EBR-II.

b. Automatic Power Level Control System

Testing of the hydraulic-control-rod drives at the vendor's plant has been completed, and the drives are scheduled for shipment the first week of August.

C. Engineered Safety Features--Safety Features Technology

1. Reactor System and Containment Structural Dynamic Response (S. H. Fistedis)

a. Hydrodynamic Response to High-energy Excursion (Y. W. Chang and T. J. Marciniak)

Last Reported: ANL-7679, pp. 170-177 (March 1970).

(i) Parametric Studies of System Geometries and Excursion Magnitudes and Durations to Assist FFTF Accident Analysis. ANL assistance in FFTF safety effort was formalized with specific "task statements" agreed upon by FFTF and ANL. In this technical area, the pertinent task statement for FFTF support is: "Reactor System and Containment Structural Dynamic Response," dated June 2, 1970. In accordance with this task statement, work at ANL proceeded with the evaluation of vessel and plug

response to a hypothetical accident. This portion of the study in the subject task statement, designated as "preliminary" had an August 1970 completion date. However, since the requested effort was parallel to the ANL fast-reactor containment program, the subject results were made available to FFTF considerably earlier on June 24, 1970.

Two hypothetical accidents were examined. The work required the employment of the ANL two-dimensional hydrodynamics code REXCO to examine the details of energy transfer to the cover from a uniform coolant slug for two different initial conditions.

The FFTF input for each case is as follows:

	<u>Case A</u>	<u>Case B</u>
Uniform coolant velocity, cm/sec	4492	2706
Coolant mass of slug, slugs	6520	8620
Coolant kinetic energy, MW-sec	93	44
Original cover gas gap, ft	6	1.5

Pertinent physical dimensions are:

Vessel thickness: 2 in.

Plug weight: 700,000 lb

Total area of holddown bolts: 500 in.².

The results obtained involve three items for each case. The first item pertains to the computer Film Grid Display. It displays the progressive deformation of the grids, including the deformation of the reactor vessel in the critical area in the vicinity of the plug. Figure IV.C.1 shows deformation of grids and vessel at 3.16 msec after slug impact for Case A.

The second item is the printed output of the computer program. It provides considerable insight, both direct and peripheral, on the progress of the excursion. The important quantities obtained from this item are: (a) partition of kinetic energy into its radial and axial components; (b) velocities, displacements, and strains of the vessel; (c) velocity and displacement of the plug; and (d) strains of the holddown bolts.

The third item consists of graphs. This is the computer Cal-comp display of important parameters. A variety of graphs representing excursion effects were obtained; Fig. IV.C.2a shows total force for the plug, Fig. IV.C.2b depicts horizontal expansion of the vessel top, and Fig. IV.C.2c indicates axial displacement (lifting) of the plug.

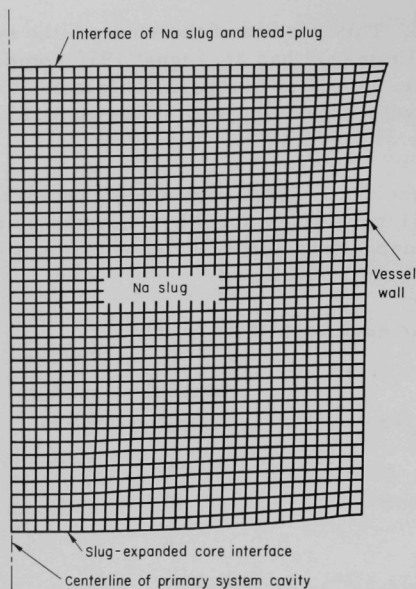


Fig. IV.C.1

Deformation of Vessel and of the Grids of Coolant Slug, 3.16 msec after Slug Impacts the Head-plug (Case A)

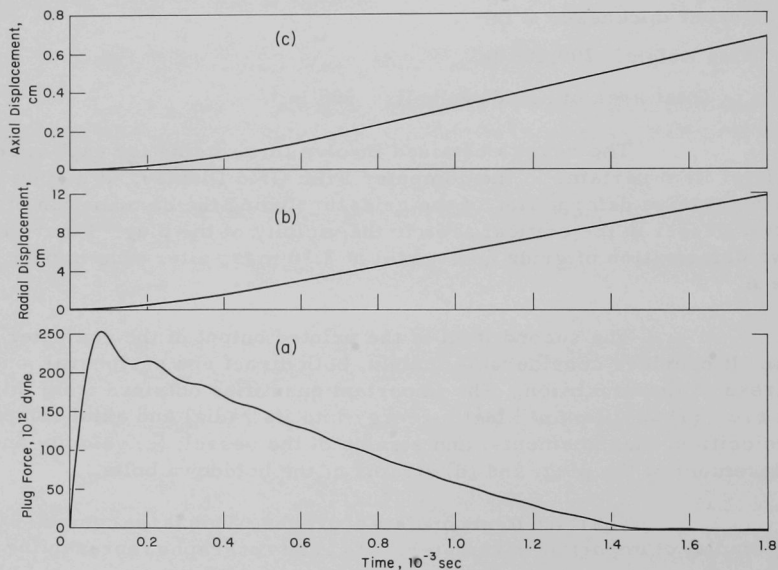


Fig. IV.C.2. Graphs Representing Excursion Effects: a. Impact of Coolant Slug on Head-plug (Case A); b. Radial Displacement of Reactor Vessel at Point Adjacent to the Reactor Plug (Case A); c. Axial Displacement (Uplift) of Reactor Plug (Case A)

The graphs extend these effects up to 3 msec. But, since a partition of energy is available in the output, the ultimate movement of the plug can be assessed. Although this preliminary study was of an investigative and not a design nature, it appears that with proper structural design of the primary system components, both accidents (Cases A and B) treated are quite "manageable."

Extending the capability of the REXCO-H program to analyze sodium in postburst accidents necessitates the inclusion of a molten-fuel-sodium interaction model. The mathematical formulation of the problem is fairly straightforward and is based on a quasi-steady-state heat-transfer model (see ANL-7688, pp. 240-244, April-May 1970) in which the heat-transfer coefficient, h , and the heat-transfer area, A , are treated as a lumped parameter. The set of equations to be solved is

$$\frac{\rho_0}{\rho} = \frac{d\psi}{d\bar{V}} \quad (\text{continuity}), \quad (1)$$

$$\ddot{r} = -\frac{1}{\rho} \frac{\partial p}{\partial r} \quad (\text{momentum}), \quad (2)$$

$$\ddot{z} = -\frac{1}{\rho} \frac{\partial p}{\partial z}, \quad (3)$$

$$dE = -pdV + \dot{Q}dt \quad (\text{energy}),$$

$$p = f(V, E) \quad (\text{state}), \quad (4)$$

and

$$\dot{Q} = [hA](T_f - T) \quad (\text{heat transfer}), \quad (5)$$

where

- ρ_0 = initial density,
- ρ = density,
- ψ, \bar{V} = volume,
- V = specific volume,
- \ddot{r} = radial acceleration,
- r = radius,
- p = pressure,
- \ddot{z} = axial acceleration,
- E = internal energy,
- \dot{Q} = heat flux,
- t = time,

T = average sodium temperature,
 T_f = average fuel temperature,
 A = area,

and

h = heat-transfer coefficient.

Numerical solutions of Eqs. 1 and 2 and a special case of Eq. 3 are already in existence in REXCO-H (see ANL-7498, November 1969). Inclusion of the heat-transfer equation and modification of the energy equation as well as extension of the equation of state to include the thermal expansion of liquid sodium will provide the capability to analyze sodium in accidents. Program modifications to include this model have begun.

PUBLICATIONS

Sodium Boiling and Fuel-Coolant Interactions

H. K. Fauske, R. O. Ivins, and J. F. Marchaterre

Proc. European Liquid Metal Boiling Working Group, Second Meeting, Casaccia di Roma, Italy, April 9-10, 1970, EURATOM, Brussels, 1970

Simulation of Liquid Metal Boiling and Two-Phase Flow with Nonmetallic Fluids

M. A. Grolmes and H. K. Fauske

Proc. European Liquid Metal Boiling Working Group, Second Meeting, Casaccia di Roma, Italy, April 9-10, 1970, EURATOM, Brussels, 1970

Laboratory Simulations of Cladding-Steam Reactions Following Loss-of-Coolant Accidents in Water-Cooled Power Reactors

J. C. Hesson, R. O. Ivins, R. E. Wilson, Kazuo Nishio, and Charles Barnes
ANL-7609 (Jan 1970)

Condensation of a High Velocity Vapor on a Subcooled Liquid Jet in Stratified Flow

J. H. Linehan and M. A. Grolmes

Proc. 4th Int. Heat Transfer Conf., Paris-Versailles, August 31-September 4, 1970. ASME, New York, 1970, Vol. VI, p. CS-2.6

Hybrid Computer Solution of Thermal Energy Equations in Porous Fuels

W. W. Marr and M. M. El-Wakil*

Nucl. Sci. Eng. 41, 271-280 (1970)

A Study of the Incipient Nucleation of Liquid Sodium

R. M. Singer and R. E. Holtz

Proc. 4th Int. Heat Transfer Conf., Paris-Versailles, August 31-September 4, 1970. ASME, New York, 1970, Vol. VI, p. B-8.6

PUBLICATION--General

Chemical Engineering Division Research Highlights, January-December 1969
ANL-7650

*The University of Wisconsin.

